OBSERVATIONAL TESTS OF THE THEORETICAL WHITE DWARF MASS-RADIUS RELATION

by

Simon Richard Guy Joyce

Thesis

Submitted to the University of Leicester

for the degree of

Doctor of Philosophy

Department of Physics and Astronomy

May 2018

UNIVERSITY OF LEICESTER

Contents

List of Tables

List of Figures

Acknowledgments

Thank you to my supervisors Martin Barstow and Sarah Casewell for giving me the opportunity to study the stars. From them I have learned not only about astronomy, but also the qualities required to be a good astronomer. I am grateful to them for sharing their wisdom and encouragement. Thank you to my parents Mike and Elaine for their love and support. The PhD took me 3.5 years, but for them it was more like 31.5. Thank you to my wonderful wife Summer, my guiding star, who has shared it all with me every step of the way. Without you it would have no meaning.

I would especially like to thank Jay Holberg for his kindness and sharing his enthusiasm for white dwarf research during our trips to Kitt Peak. His advice on all matters relating to Sirius B is greatly appreciated. Thank you to Howard Bond, who deserves a special mention as he was of immense help when writing the phase 2 proposal which made the HST observations a success. Thank you also to Simon "tlusty guru" Preval who taught me in a day what would have taken me years to work out on my own. The life and soul of the Physics department is the people who work there, and I have been fortunate to meet many good friends along the way. A full list of people who have made life here fun would be very long, but I would especially like to mention the members of the white dwarf group, Martin Barstow, Sarah Casewell, Matt Burleigh, Matt Bainbridge, Nicole Reindl, Ian Braker, Simon Preval, Emma Longstaff, Claudia "Tea buddy" Belardi and Nicolle Finch for all their support and companionship.

Finally I would like to thank Mr B. Ernie, the wise and generous philanthropist, whose generous contribution of £0.20 per week enabled this endevour to continue. I only hope that one day I can afford to repay him.

Figure 1: Image of Sirius taken on 22/02/2018, kindly provided by Mr Wouter van Reeven.

> *"It follows also from this, that we are yet very far off from the correctness we imagined ourselves to have arrived at in the fundamental determinations of astronomy; and, that a new problem presents itself, whose solution will cost much labour and a long period of time."*

- Friedrich Bessel 1844, *The variations of the proper motions of Procyon and Sirius*

Declarations

I, Simon Richard Guy Joyce, hereby declare that this thesis has not previously been submitted to any university for the award of a higher degree. This thesis is my own work except where references to other works are given.

Abstract

The mass-radius relation is one of the keys to understanding the structure of white dwarf stars. It has a sound theoretical basis, but improved observational tests are required to confirm if it describes real white dwarfs accurately. This thesis presents tests of the mass-radius relation using two different techniques to measure the mass. The approaches used are the spectroscopic method of fitting models to the hydrogen lines in white dwarf spectra, and the gravitational redshift method first proposed by Einstein in 1916. The first spectroscopic test is a detailed study of white dwarfs in binaries, and makes use of the recently available parallaxes from *Gaia* DR2. The new data remove the primary source of uncertainty affecting similar previous studies and finds that most white dwarfs agree with the MRR within 2σ. New results are obtained for several white dwarfs which have never previously been studied in detail. This study shows that the uncertainty remaining in the spectroscopic parameters is too large to test the detailed predictions of the MRR. The subsequent chapters detail results obtained using the gravitational redshift which provide further support for the MRR with greater precision than the spectroscopic results. A troubling discrepancy is found when comparing the mass of Sirius B measured using three different methods. The final chapter is a study of Sirius B using the gravitational redshift in a way specifically designed to remove the systematic uncertainties affecting previous studies. The new data confirm the validity of the gravitational redshift as a means of measuring white dwarf masses. Sirius B is found to be in agreement with both the MRR and the dynamical mass within 1σ. General Relativity pases the 3rd classical test with flying colours.

Chapter 1

Introduction

1.1 Overview

The brightest star in the sky is known as Sirius. It was known to the ancient Egyptians as Sopdet and its appearance each year signalled that the Nile was about to undergo its annual flood. Five thousand years later, the position of Sirius was measured by Friedrich Bessel. He noticed its sinusoidal motion on the sky and inferred the presence of an unseen companion (Bessel, 1844). This unseen star turned out to be the first white dwarf discovered, now known as Sirius B (Fig. 1.1).

This thesis is a study of white dwarf stars, and will continue the study of Sirius B, as well as many other white dwarfs which have now been discovered. In the years since the first observations of white dwarfs, we have gained a detailed understanding of these curious objects. Developments in theoretical physics such as quantum mechanics have allowed us to understand their structure and composition. Meanwhile, spectroscopy has given us the observational tools needed to acquire detailed data, which can be used to develop improved models and guide further theoretical development.

The development of the theory of stellar structure led to the discovery of a relationship between the mass and radius of white dwarfs. This relationship is one of the foundations of our understanding of this type of star and is used as a tool in many observational studies. These studies are the basis for much of what is known about white dwarfs, and have also made it possible to use white dwarfs as tools to investigate many other areas of astronomy. Despite this success, observational proof of the mass-radius relation has remained elusive. Several methods can be applied to independently measure the mass and radius so that they can be compared to the predictions of the theoretical relation. Each approach requires high precision data, the lack of which has until recently prevented conclusive tests.

In this thesis I will carry out observational tests designed to test the validity of the mass-radius relationship. Sirius B is a key part of this study because it is one of the few white dwarfs which can be studied using several different methods, so they can be directly compared. I will compare results obtained using each method and also assess the strengths, limitations and improvements that need to be made in order to definitively test this fundamental theory.

1.2 White Dwarfs

White dwarfs (WDs) are the remains of stars which have ended the nuclear burning main-sequence phase of stellar evolution. Single stars below a mass of 11 $M_{\odot}$, unless affected by a close companion, go through a red-giant phase as the hydrogen in their core runs out (Siess, 2007). Without the supporting pressure of nuclear burning, the contraction of the core releases gravitational potential energy. The release of energy causes heating of an outer shell of un-burnt hydrogen surrounding the core. This shell burning phase provides enough energy to greatly expand the outer envelope which is cast off into space. The remaining core is extremely hot ($\sim$ 1 million K) and dense. It is composed mostly of the heavy elements left over from nuclear fusion. The exact composition is dependent on the initial mass of the star which sets the limit on the heaviest element which can undergo fusion during the red-giant phase. A star will fuse elements in order of increasing atomic weight. Intermediate mass stars produce WDs composed of carbon/oxygen cores. More massive stars from 6.5 up to 11 $M_{\odot}$ form neon and magnesium core WDs (Weidemann, 2000; Panei et al., 2000). Some studies have found possible examples of WDs which appear to have an iron core (e.g. Provencal et al. 1998; Bédard et al. 2017). There is currently no known evolutionary scenario to form an iron core WD so these results present a problem if they are confirmed.

Another class of WDs have a He core and a total mass below 0.5 $M_{\odot}$. They would form from a main-sequence star of less than 0.8 $M_{\odot}$. However, the lifetime of such low mass stars is longer than the current age of the universe. Examples of low mass WDs have been found (e.g. Parsons et al. 2017) and are most likely the result of interaction with a binary companion which has caused accelerated mass loss during the red-giant branch phase or mass exchange.

The strong gravitational field of the remaining core causes the heaviest elements to settle to the centre with layers of successively lighter elements on top of one another (Schatzman, 1948). The outermost layer is the lightest remaining

Table 1.1: The main WD types and the approximate percentage of the 25pc population belonging to each type. Hybrid types are not included. Adapted from table 2 in Sion et al. (2014).

Classification	Spectral features	% of 25 pc sample	$T_{\rm eff}$ range (K)
DA	Only H Balmer lines	~ 59	4590-25193
DB	He I, No H	~ 0.8	16700
DC	Continuum only	~ 12	2600-7300
DO	He II lines strong	-	>45,000 K
DQ	Carbon lines present	~ 9	5590-10900
DZ	Metal lines only, No H / He	~ 6	4000-7500

element. For the majority of WDs this will be a thin layer of hydrogen. Despite being the thinnest layer, and making up only a tiny fraction of the mass of the white dwarf, the outer envelope is the only part of the white dwarf that can be directly observed. Therefore, the spectra of white dwarfs only contain the signature of the elements present in the outer atmosphere. White dwarfs are classified according to the elements which appear in their spectra as listed in Table 1.1.

The sample in Table 1.1 is a volume limited sample (Sion et al., 2014) within 25 pc so the percentages of different white dwarf types do not all match up with the percentages found in the magnitude limited white dwarf sample. The magnitude limited sample of white dwarfs (Koester & Kepler, 2015) includes a higher percentage of DBs (20 %).

The most common type of white dwarf (DA) make up about 60 per cent of the population. Their spectra show they have a hydrogen dominated atmosphere because of the strong absorption lines corresponding to transitions in the hydrogen atom. These are the Balmer lines in optical spectra and Lyman lines in the UV region. These are the main type of white dwarf which will be discussed in this thesis.

The spectral type of a WD is not necessarily fixed. At a certain point in its cooling evolution, a WD can transform from a DA to a DB (Sion et al., 2014). About 20 per cent (Koester & Kepler, 2015) of WDs have an outer layer composed mainly of helium, classified as DB or DO. As the star cools, the convective zone extends further, and can eventually dredge up He from the deeper layers. This occurs at a temperature of around 8000 to 15,000 K (Tremblay & Bergeron, 2008) depending on the thickness of the H layer. In other cases, DO white dwarfs, which form with a He envelope, can change in to a DA as they cool below 45,000 K due to the upward diffusion of hydrogen (see review by Barstow & Werner 2006).

Some WDs show evidence of trace amounts of heavy metals in their spectra.

These elements should sink on time-scales of a few days and were completely unepected until they were discovered by space based UV observatories. There are two possible explanations for their presence in the atmosphere. The gravitational settling process can be counteracted by radiative levitation, which lifts small amounts of heavy elements back to the surface. Far-UV observations (Barstow et al., 2014) showed that the percentage of DA white dwarfs with detectable heavy elements increases from around 20 per cent at 20,000 k to 65 per cent at 70,000 K. This fits with the theory or radiative levitation which is ineffective below 20,000 K but increasingly efficient at higher temperatures (Vauclair et al., 1979; Chayer et al., 1995). However, within a given temperature range, different stars have widely varying abundances. In addition to radiative levitation, accretion from rocky and dusty material is continually supplying heavy elements to some white dwarfs, which would account for the variation seen in abundance patterns. Evidence for ongoing accretion of rocky material has been inferred from the abundances of heavy elements measured from the spectra of some white dwarfs (e.g. Wilson et al. 2015; Harrison et al. 2018).

Apart from their spectra, the other main observational characteristic of white dwarfs is that they are very faint. The first white dwarfs to be discovered were Sirius B and Procyon B (Bessel, 1844). These are both in binaries, and careful observations of the orbits showed that they must have a mass comparable to that of the Sun. Their spectra showed that they have a very high temperature, around 25,000 K in the case of Sirius B. The relation between luminosity and temperature in equation (1.1) means that they should have a higher luminosity than was observed given their high temperature. The only way to explain the low luminosity was if the radius was very small, roughly the same radius as the Earth. However, with such a large mass, this would result in a density of 2.4×10^{6} (g cm^{-3}) which is much denser than the core of a normal star.

$$L = 4\pi R^2 \sigma T_{\rm eff}^4 \tag{1.1}$$

The lack of pressure from nuclear reactions allows the white dwarf to collapse under the influence of gravity. The development of quantum mechanics showed that at these densities, the material in a white dwarf must be degenerate, which means that all the lowest energy states are occupied and the electrons can not be forced any closer together.

In the case of particles such as electrons, which are classed as Fermions, the exclusion principal only allows 2 particles with opposite spin to occupy the same quantum volume. The quantum volume differs from a spherical volume in space defined by the size of the particle because it must also take into account the

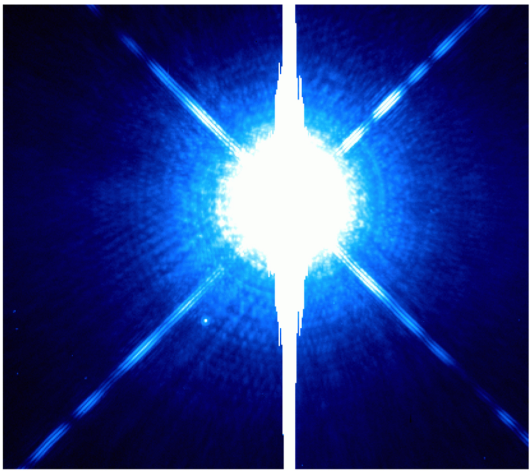

Figure 1.1: Image of Sirius taken with *HST*. Sirius B is the small dot on the lower left.

uncertainty in the position of the particle. A quantum volume is 6 dimensional, defined by the extent in the 3 spatial directions (dV) and also the 3 dimensions of the particles momentum ($4\pi p^2 dp$). The size of the quantum volume can not be smaller than Plancks constant along each of the 3 dimensions, equation 1.2.

$$4\pi p^2 dp dV > h^3 \tag{1.2}$$

Degeneracy pressure is a consequence of the minimum quantum volume, resulting from the uncertainty principal, and the exclusion principal which only allows two fermions to occupy the same volume simultaneously. It is this degeneracy pressure which supports the star against further collapse under the influence of gravity in the absence of outward pressure from nuclear fusion (Fowler, 1926).

A white dwarf then, consists of a dense core of degenerate material shrouded in a thin atmosphere of non-degenerate hydrogen or helium. The stored heat in its core keeps it shining long after nuclear reactions have ended, but over time the star will cool as its energy is radiated away. The fate of the isolated white dwarf is to slowly cool over billions of years until it fades from view and becomes a black dwarf.

1.2.1 Temperature and cooling

The temperature of a white dwarf is relevant to the mass-radius relation because theoretical models show that the radius of a white dwarf is dependent on temperature, especially at the low-mass end. Therefore, it is vital to have accurate measurements of a white dwarf's temperature to be able to compare it to the appropriate mass-radius relation.

White dwarfs cool down over time as their internal reservoir of energy is radiated away into space. There is no hydrogen or helium left in the core to fuel nuclear reactions which would maintain the temperature of the core. Also, the core material is already in the most compact degenerate state so it can not release gravitational potential energy by contracting further.

The key factors that determine how long it takes a white dwarf to cool down are the amount of stored energy in the core, and the rate of energy loss through the envelope. In the core the electrons can move freely from atom to atom and efficiently transport heat. This means that the core is nearly isothermal throughout. The total amount of energy available depends on the mass of the core, which is 99 per cent of the white dwarf's total mass. The energy is stored as kinetic energy of the ions, so the atomic weight of the ions which make up the core is also a factor in how much energy is available. Lighter elements (e.g. Carbon) have more ions per unit mass, and so they can store more energy. If the core contains a greater proportion of heavier elements, such as oxygen, there are less ions available to store energy.

The hydrogen / helium envelope is relatively thin, but is made up of non-degenerate gas which is a very good thermal insulator and quite opaque to radiation. The thickness of the envelope strongly regulates the rate of heat loss. The maximum mass of the envelope as a fraction of the total white dwarf mass is 10^{-4} (Fontaine, Brassard & Bergeron, 2001), whereas a thin envelope is only $\sim 10^{-10}$. Through spectroscopy it is possible to determine if the envelope is hydrogen or helium dominated. The mass-radius relation is also affected by the thickness and composition of the envelope.

The basic factors involved in determining the cooling time are summarised in equation (1.3) (Mestel, 1952).

$$t_{cool} \propto A^{-1}\mu^{-2/7}M^{5/7}L^{-5/7} \tag{1.3}$$

Where A is the atomic weight of the core material, μ is the molecular weight of the envelope material, M and L are the mass and luminosity of the white dwarf.

Typical time scales for a white dwarf to cool from 150,000 K to 10,000 K are 1 or 2 billion years. The initial rate of cooling is relatively fast because of the high luminosity. As the temperature decreases, the luminosity also decreases, slowing the rate of energy loss from the star.

Fig. 1.2 shows theoretical cooling tracks for C/O (50/50 by mass fraction) core white dwarfs for a range of different masses and H-layer thickness (Fontaine, Brassard & Bergeron, 2001). A high mass white dwarf will initially cool at a slower

Figure 1.2: Cooling tracks for white dwarfs of different mass and H-layer thickness. (Fontaine, Brassard & Bergeron, 2001)

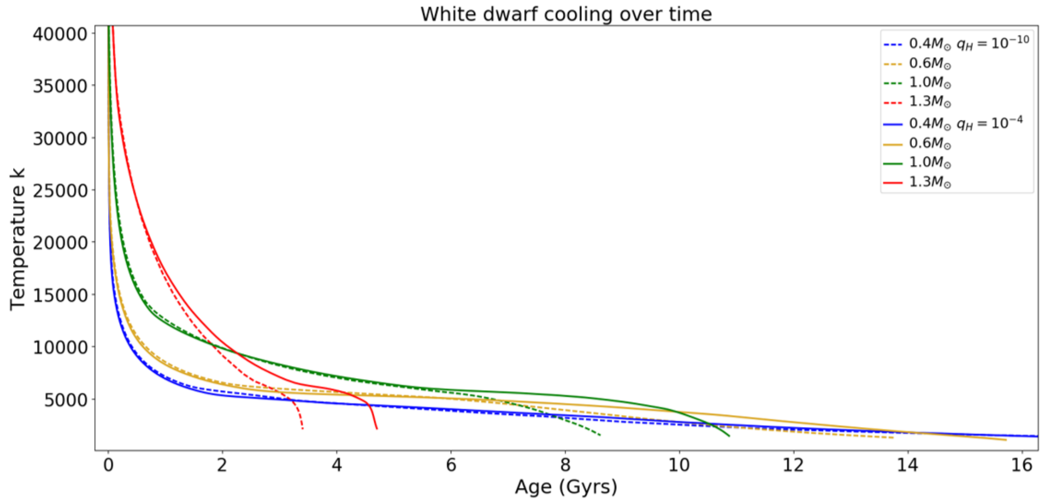

rate than a low mass white dwarf, as seen on the left of Fig. 1.2.

At a temperature known as the Debye temperature, the white dwarf starts to crystalize. The exact temperature at which this occurs depends on the density. The crystalization process first slows down the rate of cooling as the latent heat of crystalization is released, providing an additional source of energy. Once the core is crystallised however, it has a lower heat capacity than when it was in a liquid state, and so the cooling accelerates. This can be seen in the red curve for a 1.3 $M_\odot$ white dwarf just before 4 Gyrs. The curve flattens as the latent heat is released, but then the cooling rapidly accelerates just after 4 Gyrs.

The solid lines in Fig. 1.2 show that the cooling rate is reduced if there is a thick ($q_H = 10^{-4}$) H-layer, compared to the cooling rate for the thin envelope (dashed lines).

It is therefore important to know not only the temperature, but also the composition of the core and the envelope as well as the mass and radius of a white dwarf in order to place it on the proper cooling track and accurately derive its age.

1.2.2 Luminosity

The low luminosity of white dwarfs makes it difficult to detect them out to large distances. Apparent visual magnitudes in the 25 pc sample range from 8 to 18 although the majority are between 14 - 16.5 . The known population of white dwarfs is only estimated to be 86 per cent complete out to 20 pc (Holberg et al., 2016).

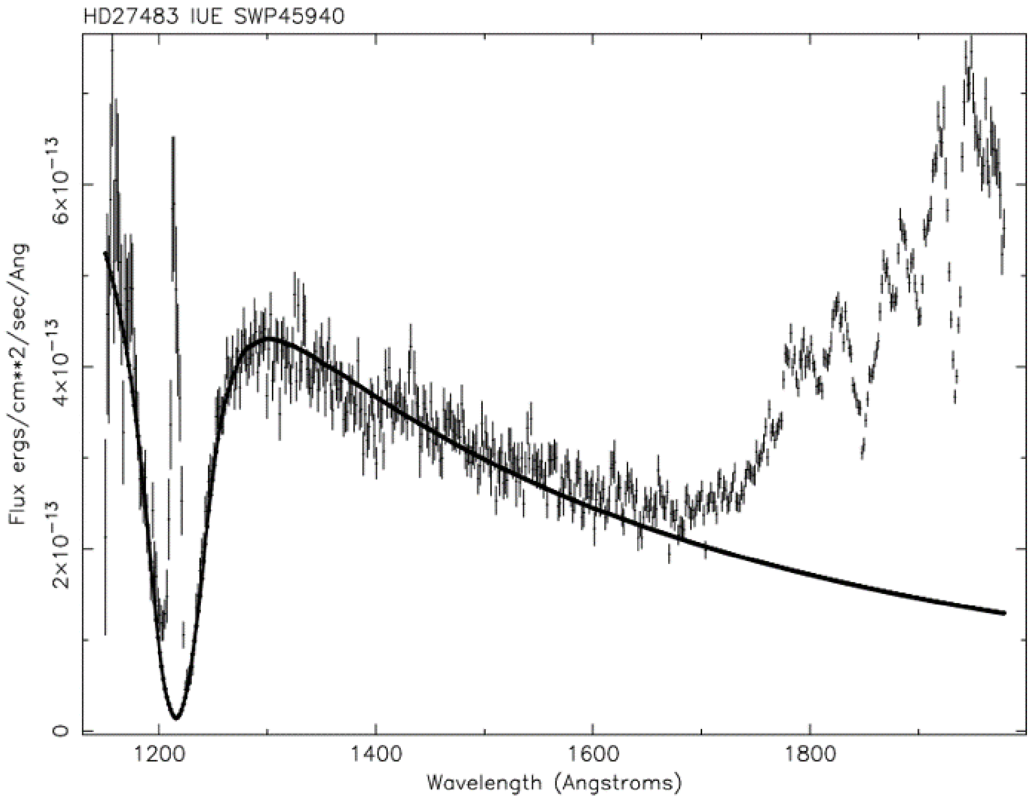

Figure 1.3: Example of a UV spectrum for HR1358 showing the WD spectrum emerging at short wavelengths. (Burleigh et al., 1998)

The degenerate nature of the white dwarf creates the unusual characteristic that the more massive they are, the smaller their radius. Observationally, this means that for two white dwarfs of the same temperature, the more massive one will have a lower luminosity.

The high temperatures ($> 10,000$ K) of many white dwarfs cause their spectral energy distribution to peak in the ultra-violet. DA white dwarfs display the Lyman series of hydrogen absorption lines in the wavelength range 1200 to 900 Å. Many white dwarfs in unresolved close binary systems with a main sequence star have been discovered because of the excess UV emission visible in the combined spectrum (e.g. Burleigh et al. 1998). Fig. 1.3 is an example of a system (HR1358) consisting of two F6V type stars which were found to have a hidden white dwarf companion visible in the UV spectrum.

1.2.3 Sirius-Like Systems

The term Sirius-Like systems (SLSs) refers to binaries with a white dwarf and a main sequence star of type K or earlier. These systems are distinct from the WD+M-dwarf systems because the white dwarf is less luminous than the main sequence star at optical wavelengths. Only ∼90 SLSs have been identified due to the difficulty in detecting the faint white dwarf next to a luminous star. Within 20 pc of Earth, around 8 per cent of white dwarfs are in SLSs. Beyond this distance, the number of identified SLSs drops to only a few percent, indicating that many of these systems remain to be discovered (Holberg et al., 2013). Several of the systems studied in this thesis were identified as candidate SLSs due to a UV excess in their spectrum. The white dwarfs were resolved for the first time using *HST* (Barstow et al., 2001) and the optical spectra presented in this thesis are the first ever obtained.

1.3 Methods for measuring the mass and radius

1.3.1 Measuring the radius

The radius of a white dwarf can be measured by its relation to the detected flux following the method of Holberg & Bergeron (2006). The flux emitted per unit surface area of the white dwarf is

$$F_{\text{surface}} = 4\pi H_{\lambda}(T_{\text{eff}}, log\ g) \tag{1.4}$$

where H_{λ} is the monochromatic Eddington flux. The surface flux depends on the temperature and gravity of the white dwarf. The relation between the flux at the stellar surface and that detected at Earth depends on the distance and radius of the star (equation 1.5).

$$f_{\text{Earth}} = \frac{R^2}{D^2} F_{\text{surface}} \tag{1.5}$$

If the distance is known from another method such as the parallax, then the measured flux (f_{Earth}) gives the radius of the star via

$$R = D\sqrt{\frac{f_{\text{Earth}}}{4\pi H_{\lambda}(T_{\text{eff}}, log\ g)}} \tag{1.6}$$

Another method is to use light-curves of eclipsing binaries. Excellent results have recently been achieved where the eclipses make it possible to measure very precise radii (e.g. Parsons et al. 2010; Bours et al. 2016). A recent study (Parsons et al., 2017) combined these radii with XSHOOTER spectroscopy to measure the MRR for 26 WDs to a precision of 2.4 per cent (radius) and 2.7 per cent(mass). This method is highly accurate, but can only be applied to a limited number of stars as it requires the inclination of the binary to be almost edge on to the observer.

1.3.2 The dynamical method

In the dynamical method, the mass of a star is derived from the orbital motion of the binary. It requires observations of the positions of the stars over a sufficiently long period of time to observe a large part of the orbit. In the case of Sirius-like systems this usually requires observations spanning decades as their orbital periods can be hundreds of years long. Once the orbit has been observed, it is fitted with a model which includes the orbital period (P) and semi-major axis (a) as parameters. These are related to the mass of the binary components via Kepler's 3rd law (1.7), where the total mass of the binary is $M_{\text{total}} = m_1 + m_2$.

$$\frac{P^2}{a^3} = \frac{4\pi^2}{G(m_1 + m_2)} \tag{1.7}$$

The individual masses are then found by equation (1.8) and (1.9) where (a_{A}) is the semi-major axis for the absolute motion of Sirius A observed on the sky as opposed to the semi-major axis of the binary orbit found from the model (a), (Bond et al., 2017).

$$M_{\text{A}} = M_{\text{total}}(1 - a_{\text{A}}/a) \tag{1.8}$$

$$M_{\text{B}} = M_{\text{total}} \times a_{\text{A}}/a \tag{1.9}$$

The first application of this method to a white dwarf (Sirius B), though the white dwarf itself had not yet been observed, was by Bessel (1844) who was making measurements of the position of Sirius A.

Sirius B can now be observed with *HST* and the orbit is well determined. Fig. 1.4 shows the orbit of Sirius B relative to Sirius A as defined by many decades of observations. From this data, it is possible to fit a model orbit which includes the period (P) and semi-major axis (a) as parameters. Several white dwarfs in binaries (e.g. Procyon, 40 Eri B) now have accurate orbit and mass determinations following long term observing campaigns and the analysis of historical observations going back over 100 years (Bond et al., 2015, 2017).

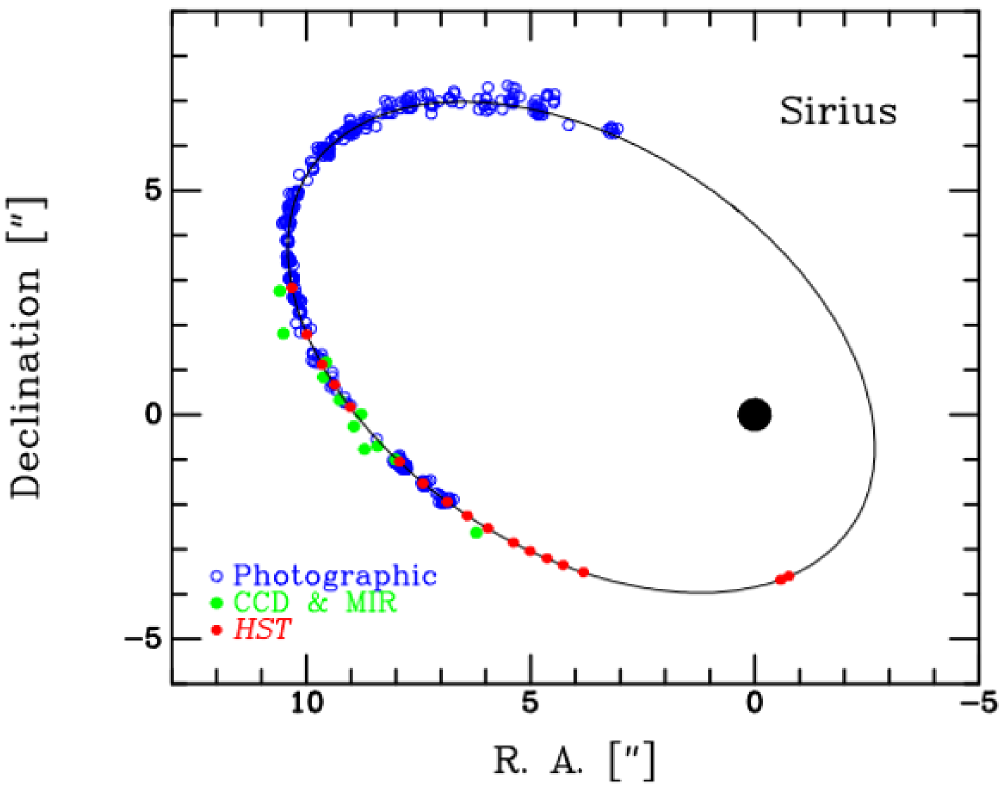

Figure 1.4: Example of the measurement of the orbit of Sirius from over 150 years of observations. (Bond et al., 2017)

1.3.3 The spectroscopic method

Theory

The spectroscopic method uses the shape of the broad hydrogen absorption lines as a diagnostic of the conditions in the white dwarf atmosphere. The broadening and depth of the lines are sensitive to the temperature and pressure. The high pressure is a result of the gravity of the white dwarf so the line broadening provides a way to measure the gravitational field strength (g) and is a function of the mass-radius ratio (equation 1.10). If an independent measure of the radius can be obtained then the log g value is all that is required to calculate the mass.

$$g = \frac{GM}{R^2} \tag{1.10}$$

The shape of the absorption lines is the result of a combination of several processes. The width of the absorption lines in white dwarf atmospheres is mainly due to pressure broadening (also known as Stark broadening or collisional broadening).

According to the theory of Stark broadening (Vidal et al., 1970), the energy levels of the hydrogen atoms in the white dwarf atmosphere are slightly altered due to the electric field of the nearby charged particles. In a high pressure gas, there are also many close encounters between atoms which have a similar distorting effect on the energy levels. The distortions change the energy required for an electron to transition to a higher level. The energy of a photon depends on its frequency, so the distortion of the energy levels allows photons with slightly longer or shorter wavelengths can be absorbed. The superposition of many atoms with various levels of distortion causes a broad wing either side of the line core as shown in Fig. 1.5. In this figure, the lowest line is H-β and each subsequent line in the Balmer series is shifted upward for clarity. The dashed lines are models with log g 7.0 and the lines get thicker to represent models with increasing log g up to 9.0 in steps of 0.5 dex. For the H-β and H-γ lines, the Stark effect broadens the line. For lines H-δ and higher, the Stark effect reduces the probability of a transition to the higher energy levels so the depth of these lines is reduced with increasing pressure.

The depth of the lines is mostly affected by the temperature which determines the proportion of atoms in each excitation state (Hummer & Mihalas, 1988). At temperatures around 15,000 K, the majority of H atoms are not ionised so there are many atoms available to absorb photons. An atmosphere at this temperature therefore forms deep absorption lines. The lines get shallower for hotter white dwarfs as the population of H atoms is increasingly ionised. Fig. 1.5 shows the decreasing line depth from left to right with increasing temperature.

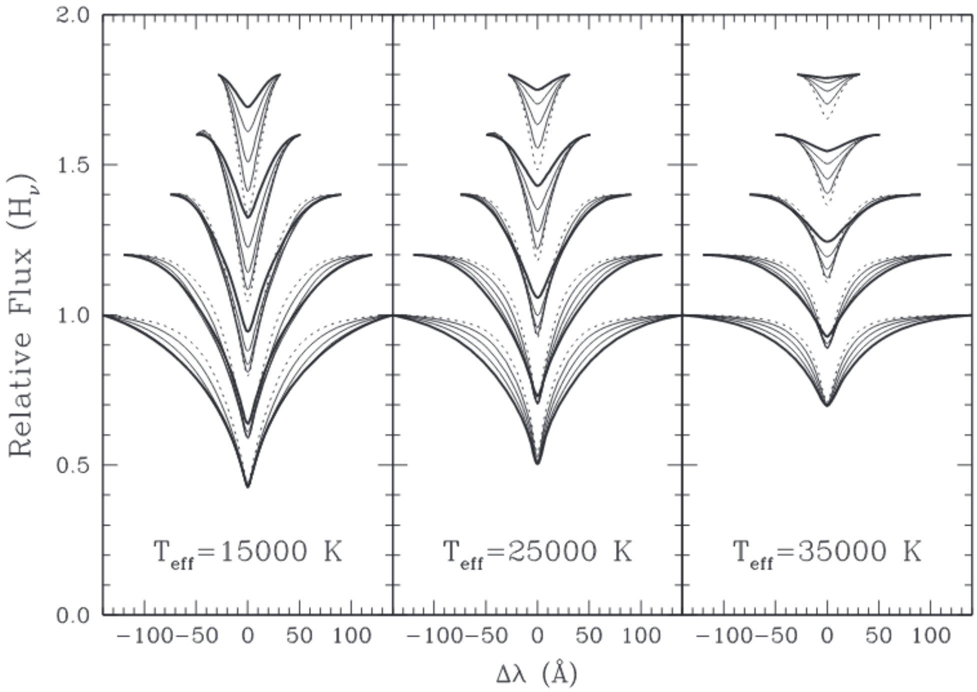

Figure 1.5: The effect of $T_{\rm eff}$ and log g on the shape of the Balmer absorption lines. The models illustrated have log g 7.0 (dashed lines) increasing to 9.0 in steps of 0.5. The temperature is indicated in each of the panels. Figure reproduced from (Tremblay & Bergeron, 2009).

The application of the spectroscopic method to white dwarfs was developed by (Holberg et al., 1985; Bergeron, Saffer & Liebert, 1992). It is a valuable tool for DA white dwarfs which have strong hydrogen absorption lines in the optical wavelengths (Balmer lines) and in the UV (Lyman lines).

The usual method followed is to generate a grid of model spectra with a range of temperature and log g and fit this to the data to find the best fitting values for these parameters. The radius can be found from photometry or from the normalization of the spectral model if the data are flux calibrated.

The principal advantage of the spectroscopic method over other methods of testing the mass-radius relation is that it can be applied to single white dwarfs easily, whereas the other methods usually require the white dwarf to be in a binary. Spectroscopic data requires only a single observation, and large catalogues of high quality spectra such as SDSS are now available. The main disadvantage is that the method relies on the accuracy of the models which in turn are affected by assumptions made in the theories of stellar structure and radiative transfer. Generating the synthetic spectra requires detailed information on the energy levels of the atoms involved. This becomes especially difficult for white dwarfs containing heavy metal pollution where the heavy ions can have thousands of possible transitions. The effect of these thousands of absorption lines is called line blanketing. It increases the opacity of the atmosphere at short wavelengths so more light is emitted in the red and infra-red region of the spectrum. However, it is the effect on the H lines that is important.

1.3.4 The gravitational redshift method

Theory

According to Einstein's theory of General Relativity (Einstein, 1916), a massive body, such as a white dwarf, causes a curvature of space-time so that the gravitational potential energy ϕ near to the white dwarf is lower than the gravitational potential energy far from the object. Conventionally, ϕ is taken to be zero at an infinite distance from the mass. A consequence of relativity is that time passes more slowly in a region of lower ϕ close to the object, than it does for an observer in a region of higher gravitational potential energy far away. As a result of the slowing down of time, light emitted at a particular wavelength close to the white dwarf, will have a lower frequency than it would if it had been emitted in a region with the same gravitational potential energy as the observer's position. As a consequence of its reduced frequency, the light will appear to be red-shifted (Einstein, 1911).

The following example demonstrates how the gravitational red-shift affects the spectrum of a white dwarf. The gravitational potential (ϕ) is the gravitational potential energy (U) per unit mass and is measured in $\mathrm{Nm\,kg^{-1}}$. The gravitational potential at the surface of the white dwarf is given by equation (1.11) where M and R are the mass and radius of the white dwarf and G is the universal gravitational constant. The large mass and small radius of white dwarfs results in a much lower ϕ at their surface in comparison to a normal main sequence star.

$$\phi = -\frac{GM}{R} \tag{1.11}$$

The hydrogen atoms in the atmosphere of a DA white dwarf absorb photons with specific frequencies related to the energy of the available electron orbital transitions. Electrons in the n=2 level of the hydrogen atom can jump up to the n=3 level by absorbing a photon with an energy of 1.9 eV. The energy of the emitted photon is related to its frequency and wavelength by equation (1.12). The energy required for this transition corresponds to photons with a frequency of 6562.8 Å, also known as the H-α line. The absorption line in the white dwarf spectrum would appear at this wavelength, except for the fact that the light must first escape from the gravitational potential of the white dwarf.

$$E = hf = \frac{hc}{\lambda} \tag{1.12}$$

The frequency of the photon is related to the time between successive wave peaks $t = \frac{1}{f}$, so a change in the rate of flow of time will alter the frequency. The change in the rate of time is a consequence of the difference in gravitational potential energy between the source and observer and is given by equation (1.13).

$$\frac{\Delta t_2 - \Delta t_1}{\Delta t} = \frac{1}{c^2}(\phi_2 - \phi_1) \tag{1.13}$$

If we assume the observer on Earth is at a great distance from the white dwarf then $\phi_2 = 0$. Using values of M = 1 $M_\odot$ and R = 0.008 $R_\odot$ appropriate for a white dwarf like Sirius B gives $\phi_1 = -2.38 \times 10^{13}\,\mathrm{Nm\,kg^{-1}}$. The time interval between wave peaks corresponding to the frequency of H-α (6562.81 Å) as measured on Earth is 2.18912×10^{-15} s. At the surface of the white dwarf, this time interval is increased to 2.18969×10^{-15} s. Converting this to a wavelength using $f_1 = \frac{1}{t_1}$ and $\lambda_{WD} = \frac{c}{f_1}$ gives a wavelength of 6564.55 Å which is 1.74 Å longer than the rest wavelength.

The wavelength shift caused by gravity is indistinguishable from the Doppler shift which would result if the WD were moving away from the observer. For this

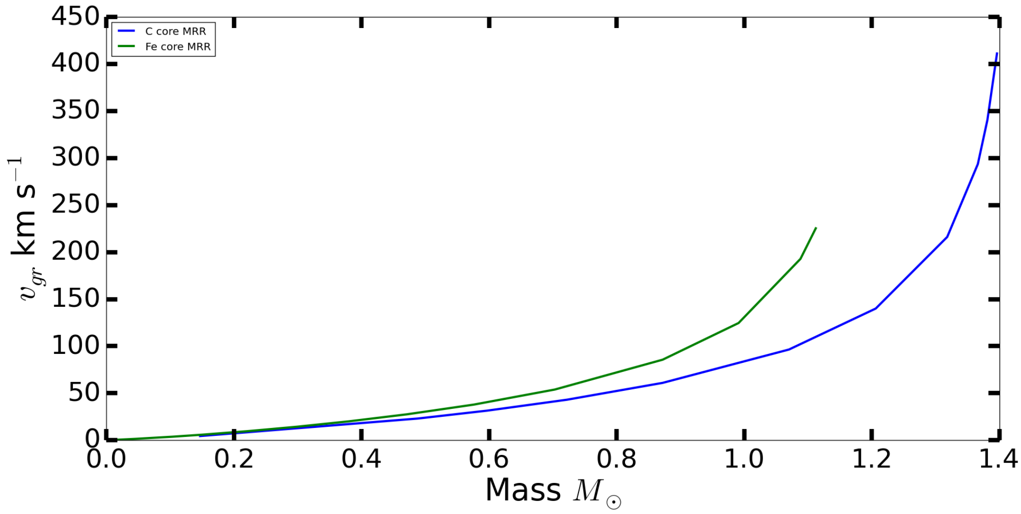

Figure 1.6: The apparent velocity due to the gravitational red-shift of the spectral lines for the full range of WD mass. The calculations are based on the predicted mass-radius ratio from the (Hamada & Salpeter, 1961) models with a carbon core composition (blue) and an iron composition (green).

reason, the gravitational red-shift can also be expressed in terms of velocity. The gravitational wavelength shift calculated for Sirius B corresponds to ~ 80 km s^{-1} (equation 1.14).

$$v_{gr} = \frac{\lambda_{WD} - \lambda_{rest}}{\lambda_{rest}} \times c = 80 \text{ (km s}^{-1}) \tag{1.14}$$

Fig. 1.6 shows the expected gravitational red-shift in units of velocity shift of the H-α line for the full range of white dwarf masses and radii assuming they follow the theoretical MRR. The purple line is for a carbon core MRR. For comparison, the blue line shows that the gravitational velocity is higher for a theoretical Fe core white dwarf of the same mass due to the smaller radius.

1.4 The Stark pressure shift

When using the wavelength shift of the hydrogen absorption lines to measure the gravitational redshift, it is important to take into account any other effects which could also cause a shift in the line. One such effect which requires careful consideration is the pressure shift. This is related to the Stark effect which produces the broadening of the hydrogen lines, but in this case it may also shift the wavelength of the line or cause it to be slightly asymmetrical. In the literature it is often referred to as either the "Stark shift" or the "Pressure shift". I will refer to it as the pressure shift (PS) here.

Lab based studies of hot plasma, designed to simulate a white dwarf atmosphere, have shown that the observed lines are slightly redshifted. Wiese & Kelleher (1971) showed that the size of the shift was up to 1 Å. This is quite considerable compared to the expected $\sim$ 1.7 Å shift caused by the gravity of a WD.

1.4.1 Pressure shift : Theoretical background

Lab based studies (Grabowski et al., 1987; Madej & Grabowski, 1990; Falcon et al., 2015; Halenka et al., 2015) have been used to provide the detailed line profiles which any theory of the pressure shift must be able to reproduce.

A theoretical explanation of the PS was developed by Grabowski & Halenka (1975) and later improved upon by Halenka et al. (2015). The plasma at the temperature and density of a WD atmosphere is made up of H atoms, some of which have been ionised. The free electrons and positive ions have electrostatic fields which act on the H atoms, causing slight deformations of the energy levels. These deformations alter the amount of energy required for a bound-bound transition. This results in photons of slightly different energy(wavelength) being absorbed. The ions move comparatively slowly and the ionic electric field is considered to be static. The electrons are much faster and distort the atomic energy levels due to frequent collisions. The cloud of electrons also have the effect of shielding individual atoms from the effect of the positive ionic electric field known as Debye screening.

Theoretical line profiles calculated with the 'Full Computer Simulation Method' Olchawa (2002) have been able to reproduce the pressure shift and asymmetry detected in lab based plasma and can be used to investigate the probable magnitude of the effect in the atmospheres of white dwarfs (Halenka et al., 2015).

The pressure shift is proportional to the density of free electrons in the plasma (N_e) divided by the temperature (Halenka et al., 2015).

$$PS \propto \frac{N_e}{T} \tag{1.15}$$

1.4.2 Asymetry vs shift

The pressure shift also causes an asymmetry of the line because it has a greater effect for wavelengths further from the line centre. The broad wings of the absorption line are thus shifted further than the core of the line.

The situation is illustrated in Fig. 1.7 (from figure 10, Halenka et al. 2015).

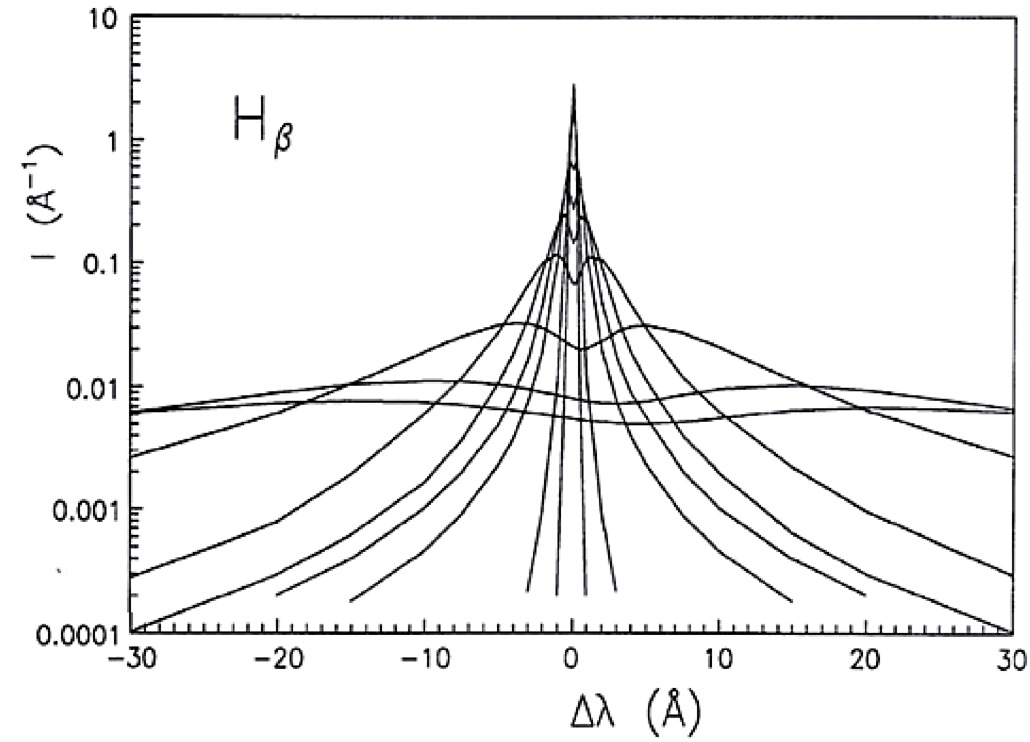

Figure 1.7: Line formation in a WD atmosphere. The line formed deeper in the atmosphere is the road flat line showing a large offset from the central wavelength. Lines formed at successively shallower depths become narrower and less pressure shifted. The line that finally emerges is a superposition of the lines formed at all depths. Figure reproduced from (Halenka et al., 2015).

The core of the absorption line is formed in the shallow outer layers of the atmosphere where the electron density is low. The pressure shift and broadening effect are weakest in this low N_e environment so the line is deep and symmetrical with minimal broadening. The wings of the line form deeper in the atmosphere where N_e is high, producing the maximum broadening of the wings. At this depth, the line is also strongly pressure shifted to longer wavelengths.

The observed line from a white dwarf atmosphere is the sum of contributions from a range of depths in the atmosphere. From the core to the wings, the line is formed at successively deeper depths in the atmosphere and subject to increasing pressure shift and broadening due to the increasing electron density. The superposition of the lines formed at all depths results in an observed line which is not shifted in the core but is increasingly pressure shifted in the wings, causing the wings to be asymmetrical.

1.4.3 Implications of pressure shift for observations of white dwarfs

Definition of the line centre

As a result of the convolution of the pressure shift and the asymmetry, along with the broadening of the absorption lines, it becomes necessary to clearly set out how the wavelength of the line will be defined.

The studies by (Greenstein & Trimble, 1967) used low resolution spectra ($\sim$ 190 Å/mm). The sharp line core was not resolved so it was necessary to include the broadened wings of the line. This method can include a range of up to 40 Å centred on the core of the line.

Lab based measurements (Wiese & Kelleher, 1971) used the average center point of horizontal lines placed at 1/2, 1/4 and $1/8_{th}$ of the maximum line depth. This method may not be reliable because the horizontal lines are measuring the wings at different points which are increasingly affected by asymmetry at distances further from the line centre. Also, the core and wings of the line are formed at different depths in the atmosphere where the differing plasma conditions alter the size of the contribution from the pressure shift.

The method adopted in Barstow et al. (2005) is to fit model spectra to the data to determine the shift of the line compared to the rest wavelength of the model. This is again susceptible to the increasing pressure shift contribution if the wavelength range fitted is too wide. For this reason, Barstow et al. (2005) repeated the fitting of each line several times, including a wider range centred on the line core each time. This method could be used to assess the relative contribution of the pressure shift and gravitational shift components.

Measurements of the gravitational redshift

Lab based tests which reproduce the plasma conditions in a white dwarf atmosphere have shown that the degree to which a line is affected by the pressure shift effect depends on the following factors.

Each line in the Balmer series is affected to a different degree. Higher order lines are shifted more than H-α. Therefore, H-α is the best line to use for measuring the gravitational redshift. Higher order lines would need to be corrected to remove the additional pressure shift.

The amount of shift also depends on the temperature and log g. Fig. 1.9, (from Grabowski et al. 1987, Figure 5) shows that the shift is greatest at temperatures below $\sim 15,000K$ and decreases by about 1 km s^{-1} as the temperature increases. Comparison of the log g = 9 (dashed) line with the log g =8 (solid lines)

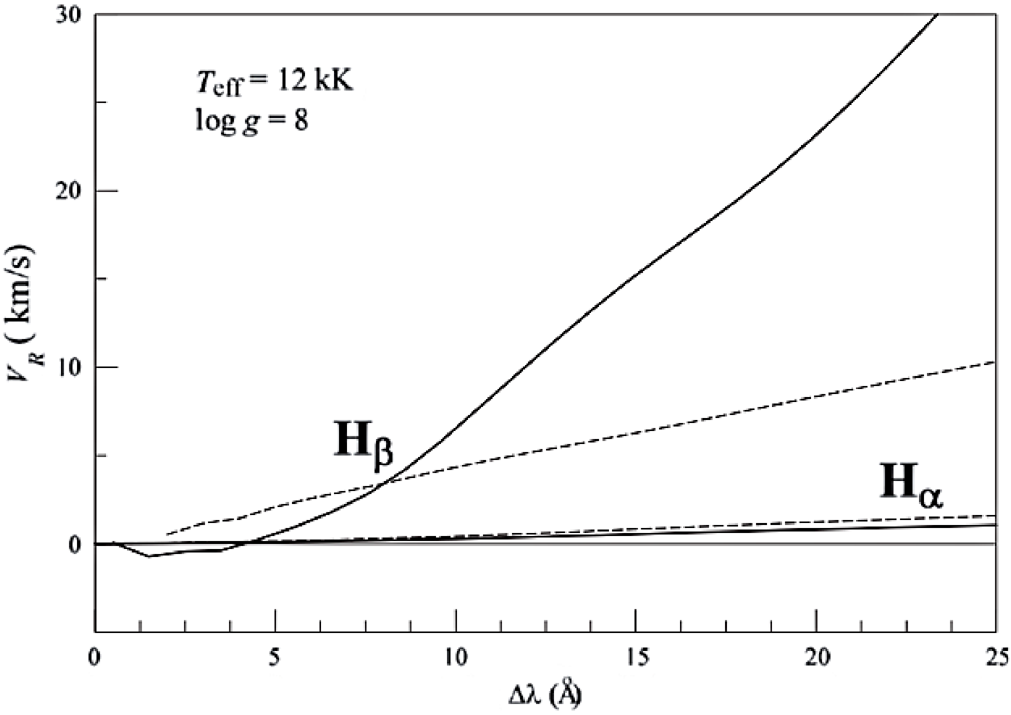

Figure 1.8: Velocity resulting from the pressure shift for H-α and H-β showing the increasing pressure shift as a wider range of wavelengths is included in the measurement of the line position. (Halenka et al., 2015)

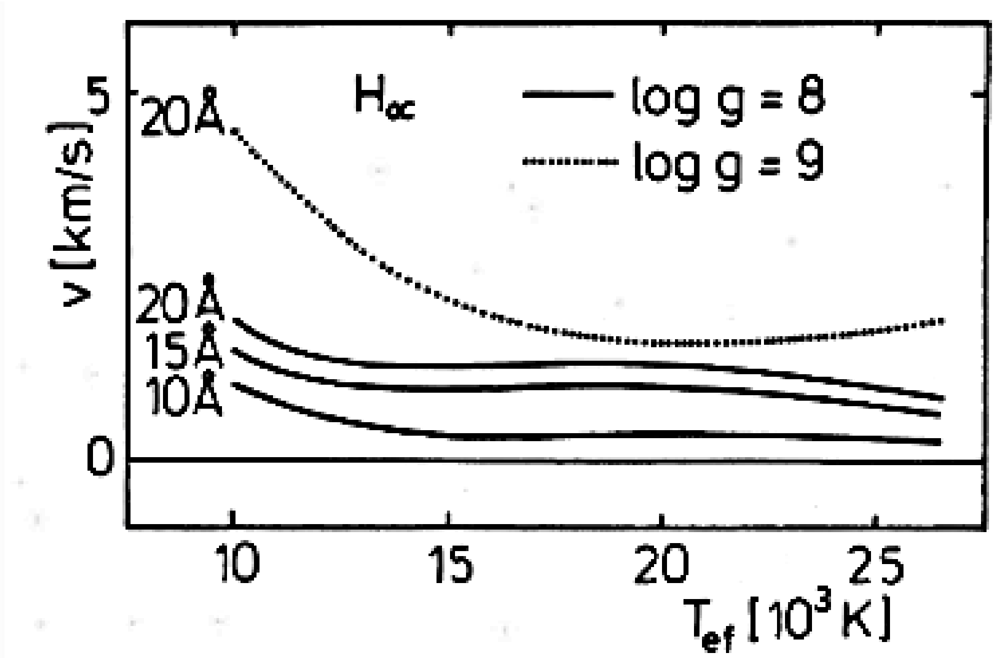

Figure 1.9: Pressure shift for H-α (Grabowski et al., 1987). The magnitude of the pressure shift varies with $T_{\rm eff}$ and log g. Numbers on the left indicate the wavelength range included when measuring the position of the broadened line.

shows that the effect increases with surface gravity. This is particularly relevant for high mass white dwarfs such as Sirius B which have a log g ~8.6. The numbers to the left of the figure indicate the wavelength range used to measure the line position. Including more of the wings increases the effect of the pressure shift on the measurement.

The general rule for all lines is that the pressure shift increases with increasing electron density. Lab based measurements have probed electron densities up to $n_e = 100 \times 10^{16}$ cm^{-3} (Falcon et al., 2017). This density range is applicable to most white dwarfs.

Fig. 1.9 indicates that for a white dwarf of the approximate temperature of Sirius B ($\sim 25,000$K) and log g 8.6, the pressure shift for the H-α line will always be less than 2-3 km s^{-1}. The majority of white dwarfs have log g between 7-8 and will be even less affected.

Lastly, the method used to measure the wavelength of the line is crucially important. All studies (e.g. Falcon et al. 2015; Halenka et al. 2015) have shown that the wings are increasingly pressure shifted with increasing distance from the line core. Over a range of 0-10 Å from the line centre, the pressure shift is minimal. For high resolution spectra such as those from *HST* with a resolution of 5000-10,000, the line is sufficiently resolved to measure its position using only the line core. For lower resolution (e.g. SDSS spectra) with a resolution of 2000 or less, the inclusion of the wings beyond 20 Å will add an increasingly significant pressure shift the more the wings are included in the measurement.

In summary, the pressure shift is unlikely to contribute significantly to the observed line shift when measured using the H-α line. Fig. 1.8 shows that the maximum pressure shift contribution to the observed velocity is estimated at < 2 km s^{-1}. However, for higher order lines (H-β onwards), the pressure shift is likely to contribute significantly, from 5-30 km s^{-1}.

1.5 The mass-radius relation

1.5.1 Theory

From the measurements of the mass and radius of Sirius B at the start of the 19th century, it was known that the material in a white dwarf must be in a state of extremely high pressure and density. The matter in the core of a white dwarf is pressure ionised so that the electrons are all separated from the atoms and can move freely. This sea of free electrons behaves like a gas.

Unlike an ideal gas where the presure is a result of the kinetic energy of the particles, the pressure of the electron gas is due to a combination of the Pauli exclusion principal and the Heisenberg uncertainty.

The Heisenberg uncertainty principal specifies the minimum volume of space which is occupied by each electron. The volume is larger than would be the case if electrons were solid particles. Instead, electrons behave like waves and are spread out. They are also in motion so they have momentum. It is not possible to define both the position and momentum of an electron any more precisely than the limit $\hbar/2$ where $\hbar$ is Planks constant / 2π .

$$\Delta x \Delta p > \frac{\hbar}{2} \tag{1.16}$$

The Pauli exclusion principal limits how many electrons can occupy the volume defined by the uncertainty principal. Only one electron can occupy the same energy state within a given volume of space.

When the density is high enough to pack the electrons into the smallest possible volume, this is the lowest energy configuration and is known as a degenerate electron gas. It is the electron degeneracy pressure that supports the star against gravitational collapse, and so the structure of the white dwarf depends almost entirely on the properties of this electron gas rather than the ions.

The investigation of stellar structure which first led to an understanding of collapsed configurations (WDs) was done by (Milne, 1930). This theory was developed further by (Chandrasekhar, 1931),"The Highly Collapsed Configurations of a Stellar Mass". The maximum mass of a white dwarf was derived in a separate paper (Chandrasekhar, 1931),"The maximum mass of ideal white dwarfs".

The early models of white dwarf structure were called zero-temperature models because they make the assumption that the pressure is provided entirely by the electrons and does not depend on the ions. The electron pressure is temperature independent, whereas the ions behave as an ideal gas which has a pressure-temperature relation.

The zero-temperature model of a white dwarf is based on the equation of state for a degenerate electron gas (1.17) which gives the pressure (P) and density for a given composition and and energy distribution. (p_e) is the momentum of the electrons.

$$P = \frac{8\pi}{3h^3} \int_0^{P_F} \frac{(p_e^4/m_e)dp_e}{\sqrt{1+(p_e/m_e c)^2}} \tag{1.17}$$

The composition of the gas is specified using the molecular weight per electron μ_e. This is calculated as $\mu_e = \frac{A}{Z}$ where A is the mass number (protons + neutrons) and Z is the proton number. μ_e is a result of the composition of the white dwarf. For example, light elements have equal numbers of protons and neutrons resulting in roughly twice as many nucleons as electrons. A carbon composition will then have a μ_e value close to 2. For heavier elements, there are more neutrons per proton, so an Fe composition would result in $\mu_e = \frac{56}{26} = 2.152$. Note that μ_e is different to the mean molecular weight (μ) which is used for non degenerate stars and depends on the ratio of H, He and heavy metals as a fraction of the total mass.

The pressure from the equation of state is then combined with the equations describing the equilibrium structure of the white dwarf.

$$\frac{dP}{dr} = \frac{-Gm\rho}{r^2} \tag{1.18}$$

$$\frac{dm}{dr} = 4\pi r^2 \rho \tag{1.19}$$

The electron gas efficiently transports heat so the entire core is nearly isother-

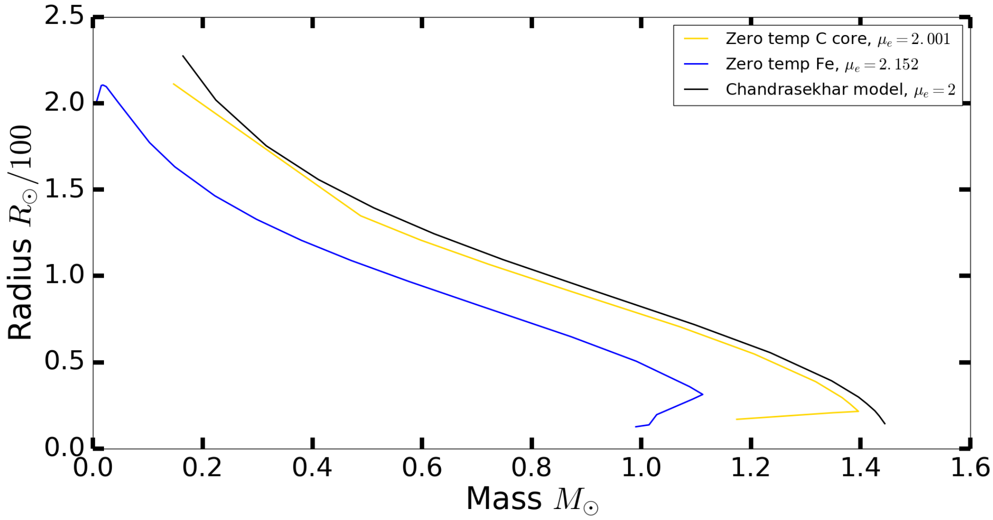

Figure 1.10: Examples of the white dwarf mass-radius relation for different core compositions (Hamada & Salpeter, 1961).

mal. It is only the thin non-degenerate surface layer which has a temperature gradient. This simplifies the calculation of the WD structure because it is not necessary to account for a variation in temperature with dr in equations (1.18) and (1.19).

Chandrasekhar (1931) combined the equation of state with the equations of equilibrium structure to show that the equation for the mass and radius of the star depends only on the composition (μ_e) and the core density (ρ). The core density depends on the mass, so for a given composition, the radius varies only with mass. This results in the mass-radius relation for white dwarfs shown in Fig. (1.10, black line) where $\mu_e = 2$ is assumed.

1.5.2 Refinements: Composition, Temperature and H-layer thickness

It was later shown (Hamada & Salpeter, 1961) that the composition of the ions does have a small effect on the MRR. The two main effects to be considered are the changes to the value of μ_e and the contribution of the ion pressure.

Including the composition of the ions in the equation of state produces a different MRR for each assumed core composition. The largest difference is seen for the hypothetical Fe composition which gives a reduced radius compared to the C/O composition expected for the majority of white dwarfs. Fig. 1.10 gives examples of the zero-temperature mass-radius relation for two different core compositions (Hamada & Salpeter, 1961).

The additional pressure of the ions as calculated by Hamada & Salpeter (1961) took no account of the temperature. The additional pressure due to the ions is much smaller than the degeneracy pressure from the electrons. However, it has been shown that it can significantly alter the radius for a given mass at the high temperatures (5000 - 100,000 K) found in white dwarfs. For a review see (Koester & Chanmugam, 1990). At high temperatures, the ions behave as an ideal classical gas so the equation of state must take into account the temperature in order to correctly predict the total pressure of the zero temperature electron gas and the finite temperature ions. As a result of this temperature dependence, additional equations describing the temperature structure of the white dwarf must be included when using equations 1.18 and 1.19. As the white dwarf cools below the crystallization temperature, the Coulomb forces between ions cause them to form a crystal lattice. At this point they become fixed in the lowest energy configuration and the MRR converges to the zero-temperature approximation.

The effect of temperature on the MRR can be clearly seen in Fig. 1.11. The solid coloured lines are the MRR for a C/O core WD starting at 10,000 K (red) and increasing to 50,000 K (blue) in steps of 10,000 K. For comparison, the zero-temperature model from (Hamada & Salpeter, 1961) is plotted as a thin black line. The lowest black line is the Fe core model.

One important result of the temperature dependence of the MRR is that a white dwarf will shrink as it cools down until it reaches the zero-temperature mass-radius ratio for its mass and composition.

1.5.3 The effect of the envelope on the MRR

The non-degenerate envelope makes up only a tiny fraction of the mass of a white dwarf. In the models of (Fontaine, Brassard & Bergeron, 2001) the mass fraction of a thick envelope is $q_H = 10^{-4}$ and a thin envelope is $q_H = 10^{-10}$. Despite this, the envelope can have a relatively large effect on the radius. The thick envelope models have a radius around 5 to 10 per cent larger than thin envelope models for typical 0.6 $M_\odot$ white dwarf. Fig. 1.11 shows the difference in radius between thin (dashed lines) and thick (solid) H-layer models. Envelope thickness decreases with increasing surface gravity $\propto g^{-1}$ so the MRRs converge towards the high mass end.

1.6 Observational tests of the MRR

The observational status of the MRR prior to *Hipparcos* was summarised by Schmidt (1996). It was shown that with the data available, the mass radius measurements

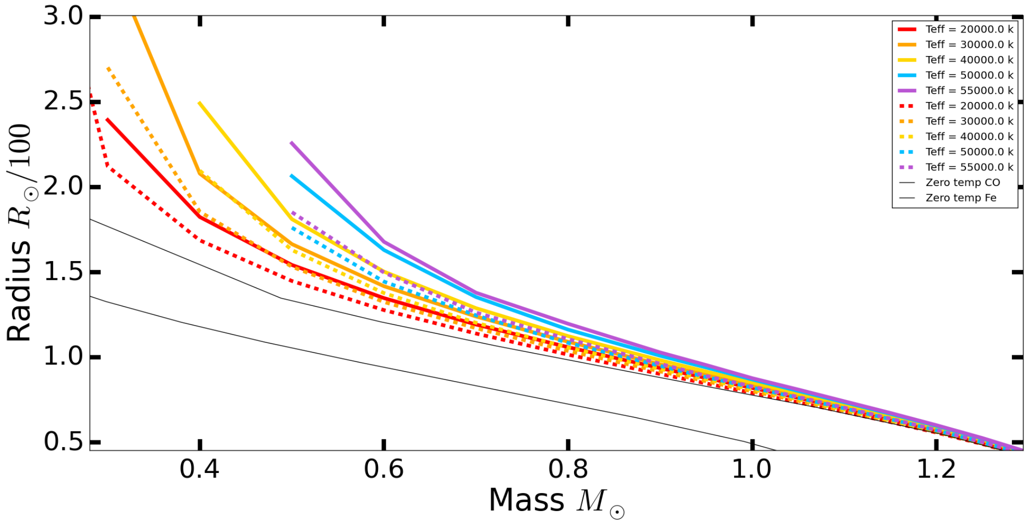

Figure 1.11: Example of MRR for white dwarfs of various temperatures and H-layer thickness (Fontaine, Brassard & Bergeron, 2001; Hamada & Salpeter, 1961).

were widely scattered and could not confirm the MRR. This large scatter was attributed to the uncertainty in the observations and Fig. (1.15, panel A) showed that the results were not incompatible with the MRR when the size of the errors was considered. Schmidt concluded that improved parallaxes and gravitational redshifts from high resolution spectra would be required to provide a meaningful test of the MRR.

Following the launch of *Hipparcos*, studies by Provencal et al. (1998) and Vauclair et al. (1997) were able to use parallax data with an accuracy of around 3.6 mili arcseconds for a sample of 20 white dwarfs. Vauclair et al. (1997) used the spectroscopic method and showed that the improved parallaxes greatly reduced the scatter in the mass-radius measurements. The data were in agreement with the general form of the MRR although the uncertainties were still too large to differentiate between zero-temperature and finite-temperature models.

Of the 20 white dwarfs observed by *Hipparcos*, only 4 had reliable mass determinations available. Provencal et al. (1998) pointed out that Sirius, Procyon, 40 Eri and Stein 2051 represented the "shaky underpinnings" of the empirical white dwarf mass-radius relation. At that time, the best available mass-radius measurements for these stars placed them significantly below the MRR, except for Sirius. The approach taken by Provencal et al. (1998) differs from Vauclair et al. (1997) in that the mass and radius are derived from the visual binary parameters (period, semimajor axis, fractional mass and stellar flux). The results are based on well understood physical principals and do not rely on the assumptions involved in broadening theory as required by the spectroscopic method. The improved parallax data led to revised mass-radius values which brought 40 Eri B and Sirius B into agreement with the Wood (1995) finite temperature models as opposed to the zero-temperature models as had previously been the case. A notable exception was Procyon B which was found to be consistent only with an Fe core zero-temperature model.

1.6.1 Combining spectroscopic and gravitational redshift methods

For a limited number of white dwarfs, it has been possible to study the MRR using both the spectroscopic and gravitational redshift in combination. Studies by Holberg, Oswalt & Barstow (2012) and Barstow et al. (2005) focused on white dwarfs in Sirius-Like binaries where accurate parallax data could be obtained for the bright main-sequence companion. The presence of a companion also makes it possible to disentangle the radial velocity component of the gravitational redshift. Holberg, Oswalt & Barstow (2012) studied 12 white dwarfs in this way and found agreement with C and C/O core MRRs within 1-2 σ.

The study by Barstow et al. (2005) focused on Sirius B which is the closest white dwarf and should provide high precision results to test the high mass end of the MRR. This study obtained the first space based spectrum of Sirius B free from contamination by light from Sirius A. The results for the mass and radius of Sirius B are shown in Fig. 1.12. There was a puzzling discrepancy between the mass obtained from the 2 methods. The spectroscopic result (green) was not compatible with the redshift mass (magenta) and neither method was within the 2σ error ellipse of the results from Holberg et al. (1998). The agreement could be improved if the radius measured from the flux of the G750M spectrum were used (upper pair of data points). However, the G430L spectrum was considered to be better calibrated so should have given the correct radius. One possible cause of the difference between the radii obtained from each spectrum was that some flux was lost from the G430L spectrum due to the use of the narrow 50 x 0.2 arcsec slit.

1.6.2 Studies using the dynamical method

Dynamical studies of Sirius B (Bond et al., 2017), Procyon B (Bond et al., 2015) and 40 Eri B (Bond et al., 2017; Mason et al., 2017) sucessfully derived white dwarf mass estimates from the binary orbit. The precision achieved by this method is $\sim$ 1 per cent for Sirius B and Procyon B and 3 per cent for 40 Eri B. This level of precision makes it possible to show that finite temperature models are a much better fit than zero temperature models.

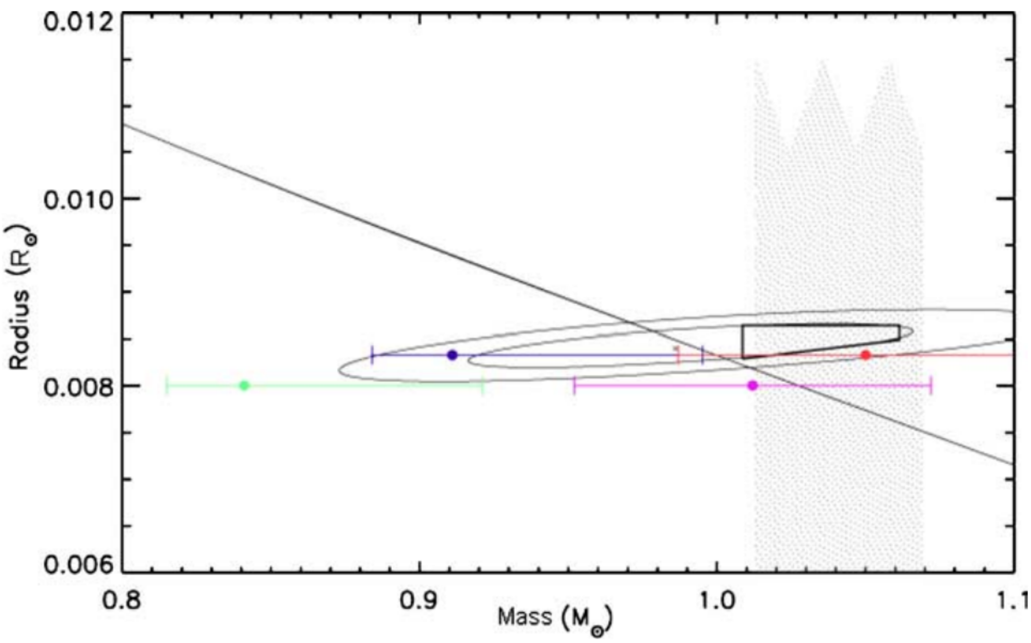

Figure 1.12: The mass of Sirius B measured using *HST* data in 2005. The lower set of data points are the mass from spectroscopy (green) and the mass from the gravitational red-shift(purple). Figure is reproduced from (Barstow et al., 2005)

The dynamical method provides the best high precision test of the MRR. Fig. 1.13 shows the results achieved to date which are all in agreement with the theoretical MRR appropriate for the temperature of the white dwarf.

Only a few white dwarfs have masses determined in this way because of the long observing campaigns required. Fig. 1.4 shows that the high precision provided by *HST* (red dots) has only been available for about half of the total orbit of Sirius B. A further limitation of the dynamical method is that it does not provide an independent measurement of the radius. This has to be provided by spectroscopy or photometry. This method is also currently limited to systems within a few hundred parsecs where the binary orbit can be resolved.

As noted in Barstow et al. (2005), one of the key causes of uncertainty in many studies is the error in the radius. The problem is made worse by the fact that most methods use the radius in the calculation of the mass. This results in both quantities being affected by the radius error in a way that tends to scatter the results orthogonally to the MRR. The error ellipses shown in Fig. (1.15, panel A) show the effect of this problem. This situation is gradually improving due to continuing efforts to improve the flux calibration (e.g. Bohlin et al. 2014; Narayan et al. 2016) and the availability of improved parallax measurements.

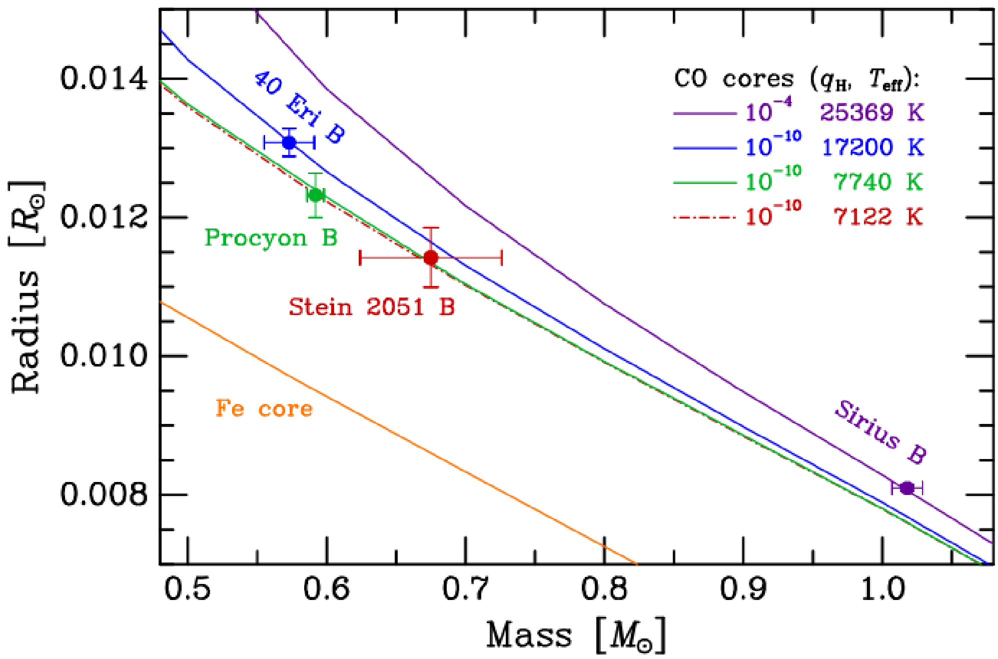

Figure 1.13: Tests of the MRR provided by the dynamical method. Figure reproduced from (Bond et al., 2017).

Another route to improved radius measurements is available for rare eclipsing binaries. The use of eclipse light-curves and gravitational red-shifts from spectroscopy made it possible to achieve a precision of 2.4 per cent in mass and 2.7 per cent in radius on average for a sample of 16 white dwarfs (Parsons et al., 2017). The high level of precision achieved made it possible to distinguish between models with different core composition and H-layer thickness. In particular, it was found that white dwarfs below 0.5 $M_\odot$ were consistent with He core models, while higher mass white dwarfs required C/O core models. This difference in core composition is expected according to theories of white dwarf formation. Formation of a white dwarf below 0.5 $M_\odot$ is thought to result when a higher mass star in the red giant phase goes through excessive mass loss before the core can be converted to C/O. An advantage of including these stars in studies of the MRR is that they help with investigating the low mass end of the MRR where the effects of temperature and core composition are greatest.

The first study to make use of the new parallax data from *Gaia* DR1 was Tremblay et al. (2017). This study highlighted the improvement in precision from using parallaxes with uncertainty of 0.5-0.7 mas. Despite this improvement, a definitive test of the MRR, and in particular the predictions of H-layer thickness, remained

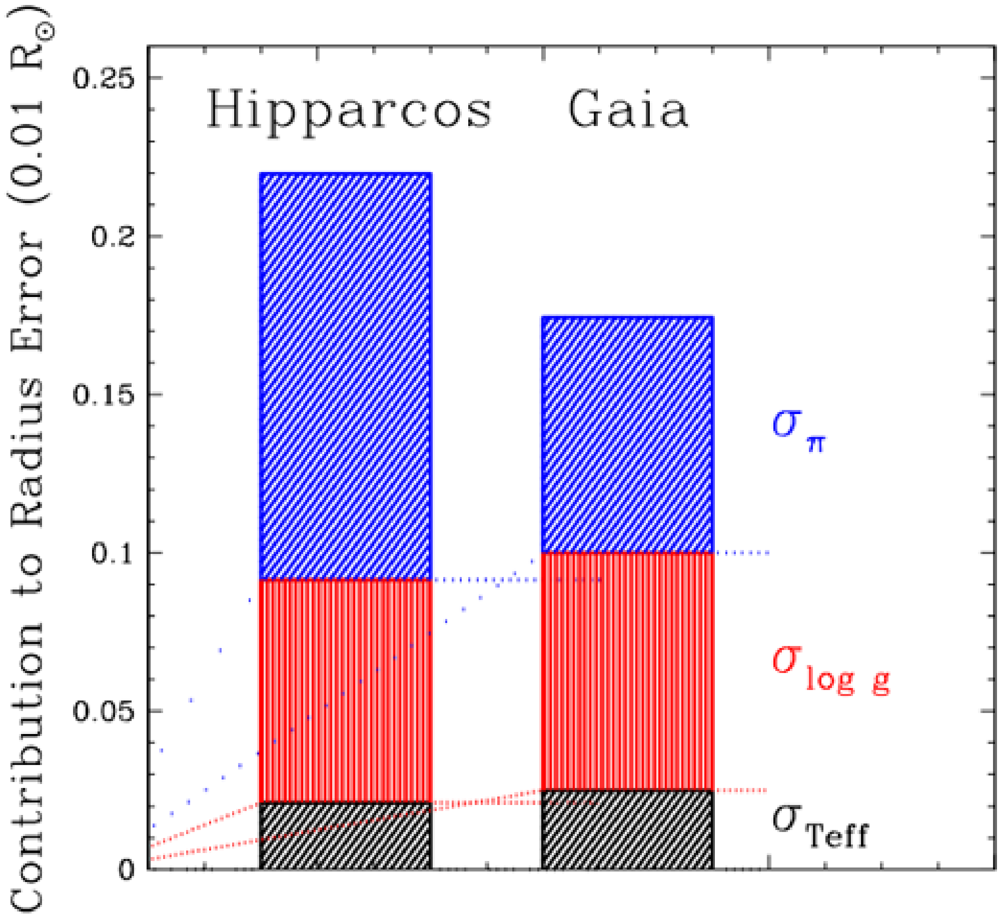

Figure 1.14: Contributions to the uncertainty in the radius. With *Gaia* DR1 parallaxes the error has been reduced to slightly below the level of error from the spectroscopic parameters ($T_{\rm eff}$ and log g). (Tremblay et al., 2017)

elusive. This was partly because DR1 contained only a limited number of white dwarfs and has not yet reached the micro-arcsecond precision expected for later data releases. A further problem highlighted by Tremblay et al. (2017) is that the uncertainty in the spectroscopic parameters is now the dominant source of uncertainty. Fig. 1.14, (Fig 5 from Tremblay et al. 2017), shows the contributions to the uncertainty in the radius. While the parallax uncertainty will become negligible in the near future, the error contribution from the spectroscopic parameters currently limits the accuracy to $\sim$ 8 per cent in radius (assuming an error of 0.001 and radius of 0.013 R$_\odot$). As noted, the radius error also contributes to the mass error in the spectroscopic method. This will continue to hamper tests of the MRR unless the determination of spectroscopic parameters can be greatly improved.

As the precision of large samples has improved, it has become possible not only to test the MRR, but also to identify sub-groups of stars which are definitely not consistent with the MRR. Bédard et al. (2017) used a sample of 219 DA and DB white dwarfs to test the MRR and found that 73 per cent were consistent with the MRR at the 1 σ level. They also identified 15 objects which were not consistent and are probably unresolved double degenerate systems. Fig. (1.15, panel C) (Figure 13 in Bédard et al. (2017)) shows the known and suspected double degenerates highlighted in solid red and dotted red respectively. Unresolved double degenerate spectra can be indistinguishable from single star spectra and give a log g value as expected. However, the increased luminosity causes the radius to be overestimated. These systems appear to the right and above the MRR.

The samples studied by Tremblay et al. (2017) and Bédard et al. (2017) both show some stars below 0.5 $M_{\odot}$ which fall significantly below the MRR. It has been suggested that they represent a population of Fe core white dwarfs since they appear to be a better fit with the Fe core MRR. This interpretation is problematic because there is currently no known formation route which would produce this kind of white dwarf. Further work is needed to learn more about these stars and determine whether they represent a genuine sub-group of white dwarfs or are the result of observational errors.

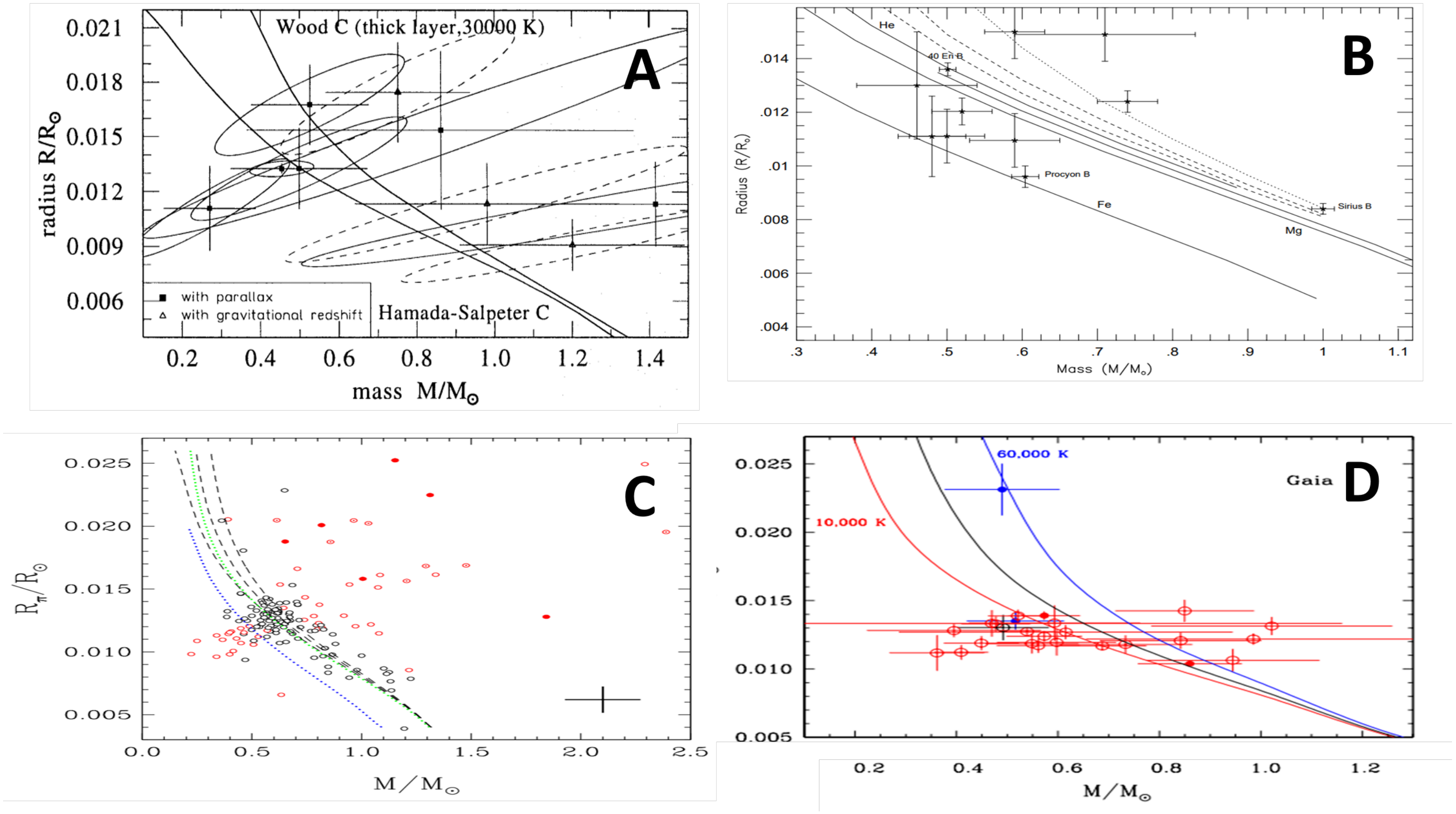

Figure 1.15: Observational tests of the MRR. (A) The size of the error bars due to the uncertainty in the parallax prior to *Hipparcos* (Schmidt, 1996). (B) Using *Hipparcos* parallax (Provencal et al., 1998). (C)Using *Gaia* parallax (Bédard et al., 2017), (D)(Tremblay et al., 2017).

Taken as a whole, the history of empirical studies of the MRR has shown a gradual convergence of results toward the theoretical MRR as the precision of the available data had improved. While high precision has been achieved for a few individual stars, the methods used are not yet applicable to large enough samples to definitively test the details of the MRR across the full range of mass, temperature, core composition and envelope thickness. We are now reaching the point where the level of precision for large samples of white dwarfs approaches that required to distinguish between the various details of the MRR. While the general form of the empirical MRR is no longer in doubt, it will be interesting to see where the final resting place of many of these well studied WDs falls on the mass-radius plane.

1.6.3 White dwarf formation and the mass-radius relation

The theory of stellar structure makes it possible to calculate the MRR for any combination of composition, envelope thickness and temperature. The question is, what range of values for each of these parameters correctly describes real white dwarfs? Some guidance to the expected parameter ranges comes from the theory of stellar evolution, which predicts certain compositions and envelope thickness's depending on the details of the white dwarf formation scenario.

The problem currently is that the observational data for white dwarfs do not constrain the parameters of the MRR. Therefore, the links between white dwarf formation and white dwarfs themselves remain poorly understood. An example of this is the possible evidence for the existence of Fe core white dwarfs based on observations of several stars which show they lie significantly below the C/O core MRR (Bédard et al., 2017; Provencal et al., 1998). However, the theory of stellar evolution does not predict the existence of such stars.

1.7 How white dwarfs and the MRR relate to other areas of astronomy and astrophysics

White dwarfs, together with the mass-radius relation, are the foundations of many areas of astrophysics. One of the most fundamental examples of the importance of white dwarfs is their role as the progenitors of supernovae type I_a (SN I_a). These supernovae are a vital link in the cosmological distance scale because they make it possible to measure the distances to local galaxies.

Within our own galaxy, white dwarfs provide a means to study the past stellar population. The white dwarf mass distribution shows that each generation of stars returns much of its material to the ISM. This chemically enriched material goes on to form subsequent generations of stars and planets. They also provide a method of deriving the age of stellar populations based on the white dwarf cooling age and the main sequence lifetime of its progenitor.

1.7.1 SN Ia progenitors

The key to the use of SN Ia as standard candles was originally based on the idea that they occur when a white dwarf exceeds the Chandrasekhar limiting mass. Since the exploding star must always be at the limiting mass, the resulting explosion would always have the same peak luminosity, and any difference in the observed apparent magnitude must be a result of the distance of the object. A measurement of the apparent magnitude provides a means of calculating the distance to the galaxy where the SN occurred. Phillips (1993) showed that the peak luminosity does in fact vary by $\pm$ 0.8 mag in the B band, possibly as a result of variations in the progenitor mass or explosion mechanism. Fortunately, the peak luminosity is related to the rate at which luminosity decreases in the 15 days after the peak. The decay rate of the light curve can therefore be used to infer the absolute magnitude reliably, even though the peak in the luminosity varies from one SN Ia to the next.

The two main scenarios for triggering a SN from a white dwarf are the single and double degenerate scenarios. In the single degenerate case (Whelan & Iben, 1973), the white dwarf accretes matter from a companion until it reaches the limiting mass. The double degenerate case (Iben & Tutukov, 1984) involves the in-spiral and collision of two white dwarfs which have a combined mass greater than the mass limit.

The importance of the MRR and white dwarf mass measurements to this area of research is that the value of the limiting mass changes slightly depending on the white dwarf composition. C/O core white dwarfs have a μ_e value of 2 resulting in a limiting mass of 1.46 $M_\odot$ from equation (1.20) (Chandrasekhar, 1931; Prialnik, 2009). A white dwarf with an Fe core has a $\mu_e = 2.15$ with a correspondingly lower limiting mass of 1.26 $M_\odot$.

$$M_{Ch} = 5.83\mu_e^{-2} \qquad (M_\odot) \tag{1.20}$$

1.7.2 Cosmochronology

The theory of white dwarf cooling has many practical applications because it allows the age of a white dwarf to be derived from measurements of its temperature and

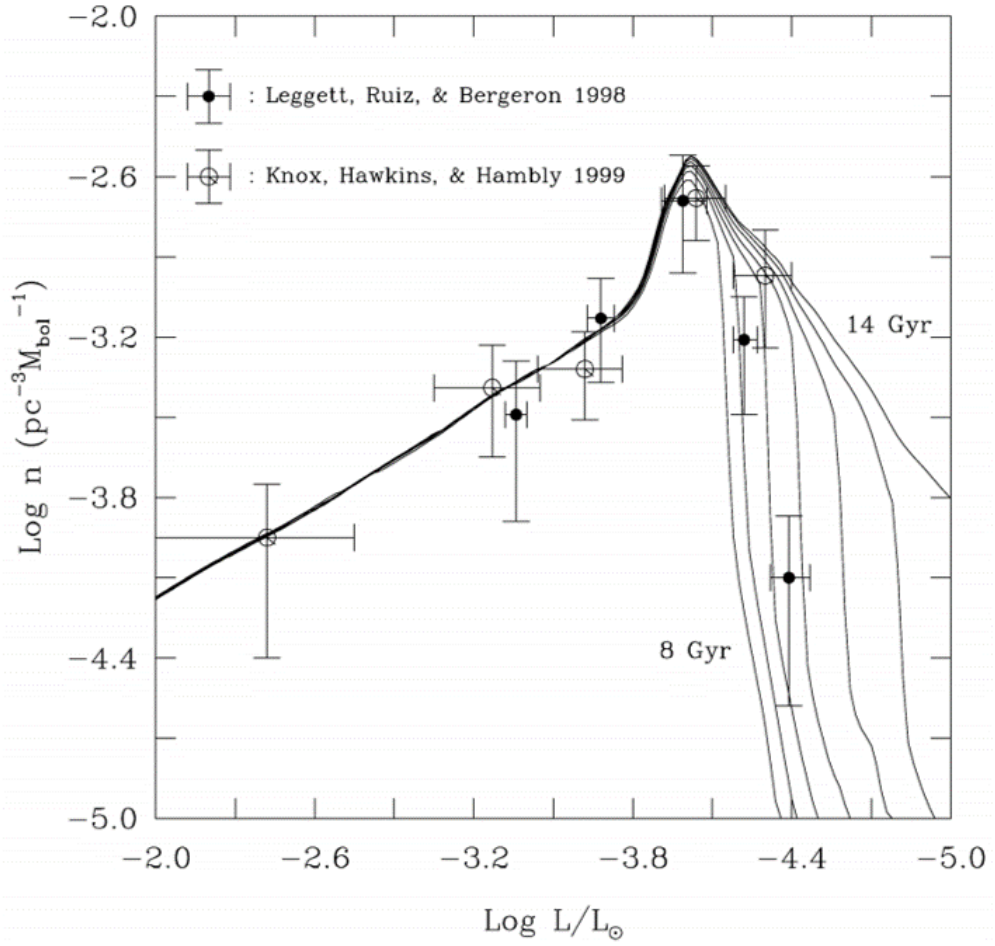

Figure 1.16: White dwarf luminosity function for solar neighbourhood. (Fontaine, Brassard & Bergeron, 2001) (Fig 9)

mass. If a white dwarf is in a binary, it is possible to estimate the total age of the binary system. The total age of the binary is the sum of the white dwarf cooling age plus the main sequence lifetime of its progenitor. This method requires accurate measurements of the white dwarfs mass to determine the appropriate cooling track, and also to estimate the lifetime of the progenitor through the initial-final mass relation. The main sequence lifetime of the white dwarf progenitor is dependent on the mass of the star assuming it has not interacted with the binary companion.

White dwarfs are also important tools for estimating the age of the disk of the galaxy. The method is to measure the luminosity function of the population of white dwarfs in the solar neighbourhood and compare it to theoretical models. Fig. 1.16 shows that the luminosity function increases towards lower luminosity as there are more cool white dwarfs than hot ones. After a certain peak the luminosity function decreases because the disk is not yet old enough for white dwarfs to have cooled down that much. The model luminosity functions show how the shape of the cut-off depends on the assumed age of the stellar population. The downturn occurs at a temperature of approximately 4000 K which makes cool white dwarfs particularly important for this kind of study.

It is important to have a reliable MRR because the WDs at the lowest temperatures do not show visible absorption lines, so the spectroscopic method can not be applied to determine their mass. If the distance and luminosity are known, they can be used to calculate the radius. Then the MRR can be used to calculate the mass from the radius. The coolest WDs are also the oldest and therefore most important for determining the age of the disk. The investigations in this thesis will potentially contribute to the development of cosmochronlogy by helping to provide observational tests of the MRR and the theoretical cooling models. The main limitations of these models which can be addressed through studies of the MRR are the details of the core composition and the DA hydrogen layer thickness. In addition, the practical application of cosmochronology can be improved by making use of well calibrated mass-radius relations suitable for white dwarfs across the full range of mass and temperature.

1.8 Aims of this thesis

Given the fundamental importance of the MRR to our understanding of white dwarfs, it is vital to conduct observational tests to confirm its validity. The theory is well developed and now includes a number of refinements which have the potential to make it an even more useful tool for the study of white dwarfs. These detailed corrections to the original Chandrasekhar MRR include the effects of temperature, core composition and H envelope thickness.

Despite many decades of studies designed to test the MRR, the uncertainty in the available data has generally been too large to provide a definitive test, except in specific cases such as eclipsing binaries or dynamical mass determinations. Since the launch of *Hipparcos* in 1996, it has become possible to test the general form of the MRR, although data precise enough to distinguish between the detailed corrections has remained sparce.

A recent key development is the availability of high precision paralax data from *Gaia* which is now available for a limited number of white dwarfs. With subsequent data releases, this level of precision in the distance measurements will become available for thousands of white dwarfs.

This thesis has two main aims. Firstly, to test the MRR using new high precision data from *Gaia* and *HST* which will provide some of the most accurate tests yet of the MRR. These tests will make use of the spectroscopic and gravitational redshift approaches. Following on from this, I will investigate the systematics and unertainties affecting each method of testing the MRR. This will enable improvements to be made so that it is possible to take full advantage of the new parallax data provided by *Gaia* in the coming years.

Chapter 2

A spectroscopic test of the MRR, comparing optical and far-UV results with *Gaia* DR2, *HST* and *FUSE*

2.1 Overview

In this chapter I will test the MRR using the technique of fitting models to the hydrogen Balmer and Lyman lines to obtain the surface gravity which can be used to calculate the mass. This approach is used to begin with because it is a well understood method which has been applied to the study of the MRR before. There is suitable spectroscopic data available for a larger sample of stars than can be studied via the other methods. Where this study differs from previous work is that it makes use of the *Gaia* DR2 parallaxes which it is hoped will greatly reduce the main source of uncertainty. I will use newly acquired *HST* spectra which have the potential to provide high precision spectroscopic parameters for a number of newly discovered white dwarfs. The spectroscopic method also provides measurements of the temperature and flux which will be needed later to successfully apply the gravitational redshift method.

2.2 Introduction

Observational tests of the MRR (e.g. Schmidt 1996; Vauclair et al. 1997; Provencal et al. 1998) have relied heavily on the use of the spectroscopic method. The Balmer lines in optical spectra are the most easily studied and are available for large samples of stars. Studies prior to *Gaia* DR1 found that the error introduced by the distance measurements made most tests of the MRR inconclusive. Following DR1, Tremblay et al. (2017) and Bédard et al. (2017) have shown that the data are in agreement with the MRR, but the uncertainty is still too large to distinguish between details such as the H-layer thickness and temperature dependence. The uncertainty is mainly due to the spectroscopically derived parameters. This will make it difficult to fully exploit future *Gaia* data releases to their fullest potential for the purposes of testing the MRR.

To make progress with spectroscopic tests of the MRR, it will be necessary to reduce the uncertainty in the spectroscopic parameters beyond what has been achieved so far. One way of verifying results and identifying causes of uncertainty is to compare the spectroscopic mass for a particular WD to the values obtained from the other methods. Some of the best WDs for this kind of study are found in Sirius-Like Systems (SLSs) which consist of a WD and a main sequence star of spectral type K or earlier (Holberg et al., 2013). Sirius itself is particularly useful for studying the MRR because of its high mass and close proximity to Earth. Like other SLSs, the mass of Sirius B can in principal be derived using the spectroscopic, dynamical and gravitational redshift methods. An added advantage is that the bright main-sequence companion is more likely to have a parallax measurement available than individual WDs.

The small apparent binary separation (often less than 1 arc sec), and the faintness of the WD compared to the main-sequence companion in the optical, has made the study of many SLSs impossible until the advent of space based far-UV and optical spectroscopic instruments. a successful campaign to resolve the WD in more suspected SLSs was carried out by (Barstow et al., 2001). Later observations were able to obtain the first optical spectra of the WD component in 3 new systems which will be used in this analysis.

Even with *HST*, many SLSs remain unresolved. Such WDs can only be studied in the far-UV where the contribution from the MS star is negligible. It is still possible to apply the spectroscopic method as the far-UV covers the Lyman series of absorption lines. In principle, the spectroscopic method can be applied in the same way as to the Balmer lines in the optical.

In this study I use Balmer/Lyman line fitting to test the MRR and also to cross check the results from optical and far-UV spectra. It is vital to test the validity of the Lyman line results because a large archive of WD spectra taken by *FUSE* exists from which we can derive accurate log g and temperatures e.g. (Barstow et al., 2003, 2010). The WDs in this archive cover a wide temperatures range (16,000 - 77,000 K) and will be ideally suited for testing the temperature dependence of the MRR. Until recently, the necessary distance information for this sample was not available. Now that the parallax measurements needed to employ the *FUSE* data for testing the MRR have arrived, it is important to compare the uncertainties and systematics of the hydrogen line fitting as applied to both Lyman and Balmer line analysis.

For Sirius B and HZ 43 there are several spectra available which I use to assess the repeatability of spectroscopic results. This follows on from the recent work of Tremblay et al. (2017) which showed that for Wolf 485A the spread in $T_{\rm eff}$ and log g values measured from several spectra was larger than the error estimates from fitting individual spectra.

2.3 Observations

2.3.1 Overview

The majority of the WDs in this sample were not included in the samples of Tremblay et al. (2017) and Bédard et al. (2017) because optical spectroscopy was not available. The exceptions to this are Sirius B, Feige 24 and HZ 43. The optical spectra for Sirius B and HZ 43 used in this analysis are from *HST* and provide a comparison to the ground based results presented in those studies. Optical spectra for 14 Aur Cb, HD 2133 B and HR 1358 B were obtained by *HST* and no previous optical spectra exist.

The sample contains 11 targets, 3 of which have both *HST* and *FUSE* spectra available. This subset of targets will be used to study potential systematic differences between the results from the Lyman and Balmer lines. Sirius B and HZ 43 both have 4 individual *HST* spectra available taken with the G430L grating. All of these targets are DA white dwarfs with hydrogen dominated atmospheres.

We make use of spectra listed in in Table 2.1 from *HST* and *FUSE* as well as *Gaia* DR2 parallax data in Table 2.2. The *HST* data consist of STIS spectra taken with the G430L grating covering the 2900-5700 Å range which includes the Balmer lines from β to the series limit. The *FUSE* spectra cover the wavelength range 912-1180 Å which corresponds to the Lyman series from Lyman β to the series limit.

Table 2.1: List of white dwarfs and the spectra used in this study.*FUSE* spectra start with a capital letter, *HST* spectra start with "o".

WD number	Name	HST obsID	Grating/slit	date
HST + FUSE				
WD 0022-745	**HD 2133 B**	obt802010	G430L / 52x0.2"	2012-09-23
		obt802020	G430L / 52x0.2"	2012-09-23
		B0550201000		
WD 0418+137	**HR 1358 B**	obt808050	G430L / 52x0.2"	2012-11-20
		obt808060	G430L / 52x0.2"	2012-11-20
WD 0512+326	**14 Aur Cb**	otb804050	G430L / 52x0.5"	2012-11-22
		obt804060	G430L / 52x0.5"	2012-11-22
		A05407070		
WD 1314+293	**HZ 43**	o57t01010	G430L / 52x2"	1998-12-17
		o57t02010	G430L / 52x2"	1998-12-19
		o69t07020	G430L / 52x2"	2000-11-06
		o69t08020	G430L / 52x2"	2000-12-10
		M1010501000		
		P1042301000		
		P1042302000		
HST				
WD 0642-166	**Sirius B**	obt801010	G430L / 52x2"	2013-01-26
		obt801020	G430L / 52x2"	2013-01-26
		obt801030	G430L / 52x2"	2013-01-26
		obt801040	G430L / 52x2"	2013-01-26
FUSE				
WD 0226-615	**HD 15638**	A05402010		
WD 0232+035	**Feige 24**	P10405040		
WD 0353+284	**RE 0357**	B05510010		
WD 1021+266	**RE 1024**	B05508010		
WD 1921-566	**REJ 1925**	A05411110		
WD 2350-706	**HD 223816**	A05408090		

Table 2.2: Comparison of parallax values from *Hipparcos*(new reduction, van Leeuwen 2007) and *Gaia* DR2 . Binary parameters (Holberg et al., 2013) and references therein. (ρ) is the apparent separation of the two stars.

Name	Hipparcos π (mas)	Gaia DR2 π (mas)	ε_i (mas)	Period (years)	SpT	(ρ) (arc sec)
HD 2133	7.32 ± 0.93	7.641 ± 0.027	0.0	665.03	F7V	0.6
HD 15638	4.85 ± 0.78	6.426 ± 0.178	0.99	<52.3	F6V	<0.08
Feige 24	10.9 ± 3.94	12.669 ± 0.054	0.13	-	dM	-
RE 0357	n/a	9.287 ± 0.076	0.11	-	K2V	Unresolved
HR 1358	21.09 ± 0.51	21.052 ± 0.077	0.12	274.53	F6V	1.276
14 Aur C	9.63 ± 2.92	12.246 ± 0.093	0.0	2432.72	F2V	2.0
Sirius	379.21 ± 1.58	n/a	-	50.1	A0V	7.5
RE 1024	n/a	6.709 ± 0.080	0.15	-	F0V	<0.08
HZ 43	25.96 ± 6.38	16.756 ± 0.074	0.26	-	-	-
REJ 1925	n/a	7.639 ± 0.121	0.42	118.63	G5V	0.217
HD 223816	n/a	6.586 ± 0.030	0.1	-	G0V	0.574

2.3.2 Spectra

HST data exists for 5 targets which were all observed with the G430L grating as part of program 12606 in cycle 19 (PI Barstow), except for HZ 43 which was observed as part of the calibration of the *HST* flux standards (Bohlin et al., 1995, 2014) for program 8066 and 8849. Sirius B and HZ 43 have exceptionally high quality spectra with 4 spectra each at S/N > 100 due to their brightness. The number and quality of the spectra for these 2 targets allow us to test the intrinsic reproducibility of measurements from repeated observations of the same target.

There are 6 targets for which only *FUSE* spectra are available. Processing of the data followed the procedures in Barstow et al. (2002, 2003). The *FUSE* spectra have been re-binned to a resolution of 0.04 Å because the spectra provided by the MAST archive are oversampled.

2.3.3 Parallax

The distances used in this study are calculated from the parallax measurements shown in Table 2.2 provided by the *Gaia* satellite (Prusti et al 2016). The *Gaia* mission measures the positions of over a billion stars by repeatedly scanning the whole sky. The changes in position of each star over the course of the 5 year mission will allow the parallax and proper motion to be measured to an accuracy of a few micro-arc seconds compared to the mili-arc second accuracy achieved by the *Hipparcos* mission.

Gaia data release 2 (DR2) was made publicly available on April 25th 2018 (Gaia Collaboration et al., 2018). It is an improvement on the preliminary data release (DR1) which had to rely on measurements from the *Hipparcos* and Tycho catalogues to provide a long enough baseline (Gaia Collaboration, Brown et al., 2016) and only included the first 14 months of *Gaia* data. DR2 benefits from 22 months of *Gaia* observations and improved calibration.

The WDs in this sample are in close binaries and none are included in the *Gaia* catalogue as individual stars. For these Sirius-Like Systems we can use the parallax measurement for the MS star to calculate the distance for the WD since the difference in distance is negligible.

The astrometric solution in DR2 is based on the assumption that all sources are single stars and does not take into account binary motion. The DR2 catalogue includes a parameter called "astrometric excess noise" (ε_i) where values greater than 1 indicate that the solution has been affected by binary motion. This is unlikely to be a problem for the stars in this sample which have long orbital periods. It can be seen from Table 2.2 that all stars in this sample have astrometric excess noise values less than 1 and the parallax measurements can be considered reliable, although it should be noted that HD 15638 has a much higher ε_i value than the rest of the sample.

2.3.4 Background subtraction for HR 1358 B spectra

Inspection of the 2D spectra for HR 1358 B shows that there is a high level of background scattered light along the whole length of the spectrum. This can be seen as lines either side of the white dwarf spectrum in Fig. 2.2 (top row). There is also a fainter pattern of scattered light which goes across the extraction region and varies along the length of the spectrum.

It is not clear what caused the extra light which can be seen as lines either side of the white dwarf spectrum. The STIS instrument handbook shows an example of the "railroad track" effect which is almost identical to the observation of HR 1358 B shown in Fig. (2.1) and is noted as most likely due to multiple reflection in the instrument. The cross dispersion plot (right panel) shows that the lines themselves do not cross over the 7 pixel wide extraction region used for the white dwarf spectrum so they do not need to be subtracted. However, in the HR 1358 B spectra, there is also a further background component which varies along the dispersion direction and does appear to cross over the white dwarf line. This is the component which the adopted background correction procedure is designed to model and remove.

The approach developed to remove the scattered light from these observations

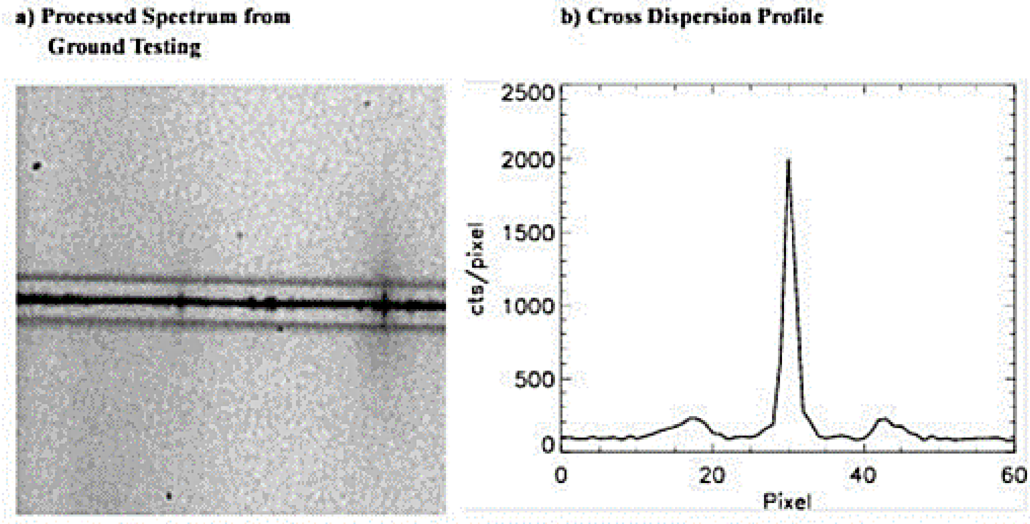

Figure 2.1: Example of STIS spectrum displaying "railroad tracks" either side of the main target spectrum. The right hand panel is a cross dispersion profile showing the flux measured by taking a vertical slice across the 2D spectrum. Figure reproduced from the STIS instrument handbook, cycle 26 (Fig 13.103, Chapter 13.7)

consists of several steps as follows. The overall aim is to make a model of the faint background which can be subtracted from the 2D spectrum, leaving just the white dwarf line. First the background is sampled by taking vertical slices one pixel wide at various points along the dispersion axis of the spectra. Extra slices were included at wavelengths close to the cores of the Balmer lines as shown in Fig. 2.2 (2nd row). Each vertical slice is plotted to show the variation in pixel intensity with vertical position on the CCD. These plots show that in general there is a strong peak corresponding to the white dwarf line, with a smaller peak either side. Underlying these 3 peaks is also a fainter background component which is highly variable from one slice to the next. Fitting Voigt profiles to these three peaks shows that the wings of the peaks either side are not wide enough to contribute to the flux within the extraction region. However, the fainter background component continues right through the white dwarf line and is the main component that needs to be removed.

Fitting Voigt profiles to the three peaks identifies the regions where the wings of these peaks contribute to the low level background. The level of the faint background is then estimated by taking only the regions where the flux contribution from the three peaks is less than 9×10^{-15} erg cm^{-2} s^{-1} as shown in Fig. 2.3. No attempt is made to fit a Voigt profile to the faint background component because its shape is different in every slice. Instead, the flux in the faint background component was estimated by fitting a polynomial to the points in-between the Voigt profiles,

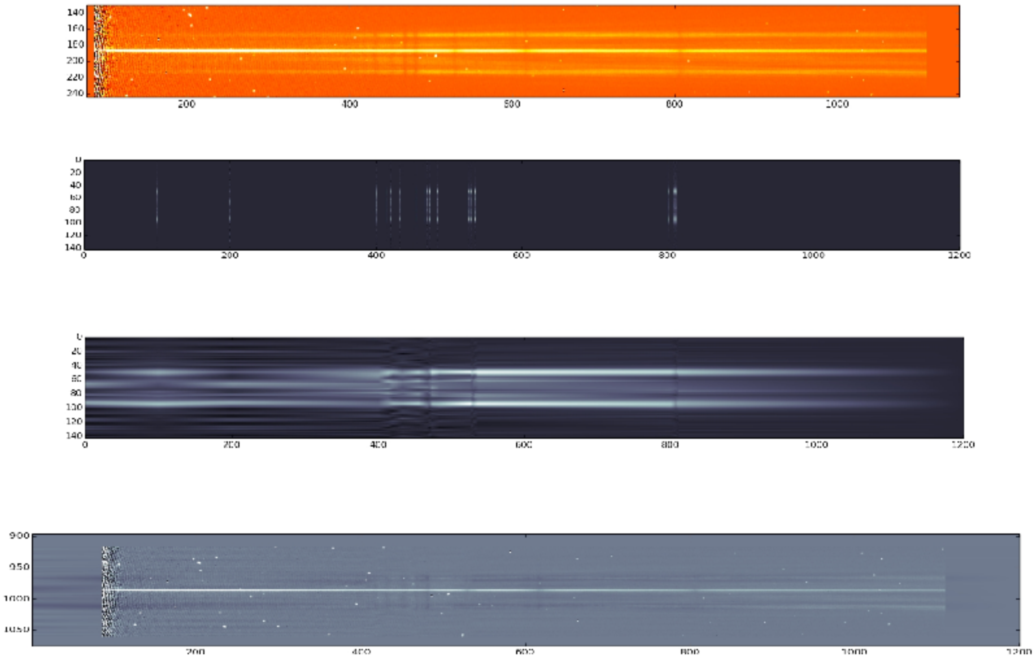

Figure 2.2: HST spectrum of HR1358 B. (Top) The original spectrum showing scattered background light. (Second row) Vertical slices taken to sample the background for modeling. (Third row) Model of the background interpolated between the vertical slices. (Bottom) The final spectrum after background subtraction.

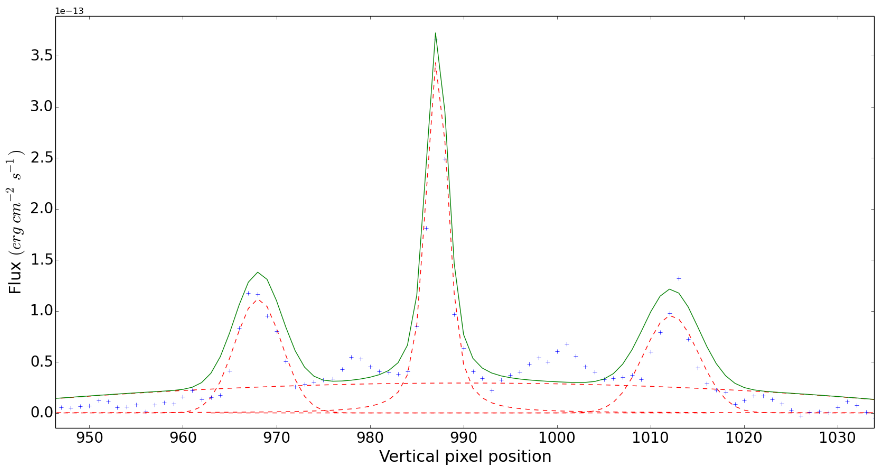

Figure 2.3: Example of ftting Voigt profiles to one of the vertical slices taken to model the background. The Voigt profiles are used to measure the spread of the 3 main peaks so that the regions where the flux can be attributed entirely to the faint background can be identified.

where the flux is assumed to be only from the faint background and contains no contribution from the 3 main peaks. The polynomial fit then allows us to interpolate the background flux level across the white dwarf line as shown by the dashed red curve in Fig. 2.3.

Since the vertical slices only sample the background at specific wavelengths, the gaps between slices are filled in by liner interpolation, which produces a complete 2D model of the background as shown in Fig. 2.2 (3rd row). When this background array is subtracted from the original spectrum, it leaves only the pure white dwarf line with a slightly reduced flux level (4th row in Fig. 2.2).

2.4 Analysis

2.4.1 Fitting procedure

Testing the MRR requires accurate measurement of the mass and radius for a sample of WDs. The spectroscopic method (Holberg et al., 1985; Bergeron, Saffer & Liebert, 1992) is based on measuring the depth and broadening of the hydrogen absorption lines observed in the spectra of DA WDs. The amount of broadening in the absorption lines is a direct consequence of the gravitational field of the WD which keeps the atmosphere at such high pressure that the energy levels of the hydrogen atoms are distorted, causing them to absorb photons of a wider range of frequencies. The depth and shape of the lines also depends on the temperature which determines what proportion of atoms in the atmosphere are in a particular state.

By fitting models generated by stellar atmosphere codes such as TLUSTY we can determine the best fitting values for log g and $T_{\rm eff}$ which will reproduce the observed line shapes. The model fitting also includes a normalization parameter, which enables the calculation of the radius of the star if its distance is known.

The spectra of white dwarfs have the characteristic shape of a blackbody with the absorption lines, formed in the atmosphere, superimposed. The spectrum between the absorption lines is not flat but will have a slope dependent on the temperature of the white dwarf. The spectroscopic method relies on fitting the shape of the absorption lines rather than the slope of the blackbody continuum. There are several approaches to dealing with the continuum. The method developed by Bergeron, Saffer & Liebert (1992) was to use a blackbody model to normalise the spectrum, which removes the shape of the continuum. The normalised spectrum is flat with the now symmetrical absorption lines still visible.

The procedure used in this work is based on that developed in Marsh et al. (1997) and applied by Barstow et al. (2005) for *HST* spectra of Sirius B and

(Barstow et al., 2003, 2010) for the *FUSE* data. The models used include the shape of the blackbody continuum. However, there are many more data points in the continuum compared to the absorption lines which can cause the fit to be inaccurate in the lines in favour of improving the fit to the continuum. The method for reducing the influence of the continuum on the fit is to remove sections of the spectrum which are between the absorption lines and therefore contain only data points from the continuum. The absorption lines are the most sensitive to the log g and $T_{\rm eff}$ parameters so the fitting is restricted to only include these regions of the spectrum.

Model grids produced from the TLUSTY models are loaded in to the XSPEC (Arnaud, 1996) fitting software. The spectra are fitted following the standard χ^2 minimisation procedure.

Fitting *HST* Balmer line spectra

The spectra were checked for any contamination from the bright main sequence companion star. This was found to be negligible for all targets except HR 1358 B. Therefore, a special background subtraction method had to be applied to the spectra of this star (Joyce et al., 2017).

Fitting results are shown in Table 2.3. The results for targets with multiple spectra are taken as the average from fitting each of the spectra individually. Where a target has only one spectrum the quoted errors are the statistical uncertainty in the fit as calculated by XSPEC. When multiple spectra have been averaged the quoted error is the error in the average.

Fitting *FUSE* Lyman line spectra

For the Lyman line spectra a slightly different fitting method has to be utilised as the satellite had different channels and detectors to record each part of the spectrum. Full details of the optical arrangement for *FUSE* are given in Moos et al. (2000) but some details of particular relevance are discussed here.

There are 4 channels with different mirror and grating coatings which are optimized to reflect light in certain wavelength ranges. During operations it was found that it was not always possible to keep all 4 channels correctly pointed at the target for the whole exposure, leading to a loss of flux in some wavelength ranges. The consequence for this analysis is that the flux measured in a spectrum can vary depending on which region of the spectrum is used. This is most noticeable in the spectrum of 14 Aur Cb shown in Fig. 2.4 where the flux in region 980-1082 Å is

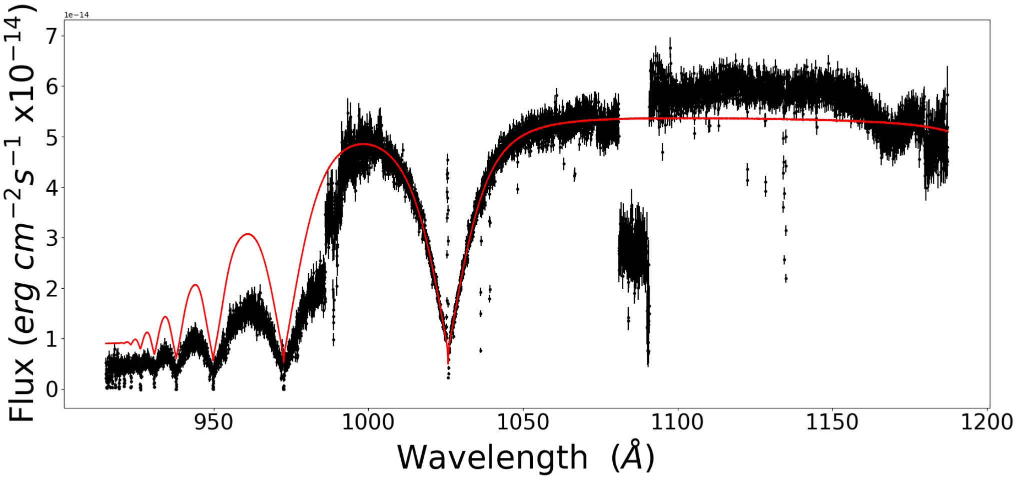

Figure 2.4: *FUSE* spectrum of 14 Aur Cb showing the difference in detected flux for sections of the spectrum recorded by different channels. The sections between 910-990 Å and 1080-1100 Å have a lower flux compared to the section between 990-1080 Å (Lyman-β) due to the target not being aligned in those channels for the full duration of the exposure. The red line is a model normalised to the Lyman-β line to highlight the difference in flux between this line and the rest of the Lyman series towards shorter wavelengths.

clearly lower than the flux in the rest of the spectrum. This spectrum is made up of several sections according to the wavelength ranges recorded by the different instrument channels. The model (red line) shows the normalisation when fitted to the Lyman-β line only and is not a good fit to the rest of the Lyman lines which are recorded by a different channel.

The model used here only has a single normalisation parameter and cannot account for the large difference in flux between different regions. The method developed to overcome this is to fit a separate model to each section of the spectrum which allows the normalisation to be altered for each independently. The 2 models are set up so that the T_{eff}, log g and abundance parameters are linked and cannot vary independently. The z and norm parameters can vary independently so the resulting fit can adjust to the different flux levels but log g and T_{eff} are still derived from fitting all of the available absorption lines simultaneously.

Another issue that affects the Lyman lines but not the Balmer lines is geocoronal emission which causes strong narrow emission lines in the cores of the broad WD absorption lines (see Fig. 2.4 at $\sim$ 1025 Å). These emission lines are not included in the model since they are not emitted by the WD. Therefore, the emission lines are excluded when fitting the model to the absorption line. After exclusion of the spikes the spectra that are actually used for fitting have small gaps in the core of each Lyman absorption line.

2.4.2 White dwarf synthetic spectra

For this study I use stellar models generated with the TLUSTY (Hubeny & Lanz, 1995) code and the resulting spectral models are calculated using SYNSPEC (Hubeny & Lanz, 2017).

These model fitting results were obtained using a non-LTE pure-hydrogen WD grid. This grid covers the temperature range 18,000–80,000 K and log g 7–9. This grid uses updated broadening tables (Tremblay & Bergeron, 2009) and including additional updates from Tremblay in 2015 (private communication). All models were generated to cover both the Lyman and Balmer line regions covering the wavelength range 3000 to 7500 Å so that the same model grid could be used for fitting both the *HST* and *FUSE* data and avoid possible systematic differences.

For the Balmer line spectra an initial fit was done with a coarse grid which has a lower resolution in log g space of 0.25. This allowed the grid to cover the full range of possible $T_{\rm eff}$ and log g values. Once an initial fit had been done, a high resolution grid with log g spacing of 0.01 was produced for each target covering a smaller range of parameter space.

For the Lyman line spectra there are existing values of $T_{\rm eff}$ and log g available in Barstow et al. (2003, 2014). These results were obtained with a non-LTE H/He model grid using the older Lemke (Lemke, 1997) broadening tables. I repeated the fitting using an updated pure H grid based on the 'Tremblay' broadening tables and the new $T_{\rm eff}$ and log g results are presented in Table 2.3.

2.4.3 Calculating mass and radius

Calculating the radius of the WD requires measurements of the flux received and the distance from the WD to the observer. The models give the predicted flux emitted per unit area by the WD and include a scaling factor to adjust for the fraction of flux per unit area at the distance of the detector. This scaling factor is listed in the 'norm' column in Table 2.3 and is used to calculate the radius using equation (2.1).

$$norm = \frac{R^2}{D^2} \tag{2.1}$$

Spectra from *HST* and *FUSE* are flux calibrated so the normalization of the best fit model can be used to calculate the radius. The final ingredient for equation

(2.1) is the distance D. This is provided by the *Gaia* satellite using the parallax method.

The radius is required as input to the mass calculation via equation (2.2).

$$g = \frac{GM}{R^2} \tag{2.2}$$

Equation(2.2) is used to calculate the mass using the radius calculated in equation (2.1) combined with the log g parameter found from model fitting of the spectrum. G is the gravitational constant.

2.5 Results

The results of fitting the spectra with the model grid are given in Table 2.3. For each target the results of fitting each individual spectrum are listed. The WDs in this sample cover a temperature range of 20,922 K for HR 1358 B to 73,999 K for HD 223816. Log g ranges from 7.5 for RE 1024 to 8.6 for Sirius B.

The mass-radius results in Table 2.4 were calculated by combining the atmospheric parameters Table 2.3 and the parallaxes in Table 2.2. The *Gaia* DR2 parallax is used for all targets except Sirius which was not included in DR2. The mass-radius results from Table 2.4 are shown in Fig. 2.5. The data are plotted with the theoretical MRR (Fontaine, Brassard & Bergeron, 2001) which was calculated for carbon/oxygen core WDs for a range of $T_{\rm eff}$. The temperatures plotted here are 15, 25, 45 and 55,000 K from dark to light grey. Dashed lines represent thin H-layer models ($qH = MH/M* = 10^{-10}$) and solid lines are thick H-layer models ($qH = MH/M* = 10^{-4}$).

HST Balmer line spectra are plotted as filled shapes and *FUSE* Lyman line results are unfilled shapes. Each target is plotted as a different shape as shown in the legend. For targets that have Balmer and Lyman spectra they are plotted as two separate points of the same shape (filled or unfilled respectively).

To search for any effects due to temperature, the mass-radius results are plotted again in Fig. 2.6. The WDs are binned into temperature ranges of 10,000 K as indicated by the marker shapes (and colours in the on-line version). The MRRs are for thick H-layer and are calculated for the temperature in the middle of each 10,000 K bin. The colours match the temperature ranges of the data points. Also plotted are the zero temperature carbon core and Fe core relations of Hamada & Salpeter (1961) as the lowest (thin black) lines.

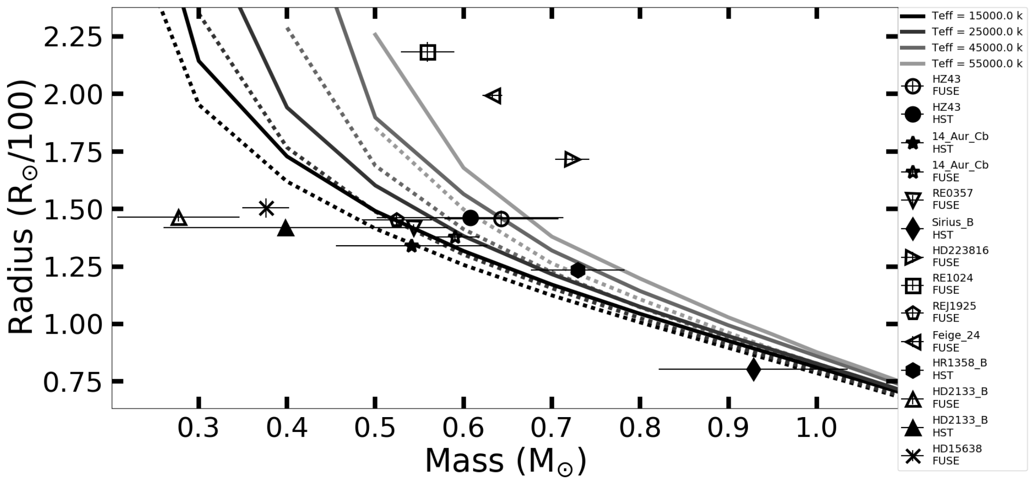

Figure 2.5: The mass-radius relation with both *HST* and *FUSE* data. Data comes from Table 2.4 and is based on fitting with the pure H non-LTE model grid using (Tremblay & Bergeron, 2009) broadening tables. Theoretical MRR models (Fontaine, Brassard & Bergeron, 2001) are shown for temperatures of 15,000, 25,000, 45,000 and 55,000 K from dark grey to light grey. Dashed lines are thin H-layer and solid lines are thick H-layer. Shapes of the symbols represent different white dwarfs as listed in the legend. The *FUSE* Lyman line results are (unfilled) and the *HST* Balmer line results are (solid). Where a target has data available from both *HST* and *FUSE* they are plotted as 2 separate data points of matching shape.

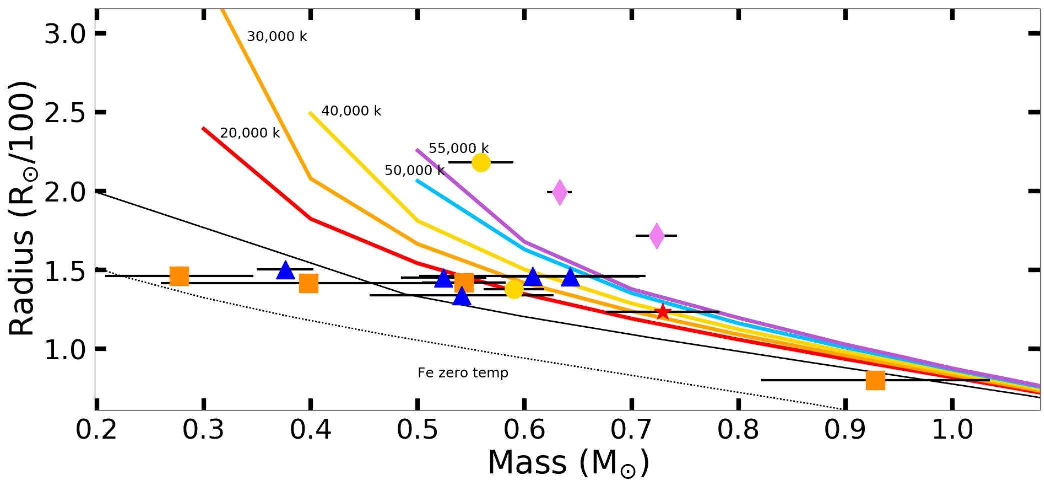

Figure 2.6: The effect of temperature on the mass-radius relation. The mass-radius results are colour coded according to the temperature of the white dwarf. (Red star) 18,000 - 25,000 K, (Orange square) 25000 - 35,000 K, (Yellow circle) 35,000-45,000 K ,(Blue triangle) 45,000-55,000 K, (Purple diamond) $>$ 55,000 K. Two theoretical zero temperature mass-radius relations are shown as black lines. They are for core compositions of Fe (bottom) and carbon (top) (Hamada & Salpeter, 1961). Above the zero temperature relations are C/O core, thick H-layer models for temperatures of 20,30,40,50 and 55,000 K as indicated on the figure (Fontaine, Brassard & Bergeron, 2001). The C/O core models are calculated for the temperatures in the middle of the ranges given for the data points and match the colour of the corresponding data points in the on-line version.

Table 2.3: Results of spectral fitting of the *HST* and *FUSE* spectra to determine the log g, $T_{\rm eff}$ and norm parameters. The norm column gives the scaling factor found from fitting the models which is related to the distance and radius of the WD via equation 2.1. These results are from fitting with a pure H non-LTE grid using the Tremblay broadening tables. *FUSE* spectra have upper case obs ID while *HST* spectra start with a lower case 'o'.

obs ID	Name	log g	$T_{\rm eff}$ (K)	Norm $(\frac{D^2}{R^2}) \times 10^{-21}$
	Sirius B			
obt801010	HST	8.62 ± 0.01	26102 ± 63	0.463 ± 0.002
obt801040	HST	8.61 ± 0.01	25807 ± 62	0.475 ± 0.002
obt801030	HST	8.59 ± 0.01	25885 ± 64	0.473 ± 0.002
obt801020	HST	8.57 ± 0.01	25894 ± 65	0.471 ± 0.002
Average	**Sirius B**	**8.60 ± 0.05**	**25922 ± 296**	**0.471 ± 0.013**
	HZ 43			
M1010501000	FUSE	7.921 ± 0.006	50631 ± 68	3.124e-3 ± 7e-06
P1042301000	FUSE	7.897 ± 0.004	50885 ± 47	3.015e-3 ± 5e-06
P1042302000	FUSE	7.939 ± 0.003	51110 ± 33	2.952e-3 ± 3e-06
Average	**HZ 43**	**7.92 ± 0.04**	**50875 ± 414**	**3.03e-3 ± 1.5e-4**
o69u070	HST	7.90 ± 0.03	51747 ± 411	3.04e-3 ± 2.5e-05
o69u080	HST	7.86 ± 0.04	50943 ± 387	3.06e-3 ± 2.5e-05
o57t020	HST	7.88 ± 0.05	50796 ± 608	3.06e-3 ± 4.0e-05
o57t010	HST	7.93 ± 0.04	51414 ± 528	3.03e-3 ± 3.3e-05
Average	**HZ 43**	**7.89 ± 0.07**	**51225 ± 950**	**3.05e-3 ± 2.8e-05**
	14 Aur Cb			
A05407070	FUSE	7.93 ± 0.02	42438 ± 95	1.45e-3 ± 6e-06
obt804050	HST	7.87 ± 0.10	45357 ± 943	1.38e-3 ± 3.4e-05
obt804060	HST	7.96 ± 0.11	46291 ± 1196	1.36e-3 ± 4.1e-05
Average	**14 Aur Cb**	**7.92 ± 0.06**	**45824 ± 660**	**1.37e-3 ± 1.7e-05**
	HD 2133 B			
B0550201000	FUSE	7.6 ± 0.1	28276 ± 70	6.36e-4 ± 1.5e-05

Continued on next page

Table 2.3 – *Continued from previous page*

obs ID	Name	log g	$T_{\rm eff}$ (K)	Norm $(\frac{D^2}{R^2}) \times 10^{-21}$
obt802010	HST	7.83 ± 0.07	29612 ± 266	6.01e-4 ± 1.3e-05
obt802020	HST	7.64 ± 0.08	29836 ± 299	5.92e-4 ± 1.4e-05
Average	**HD 2133 B**	**7.73 ± 0.13**	**29724 ± 158**	**5.97e-4 ± 6e-06**
	HR 1358 B			
obt808050	HST	8.14 ± 0.04	20922 ± 190	3.37e-3 ± 6.3e-05
obt808060	HST	8.10 ± 0.08	20657 ± 183	3.51e-3 ± 6.4e-05
Average	**HR 1358 B**	**8.12 ± 0.03**	**20790 ± 187**	**3.44e-3 ± 9.7e-05**
	HD 223816			
A05408090	FUSE	7.83 ± 0.01	73999 ± 267	6.49e-4 ± 3e-06
	RE 0357			
B05510010	FUSE	7.87 ± 0.03	33927 ± 66	8.84e-4 ± 9e-06
	RE 1024			
B05508010	FUSE	7.51 ± 0.02	37274 ± 37	1.09e-3 ± 3.5e-05
	REJ 1925			
A05411110	FUSE	7.80 ± 0.03	49037 ± 263	6.25e-4 ± 7e-06
	Feige 24			
P10405040	FUSE	7.64 ± 0.01	62835 ± 119	3.24e-3 ± 8e-06
	HD 15638			
A05402010	FUSE	7.66 ± 0.02	50110 ± 203	4.75e-4 ± 5e-06

Table 2.4: Mass and radius values calculated using the spectroscopic parameters listed in Table 2.3.

Name	obs ID	**HST** Radius (0.01 $R_\odot$)	Mass ($M_\odot$)	Distance (pc)
Sirius B	obt801010	0.796 ± 0.004	0.954 ± 0.029	2.639 ± 0.01
Sirius B	obt801020	0.804 ± 0.004	0.874 ± 0.026	2.639 ± 0.01
Sirius B	obt801030	0.805 ± 0.004	0.924 ± 0.028	2.639 ± 0.01
Sirius B	obt801040	0.807 ± 0.004	0.962 ± 0.028	2.639 ± 0.01
Average	HST	0.802 ± 0.011	0.927 ± 0.107	2.637 ± 0.011
HZ43	M1010501000	1.48 ± 0.007	0.665 ± 0.011	59.68 ± 0.262
HZ43	P1042301000	1.454 ± 0.006	0.608 ± 0.008	59.68 ± 0.262
HZ43	P1042302000	1.438 ± 0.006	0.656 ± 0.008	59.68 ± 0.262
Average	FUSE	1.457 ± 0.036	0.643 ± 0.065	59.68 ± 0.262
HZ43	o69u070	1.459 ± 0.009	0.614 ± 0.048	59.68 ± 0.262
HZ43	o69u080	1.464 ± 0.009	0.568 ± 0.048	59.68 ± 0.262
HZ43	o57t020	1.464 ± 0.011	0.59 ± 0.067	59.68 ± 0.262
HZ43	o57t010	1.458 ± 0.01	0.661 ± 0.066	59.68 ± 0.262
Average	HST	1.461 ± 0.009	0.607 ± 0.106	59.68 ± 0.262
14 Aur Cb	A05407070	1.378 ± 0.011	0.59 ± 0.028	81.656 ± 0.62
14 Aur Cb	obt804050	1.346 ± 0.0193	0.492 ± 0.126	81.656 ± 0.622
14 Aur Cb	obt804060	1.334 ± 0.023	0.595 ± 0.178	81.656 ± 0.622
Average	HST	1.34 ± 0.013	0.541 ± 0.086	81.656 ± 0.622
HD2133 B	B0550201000	1.464 ± 0.018	0.277 ± 0.069	130.876 ± 0.462
HD2133 B	obt802010	1.423 ± 0.016	0.495 ± 0.088	130.876 ± 0.462
HD2133 B	obt802020	1.413 ± 0.018	0.32 ± 0.068	130.876 ± 0.462
Average	HST	1.418 ± 0.009	0.398 ± 0.138	130.876 ± 0.462
HR1358 B	obt808050	1.223 ± 0.0123	0.748 ± 0.072	47.502 ± 0.173
HR1358 B	obt808060	1.248 ± 0.012	0.711 ± 0.137	47.502 ± 0.173
Average	HST	1.235 ± 0.018	0.729 ± 0.053	47.502 ± 0.173
RE 0357	B05510010	1.42 ± 0.014	0.543 ± 0.039	107.68 ± 0.876
HD 223816	A05408090	1.717 ± 0.009	0.723 ± 0.019	151.846 ± 0.689
RE 1024	B05508010	2.183 ± 0.043	0.559 ± 0.03	149.065 ± 1.782
REJ 1925	A05411110	1.452 ± 0.024	0.524 ± 0.04	130.907 ± 2.065
Feige 24	P10405040	1.993 ± 0.009	0.633 ± 0.012	78.935 ± 0.335
HD15638	A05402010	1.504 ± 0.042	0.376 ± 0.026	155.618 ± 4.303

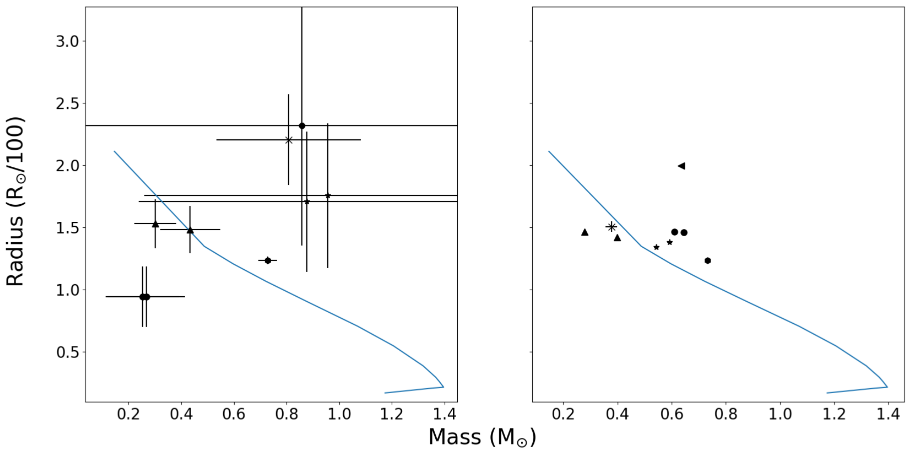

Figure 2.7: Comparison of results using parallax from *Hipparcos* (left panel) and *Gaia* DR2 (right panel). The blue line is the Hamada-Salpeter zero-temperature MRR for a C/O core WD. Error bars are calculated from the error in the parallax and do not include the error due to the spectroscopic fitting parameters. The DR2 errors are too small to be seen on this scale. These figures only include targets which had a parallax in the *Hipparcos* catalogue so not all of the targets in Fig.(2.6) are included.

2.6 Discussion

2.6.1 Sources of uncertainty

The currently available data is a vast improvement over the results that could be obtained using previously available parallaxes. However, there is clearly a great deal of uncertainty remaining. Here I investigate whether the main source of uncertainty is still the parallax and compare this error contribution to the error from the spectroscopic fitting parameters.

Parallax

As a comparison to show the effect of the improved parallax data, Fig. 2.7 shows the MRR calculated using the *Hipparcos* parallax (left panel) and the *Gaia* DR2 parallax (right panel). Only the zero temperature (Hamada & Salpeter, 1961) relation is plotted here for clarity. This plot only contains a subset of the WDs, which have parallaxes available in both catalogues. The error bars are calculated from the uncertainty in the parallax alone, and do not include the error from the spectroscopic fitting. It clearly shows that the *Gaia* parallaxes not only reduce the error bars to the point of being negligible, but also bring many of the targets into much closer agreement with the MRR. The distance measurements are no longer a major source of error.

Atmospheric parameters

For the majority of targets, where only one spectrum is available, the uncertainty in the norm and log g has been taken as the statistical error on the parameter found by the model fitting procedure. For the log g parameter this gives an uncertainty of on average 0.03 However, this error range is smaller than the spread in log g results found from fitting multiple spectra from the same target taken with the same instrument. In Fig. 2.8 and Fig. 2.9 the top and bottom panels show the spread in $T_{\rm eff}$ and log g from fitting multiple spectra of Sirius B and HZ 43. A similar test was carried out by Tremblay et al. (2017) for Wolf 485A (See their fig. 6). The spread in values for Wolf 485A found when using the same models and fitting technique is indicated by the black cross at the centre of each plot. We have set the axis of the plots have the same width to aid direct comparison. The optical spectra for Sirius B (top panel) give a smaller spread than Wolf 485A. The 4 Sirius B spectra have a log g range of 0.046 The spectra for Sirius B are exceptionally high S/N ($\sim$ 200) so it is possible that this spread in log g results represents a lower limit for the log g uncertainty using this method of spectral fitting.

It is clear that the spread in values for HZ 43 is the same as for Wolf 485 A in the optical. The far-UV on the other hand gives a much smaller spread. In (Fig. 2.9, lower panel) it is particularly noticeable that the uncertainty associated with the individual FUSE results (stars) is much smaller than the HST results (circles). It was noted (Barstow et al., 2003) that the Lyman lines gave smaller uncertainties in log g and $T_{\rm eff}$ compared to the Balmer line spectroscopy. The Balmer line spectra in Barstow et al. (2003) were ground based observations with S/N $\sim 50-100$ similar to the HST spectra used here. In Fig. 2.10 the mass and radius have been calculated for each individual spectrum for Sirius B and HZ 43 rather than taking the average. The top panel shows the spread in mass-radius results for Sirius B. The bottom panel compares the spread and uncertainty in the mass-radius values from the HZ 43 Balmer line (filled circles) and Lyman line (empty circles) spectra. The spread in mass values derived from these two targets is $\sim$0.1 $M_\odot$. This shows that when the spread in parameter values taken from multiple spectra is used as an estimate of the measurement uncertainty, the resulting error range in the mass-radius calculations is still too large to be able to distinguish between theoretical MRRs with different core compositions or H-layer thickness using the spectroscopic method.

Spectroscopic method precision and the MRR

To evaluate the contribution of each of the input parameters as a percentage of the total error, I have calculated the individual error contributions in Table 2.5.

The distance and normalisation contribute to both the radius and mass calculations via equations (2.1) and (2.2) so their contribution to the radius error and the mass error are listed separately. The error contribution of each parameter was calculated by propagating the statistical uncertainty from the χ^2 fitting through the mass-radius calculations. These are then converted to a percentage of the final error for ease of comparison. The discussion of the spread in values from several spectra compared to the uncertainty in individual spectra has shown that the spread in values is much larger than the statistical uncertainty. In order to compare these two measures of uncertainty, Table 2.5 includes an 'Average' row for each target. The error values in this row are based on the standard error in the mean for parameter values taken from several spectra of the same target. The 'Average' uncertainty gives a more realistic estimate of the uncertainty involved with these measurements. It is important to compare this with the errors quoted for targets where only a single spectrum is available as the errors are likely to be underestimated for most targets.

For the radius calculations, the error due to the distance derived from the parallax is now less than or equal to the uncertainty from the normalisation. All targets except HZ43 have a distance error contribution of $\sim$50 per cent or less to the error in the average radius. For most targets the spread in the normalisation values is similar to the error in individual measurements so the percentage error contribution remains the same for the average radius. A notable exception is Sirius which has a parallax error of only 0.4 per cent due to its close proximity to Earth, so in this case the spread in normalisation is the dominant source of error at 78 per cent of the total error.

For the mass calculations the log g parameter is the dominant source of uncertainty contributing between 63-96 per cent of the total error when calculated from the spread in the average log g. The error in the distances is now the smallest source of uncertainty, contributing no more than 6 per cent to the average mass error. This confirms that *Gaia* DR2 has reduced the distance errors to the point where they are no longer dominant, and supports the conclusion of Tremblay et al. (2017) that it is the atmospheric parameters which are now limiting the accuracy of the mass-radius measurements. For all targets in this sample, the results for radius measurements show greater consistency than the mass measurements regardless of whether Lyman or Balmer spectra are used.

Table 2.5: The per cent error contribution of each input parameter to the final error in the mass-radius calculations. The values in the main rows are calculated from the statistical error on each parameter from fitting individual spectra. The values in the 'Average' rows are based on the standard error in the mean parameter values found from fitting several spectra of the same target.

Name	dist err % (R)	norm err % (R)	Radius ($R_{\odot}$)	Mass ($M_{\odot}$)	dist err % (M)	norm err % (M)	g err % (M)
HZ 43	79	20	0.0148±0.000067	0.67±0.01	31	7	60
HZ 43	85	14	0.0145±0.000065	0.61±0.01	40	6	52
HZ 43	89	10	0.0144±0.000064	0.66±0.01	48	5	45
Average	15	84	0.0146±0.000364	0.64±0.06	5	30	63
HZ 43	51	48	0.0146±0.000088	0.61±0.05	7	6	86
HZ 43	52	47	0.0146±0.000087	0.57±0.05	6	5	87
HZ 43	40	59	0.0146±0.000115	0.59±0.07	4	7	87
HZ 43	44	55	0.0146±0.000101	0.66±0.07	5	6	87
Average	49	50	0.0146±0.000093	0.61±0.11	3	3	93
14 Aur Cb	38	61	0.0135±0.000193	0.49±0.13	3	6	89
14 Aur Cb	33	66	0.0133±0.000225	0.60±0.18	3	6	89
Average	55	44	0.0134±0.000131	0.54±0.09	6	4	88
HD 2133 B	25	74	0.0142±0.000157	0.49±0.09	2	8	88
HD 2133 B	22	77	0.0141±0.000179	0.32±0.07	2	8	89
Average	39	60	0.0142±0.000092	0.40±0.14	1	2	96
Sirius B	59	40	0.0080±0.000036	0.96±0.03	14	9	76
Sirius B	58	41	0.0080±0.000036	0.88±0.03	14	9	76
Sirius B	58	41	0.0080±0.000036	0.92±0.03	13	9	76
Sirius B	59	40	0.0081±0.000036	0.96±0.03	14	9	75
Average	21	78	0.0080±0.000112	0.93±0.10	4	15	79
HR 1358 B	28	71	0.0122±0.000123	0.75±0.07	4	12	82
HR 1358 B	28	71	0.0125±0.000123	0.71±0.14	2	6	90
Average	20	79	0.0124±0.000180	0.73±0.05	6	24	69

2.6.2 Testing the MRR

The combined results from both the Lyman and Balmer spectra support the validity of the MRR. In comparison to studies using less accurate parallaxes (e.g. Schmidt 1996), the scatter in the data and the errors on the data points are considerably reduced. Fig. 2.7 shows that all but one of the stars which had a *Hipparcos* parallax available previously have converged towards the MRR rather than staying in the same position but with smaller errors. Most of the targets cluster around the 0.6 $M_\odot$ range. This is expected due to the sharply peaked WD mass distribution at ~ 0.6 $M_\odot$. There is a lack of data at the high mass range except for Sirius B discussed in section 2.6.3. The mass of HD 2133 is uncertain as the *HST* results are within 2σ of the MRR but the *FUSE* result is not consistent at the $> 3\sigma$ level.

A detailed comparison of each white dwarf with a theoretical relation of the appropriate temperature reveals that only five out of eleven are within 2σ. This might indicate that the details of the MRR still need adjustment. However, it has been shown in section 2.6.1 that the uncertainty in individual spectra may be underestimated. Four out of the five which agree with the MRR have errorbars calculated from the spread in results from several spectra. Of the six outliers, five have errors based on the statistical uncertainty in a single spectrum. The errors were recalculated by assuming a log g uncertainty of 0.1 which was found to be the spread in log g from multiple spectra of HZ 43 in Fig. 2.9. With these more realistic errors, 45 per cent of the sample agree within 1σ and 91 per cent are within 2σ. Although still slightly lower percentages than would be expected if the MRR were valid, this does not raise serious doubts about the validity of the MRR, given that there are still some doubts over the exact mass-radius values for HD 2133 B. Analysing further data using the gravitational redshift method may help to better constrain the mass of HD 2133 B, as will be discussed in the next chapter. What the data does show, is that the uncertainties in most cases are now small enough to clearly identify WDs which follow the MRR, and also to distinguish stars which do not follow the MRR such as HD 15638.

For the 10 stars within 2σ of the MRR, 3 favour a thin H-layer model. 14 Aur Cb is within 2σ of the thin MRR and more than 3σ from the thick MRR for both the UV and optical results. HZ 43 and REJ 1925 are less certain as they are both within 1σ of the thin model but still agree with the thick model within 2σ. HD 2133 B is closer to the thin MRR but with relatively large uncertainty as previously discussed. Of the remaining 7 stars, Feige 24 and HD 223816 are the only ones which are clearly a better fit to the thick H-layer MRR and are $> 3\sigma$ from the thin MRR. The rest, including Sirius B, are within 2σ of both thick and thin H-layer models

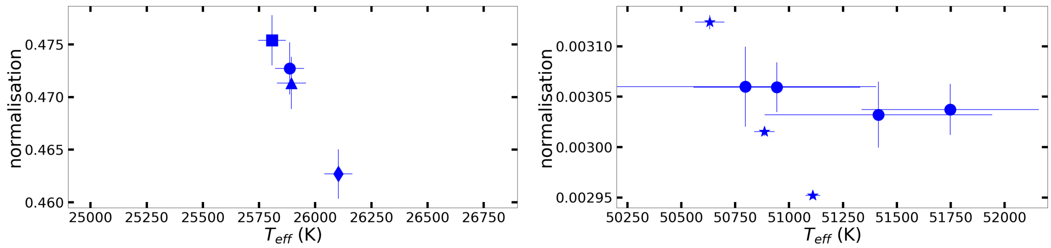

Figure 2.8: **Left panel:** The spread in normalisation from fitting 4 *HST* spectra of Sirius B. The results from spectrum obt801010 (diamond) gives a slightly higher temperature than the other 3 spectra. **Right panel:** The spread in normalisation from fitting 4 *HST* (Circles) and 3 *FUSE* spectra (Stars) of HZ 43. Results are consistent between the Lyman and Balmer spectra.

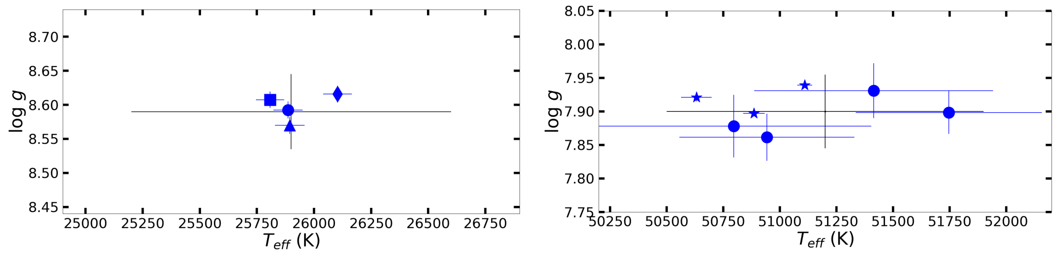

Figure 2.9: Scatter in log g and $T_{\rm eff}$ parameters measured from multiple spectra of the same star. For comparison, the black cross in both panels indicates the spread found for WD1327-083 (Wolf 485A) as shown in Fig. 6 of Tremblay el al. (2017). **Left:** Sirius B, best fit parameters for 4 *HST* Balmer line spectra. **Right:** HZ 43 B, *FUSE* Lyman line spectra (stars) and *HST* Balmer line spectra (circles).

and can not distinguish between them, although the dynamical mass of Sirius B (see section 2.6.3) clearly agrees with the thick H-layer MRR. This adds to the findings of previous studies by Provencal et al. (1998) and Romero et al. (2012) which have also found evidence for a range of H-layer thickness for DA white dwarfs.

The effect of temperature

According to the theoretical models, some spread in the mass-radius results is expected due to the different temperatures of the stars in the sample. It is expected that WDs of a given mass will have a larger radius if they have a higher temperature. The limited size of the sample means there are not enough stars in each temperature range to test the MRR across the full mass range. However, it may be possible to test for any general trends with temperature using the full sample.

Fig. 2.6 shows the result of plotting the MRR with markers colour coded according to 5 temperature bins. They are compared to theoretical MRR tracks for

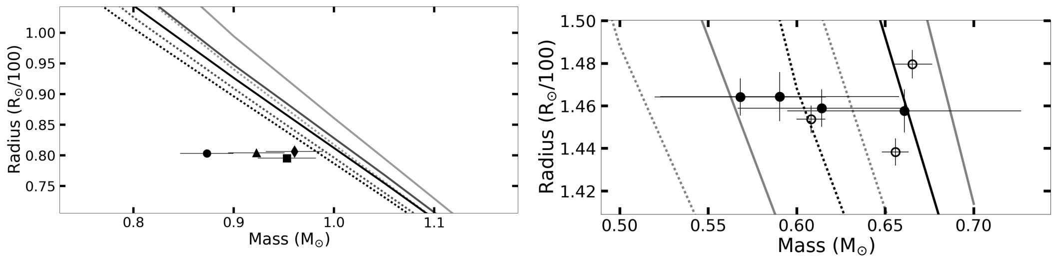

Figure 2.10: **Left:** The MRR results for each spectrum of Sirius B calculated individually. All results are from *HST* Balmer line spectra. **Right:** Results for each spectrum of HZ 43 including Lyman line (Empty circles) and Balmer line spectra (Filled circles). The $T_{\rm eff}$ measured for HZ 43 is 51,189 K. The MRR is plotted for temperatures of 25,51 and 58,000 K from left to right. The data points are clustered around the MRR for 51,000 K but are consistent with both thin (dashed line) and thick (solid) models.

a range of temperatures and thick hydrogen layers. The results match the expected trend with the lowest temperature stars slightly below the zero temperature relation and hotter stars increasingly further above the zero temperature relation. The results for Feige 24 and HD 223816 are the most inconsistent with the zero temperature MRR. These two stars are also the hottest in this sample with temperatures of 62,835 K and 73,400 K respectively.

The correlation between increasing temperature and radii larger than the zero temperature model indicates that temperature is indeed an important factor. Much better agreement is found when these targets are compared to the MRR appropriate for their temperature. Only three are consistent with the zero-temperature carbon core model compared to ten when temperature effects are included. Although the data matches the expected trend with increasing temperature, it appears that there is a wider spread in possible radii for a given mass than would be expected from the models, even when the thick H-layer models, which give larger radii, are used. For example, Feige 24 lies above the MRR while 14 Aur Cb and HZ 43 lie below the MRR for their temperature despite all 3 having almost the same mass. They would be expected to have a similar core composition given their similar mass. This may indicate that the influence of temperature on the radius is slightly underestimated in current models.

Comparison of Lyman and Balmer line results

A further issue to examine is the possibility of systematic differences between values derived from the Lyman or Balmer spectra. In the analysis by Barstow et al. (2003),

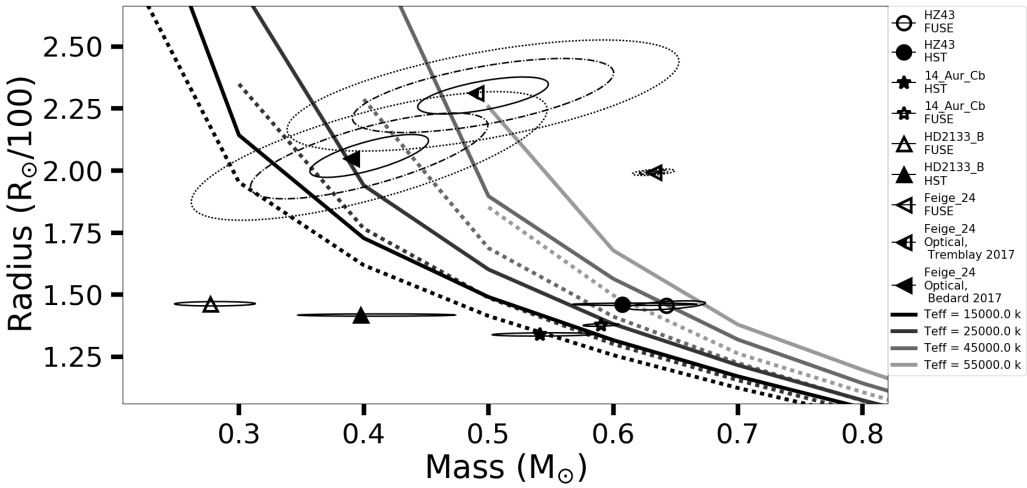

Figure 2.11: Comparison of mass-radius results for 4 WDs with both far-UV (hollow markers) and optical (solid) spectra. The error ellipses are 1σ for most targets except for Feige 24 where 1, 2 and 3σ ellipses are shown. The size of the ellipses for the Feige 24 optical data points are based on the log g and radius (with DR1 parallax) uncertainties quoted in (Tremblay et al., 2017; Bédard et al., 2017).

good consistency was found when comparing Lyman and Balmer results for WDs below 50,000 K using the H/He grid based on the Lemke broadening tables, but increasing discrepancies in temperature became apparent above this temperature. Here I repeat this test using the new (Tremblay & Bergeron, 2009) model grid. There are 4 WDs which can be used to compare the Lyman and Balmer results covering a T_{eff} range of 29,700 K to 62,835 K. HZ34, 14 Aur Cb and HD 2133 were observed by both *FUSE* and *HST*. For Feige 24 I include the Balmer line results obtained by Tremblay et al. (2017) and Bédard et al. (2017) to compare to the *FUSE* data.

Fig. 2.11 compares the mass-radius values obtained for each target. Each target is plotted twice with solid markers for optical data and hollow markers for far-UV. The uncertainty is represented as 1σ error ellipses which are at an angle to the axis due to the R^2 being included in the mass equation.

For the WDs below 50,000 K there is no significant difference in the results obtained from the same target when using both the Lyman and Balmer lines except in the case of HD 2133. HZ 43 and 14 Aur Cb both have Balmer and Lyman line results in agreement within the errors. HZ 43 shows that the results from Balmer and Lyman line fitting, even at 50,000 K, are entirely consistent (plotted as circles in Fig. 2.11). A more detailed plot showing the results for all the HZ 43 spectra individually is shown in (Fig. 2.8 and 2.9, lower panel). The 3 Lyman line spectra (stars) and 4 Balmer line spectra (circles) are in excellent agreement despite coming from different instruments and different wavelength ranges.

Feige 24 is above 50,000 K which was noted as the boundary where Lyman and Balmer determinations start to diverge (Barstow et al., 2003). Both the far-UV and the optical result of Tremblay et al. (2017) lie near the MRR for the temperature of 55,000 K as expected. However, there is no agreement between any of the 3 optical and UV data points at $> 3\sigma$.

At such high temperatures, radiative levitation can bring up trace amounts of heavy metals which could affect the shape of the hydrogen absorption lines. This would alter the log g and $T_{\rm eff}$ derived from their fitting. Feige 24 was one of the targets studied by Barstow et al. (2014) and found to contain heavy metals.

Barstow et al. (2014) using models including heavy metals but with the older Lemke broadening tables found a lower log g of 7.53. Combined with the new distance measurement, this gives a mass of 0.46 $M_\odot$ which is still not compatible with the optical data and no longer lies on the MRR at 55,000 K. More work is needed to understand the effects of heavy metals on the spectroscopic parameters and to solve the Lyman-Balmer problem (Preval et al., 2015) before WDs above 50,000 K can reliably constrain the MRR.

Details of individual systems

Several of the targets in this sample had very uncertain distance information available previously. 14 Aur Cb, HD 2133 B and HR 1358 B are also unresolved from the ground and these are the first optical spectra to be obtained. The following review highlights what the new data tell us about these WDs and the implications for the MRR.

HD 15638 The DR1 parallax was 3.8 $\pm$ 0.3 mas making this star a notable $> 3\sigma$ outlier in both mass and radius. The DR2 parallax is almost double the previous value at 6.4 $\pm$ 0.2 and has moved this data point from the top right of Fig. 2.5 to the bottom left. The *FUSE* spectrum was previously analysed by Kawka & Vennes (2010) who found log g and $T_{\rm eff}$ values in agreement with ours. Their mass estimate of 0.54 $\pm$ 0.01 $M_\odot$ was derived using the MRR because no distance measurement was available. With the new *Gaia* parallax the star is more than 2σ below the C/O core MRR for a temperature of 50,000 K.

14 Aur Cb The results for 14 Aur Cb show that it is close to the average WD mass. The Balmer and Lyman spectra give a mass of 0.54 ± 0.09 and 0.59 ± 0.03 $M_\odot$ respectively. Comparison with the MRR for a C/O WD shows that the data matches the thin H-layer models within 1σ and is not consistent with the thick H-layer model.

HR 1358 B was discovered by Boehm-Vitense (1993) and is a member of the Hyades cluster. Previous analysis (Burleigh et al., 1998) found a mass of 0.98 $M_\odot$ which was noted as probably too high because it gave a total age for the system which was younger than the cluster age. From the *HST* spectra I find a lower mass of 0.73 ± 0.05 $M_\odot$.

A lower mass also increases the estimated age of the system due to the longer main sequence lifetime of a lower mass WD progenitor. For a WD mass of 0.73 $M_\odot$ and $T_{\rm eff}$ 20,900 K, the total main sequence plus WD cooling age is approximately 240 Myrs. This is still some way short of the Hyades cluster age of 625 ± 50 Myr (Perryman et al., 1998). Even with the lower mass estimate of 0.73 $M_\odot$, HR 1358 B is still more massive than the majority of WDs, which makes this an important target for constraining the sparsely sampled high-mass end of the MRR.

HD 2133 B The mass-radius results for HD 2133 B are still somewhat uncertain. It was noted that the results for the *FUSE* spectrum of HD 2133 changed from 0.61 $M_\odot$ when fitting with models based on the older Lemke broadening tables, down to only 0.28 $M_\odot$ with the newer Tremblay based models. However the change for the *HST* spectra was much smaller, from 0.43 down to 0.4 $M_\odot$. The *FUSE* mass of 0.27 $M_\odot$ is lower than would be expected from single star evolution, which implies that the *HST* mass is more likely to be correct. It should be noted that 0.4 $M_\odot$ is the average of the 2 *HST* spectra and there is a range of 0.2 $M_\odot$ between them. With this large uncertainty, HD 2133 may be considered consistent with the C/O core MRR. Previous far-UV results (Burleigh et al., 1997) support the higher mass estimate (0.6 ± 0.05 $M_\odot$).

RE 0357 With the DR1 parallax this WD fell significantly below the MRR. DR2 increased the distance derived from the parallax from 98 to 108 pc and has brought this result into agreement with the MRR. This system includes a K2V main sequence star which is known to be very rapidly rotating despite being old enough to have spun down. The scenario suggested to explain this is that the MS star accreted material during the AGB phase of the current WD companion. This system was

Table 2.6: Comparison of mass and radius results for Sirius B from spectra analysed by various authors and the mass derived from astrometric measurements.

Method/model	Radius ($R_\odot$)	Mass ($M_\odot$)
Dynamical mass		
(Bond et al., 2017)	-	1.018 ± 0.011
Spectroscopic mass		
Tremblay model (this paper)	0.0080 ± 0.0001	0.927 ± 0.107
HST (2004 data, Barstow et al. 2005)	0.0080 ± 0.0004	0.841 ± 0.08
HST (2004 data, Bédard et al. 2017)	0.0079 ± 0.0002	0.940 ± 0.11
Ground based (Tremblay et al., 2017)	0.0080 ± 0.0001	0.872 ± 0.084

first noted as a UV excess source by Jeffries et al. (1996). The UV emission of a hidden WD was suggested as the true origin of the excess UV luminosity of the MS star. The required WD parameters in this scenario were calculated by Jeffries et al. (1996) as $M_\odot$ = 0.4-0.7 and $T_{\rm eff}$ 30,000-40,000 K. Our *FUSE* results fall within the predicted range with mass = 0.54 ± 0.04 $M_\odot$ and $T_{\rm eff}$ = 33,927 ± 66 K.

A higher mass of 0.79 $M_\odot$ was found from the EUV results (Burleigh et al., 1997) using the *Gaia* distance of 108 pc, although that requires a log g of 8.25 which is incompatible with the log g of 7.87 found here and by Barstow et al. (2014).

2.6.3 Sirius B

Sirius B represents an important benchmark for validating the results of the spectroscopic mass measurements because its mass can be measured by several independent methods. The mass is most accurately determined from the dynamical method which uses long term observations of the binary orbit to calculate the complete set of binary parameters including the mass of both Sirius A and B. Bond et al. (2017) recently published the results of analysis of 150 years of observations of the Sirius system, including almost 20 years of *HST* observations. From these it has been possible to measure the orbital motion of Sirius B over most of its 50 year orbit. The mass calculated in this way is the most reliable because it depends only on well-known laws of mechanics rather than spectral modelling. The disadvantage of this method is that it doesn't provide any information on the radius.

Fig. 2.12 shows the Bond et al. (2017) dynamical mass 1.018 ± 0.011 $M_\odot$ (red diamond). The dynamical method does not provide a measure of the radius so I use the radius measured from fitting the G430L spectra when plotting this data point. The radius measurement is dependent on the normalization from spectral fitting and the distance from the parallax which are two of the most accurately

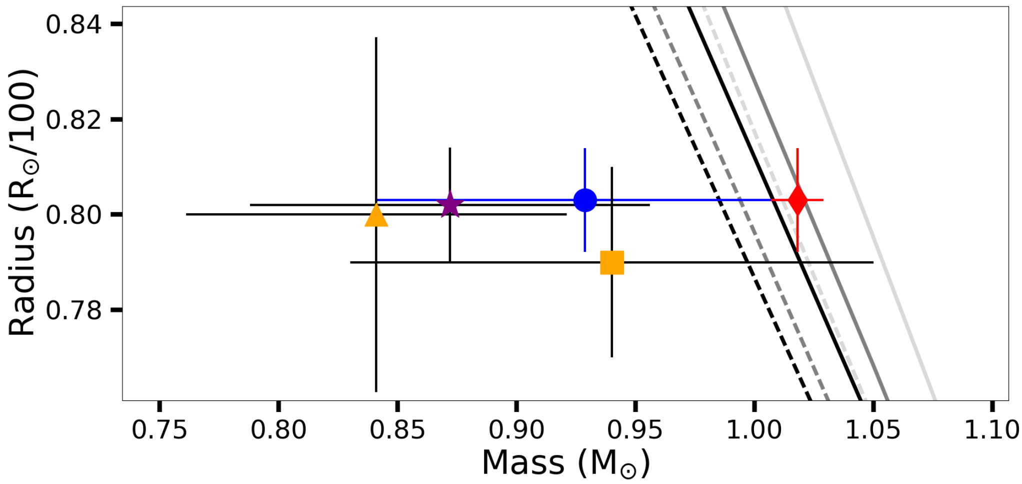

Figure 2.12: Sirius B. Comparison of mass measured using the dynamical (Red diamond) and spectroscopic method. The dynamical mass (Bond et al 2017) is consistent with the MRR for a C/O core WD at 25000 K. The theoretical tracks are from darkest to lightest 15,000, 25,000 and 45,000 K. Dashed lines are thin H envelope and solid lines are thick H envelope. The yellow markers are the 2005 *HST* Balmer line spectrum. The Bédard et al. (2017) result (yellow square) is consistent with the results from the new spectra (Blue circle) and give a larger mass than the Barstow et al. (2005) result using the same spectrum (yellow triangle). Also plotted is the Tremblay et al. (2017) measurement from a ground based spectrum (purple star).

measured parameters in the spectroscopic method. It should be noted that there is no parallax for Sirius in *Gaia* DR1 because the star is too bright to be handled by the normal processing. The parallax used here is the *Hipparcos* value 379.21 ± 1.58 mas from the new reduction of the catalogue (van Leeuwen, 2007). The uncertainty on this value is already very small and it is not expected to change much when measured by *Gaia*. The fitting of the 4 *HST* spectra for Sirius B shows very little variation in the radius and so it is possible to calculate an average radius value of comparable accuracy to the dynamical mass. Table 2.4 and 2.6 list the calculated mass and radius values with associated errors.

It was reported in Loyd et al. (2016) that the flux in their STIS spectra was often 10 per cent lower compared to COS spectra of the same target. This could be caused by loss of flux if the target was not correctly aligned in the slit or the slit used was too narrow and excluded some of the point spread function. Loss of flux would have the effect of decreasing the measured radius. However, there is no evidence to suggest that any of the spectra used here suffer from loss of flux. For targets where there were multiple spectra, or spectra from more than one satellite, the variation in flux is negligible. Similar measurements for HZ 43, 14 Aur Cb and HD 2133 B, using both *HST* and *FUSE* spectra gave flux/radius measurements that are in complete agreement from two independent satellites and calibration pipelines so it seems unlikely that there is any serious problem with the spectra.

Comparison with the theoretical MRR reveals that the dynamical mass with the spectroscopic radius is in excellent agreement with the MRR for a C/O core WD with a temperature of 25,900 K and a thick hydrogen layer. This is one of the few measurements where the uncertainty is small enough to be able to show clearly that the data is consistent with a thick H-layer model and not with the equivalent thin H-layer model of the same temperature. The mass measured using the spectroscopic method is 0.93 ± 0.1 $M_{\odot}$ which is almost 10 per cent less than the dynamical mass. The two measurements are consistent within 1σ, although this is due to the relatively large uncertainty in the spectroscopic mass resulting from the spread in log g values from the 4 spectra. By itself, this result does not indicate any serious discrepancy between the two methods. However, a comparison with the results found by other studies (Tremblay et al., 2017; Bédard et al., 2017) shows that the spectroscopic mass is consistently lower by at least 10 percent.

It is possible that improvements to the models may increase the mass estimate. Evidence for systematic differences being dependent on the models used rather than random error is found from comparing the results obtained by two different studies which both used the same *HST* spectrum of Sirius B taken in 2004.

This spectrum was fitted by Barstow et al. (2005) and has recently been re-analysed by Bédard et al. (2017). The models used are both pure hydrogen NLTE. The main difference between the studies is that Barstow et al. (2005) used models based on the Lemke (1997) broadening tables, whereas Bédard et al. (2017) used the Tremblay & Bergeron (2009) tables and included 3D corrections (Tremblay et al., 2013). It can be seen in Fig. 2.12 that the 2005 analysis resulted in a spectroscopic mass of only 0.841 ± 0.08 $M_{\odot}$ which is incompatible with the dynamical mass. The 2017 analysis has resulted in an increased mass of 0.94 ± 0.11 $M_{\odot}$ which is still lower than the dynamical mass, but is in close agreement with the results from the more recent *HST* spectra presented in this paper. It is interesting that the spectroscopic results from 2 different sets of *HST* spectra analysed independently, as well as the ground based spectrum (Tremblay et al., 2017), give results in complete agreement with each other, but consistently lower than the dynamical mass by 0.08 $M_{\odot}$. The results are also in disagreement with the mass derived from the gravitational red-shift method (Barstow et al., 2017) which is 1.1 ± 0.03 $M_{\odot}$.

It can be concluded that, although spectroscopic masses are formally consistent with the dynamic mass at the 1σ level, they are systematically about 10 per cent lower than the dynamic mass. It is more likely that the models, rather than the data or fitting method, are responsible for the systematic offset. The models provide a good fit to the data, but consistently give a gravity which is too low, causing the mass to be underestimated. It is hoped that these results from Sirius B might also help to indicate where improvements to the models need to be made.

One of the keys to resolving this issue may be the use of laboratory based tests to validate the theoretical models. Falcon et al. (2017) have developed laboratory tests which can probe higher plasma densities and have shown that even for the updated broadening tables (Tremblay & Bergeron, 2009) there are still differences between the theoretical and observed line profiles when the density of the plasma is increased to the levels found in WD atmospheres. Improved treatment of the Stark effects, which have been shown to cause asymmetry in the Balmer lines (Halenka et al., 2015) may be necessary to correctly fit the high quality spectra now available.

2.7 Conclusions

I have conducted a study with the main aims of testing the MRR using state of the art data and comparing results from optical and far-UV spectroscopy. The detailed analysis of the uncertainties involved with the Balmer/Lyman line fitting are a step towards improving upon the results that can currently be achieved. In particular, the validation of the Lyman line results will make it possible to extend spectroscopic studies to many SLSs which cannot be studied in the optical.

The use of parallax data from *Gaia* DR2 has substantially reduced the uncertainty in the mass determinations and also made it possible to obtain new results for some systems which previously had no parallax measurement available.

In common with studies using DR1 (Tremblay et al. 2017; Bédard et al. 2017), I find that most WDs in the sample are consistent with the MRR. 91 per cent of the WDs studied are within 2σ of the theoretical MRR appropriate for their temperature when realistic uncertainties are considered. HD 15638 is the main WD which does not agree within 2σ and is noted as having a significantly different parallax in DR1 compared to DR2. As shown by Bédard et al. (2017), the improvement in precision makes it possible to identify individual WDs which are inconsistent with the general trend of the MRR followed by most of the sample. Two stars in the sample are a better fit to thin H-layer models while others agree with thick H-layer models. This is similar to the findings of Provencal et al. (1998) and Romero et al. (2012) and shows that a range of evolutionary scenarios may have to be considered.

This analysis also confirms the finding of Barstow et al. (2003) that Lyman line fitting produces results consistent with the Balmer line fitting within 1σ. However, this does not apply to WDs above 50,000 K. More work is needed to understand the cause of the divergence in spectroscopic parameters obtained for WDs above 50,000 K, particularly the role that trace heavy metals may play in altering the shape of the hydrogen lines.

Despite using the best available space-based spectra, this study agrees with the conclusions of Tremblay et al. (2017) which showed that spectroscopic tests of the MRR are now limited by the accuracy of the spectroscopically derived parameters rather than the parallax. The spread in results obtained from multiple spectra of Sirius B and HZ 43 highlight the fact that even with the best optical spectra, the uncertainty still makes definitive tests of the MRR problematic. For HZ 43 which has 7 spectra available, there is a spread of 0.1 in log g which is similar to that found for Wolf 485A (Tremblay et al., 2017). As a consequence, there is an uncertainty in the mass derived from spectral fitting of at least 0.1 $M_{\odot}$ even for high S/N spectra. This is larger than the statistical uncertainty found from fitting single spectra by a factor of $\sim$2-3. The log g parameter is the main contributor. From the spread in HZ 43 results, it is estimated that the mass can currently only be measured to a precision of $\sim$ 14 per cent using Balmer line and 10 per cent using Lyman line data without using the MRR to derive the mass.

A preliminary attempt to search for observational evidence of the predicted temperature dependence of the WD radius in the data was not conclusive. The temperature clearly has some effect, with the hottest stars having the largest radii for a given mass. However, a much larger sample covering a wide temperature range for each mass bin will be required to provide a detailed test.

The radius obtained for Sirius B has produced a result in firm support of the MRR at the high mass end when combined with the dynamical mass (1.018 ± 0.011 $M_{\odot}$) of Bond et al. (2017). The spectroscopic mass is formally within 1σ of the dynamical mass and the MRR, although there is an apparent tendency for the mass to be underestimated, and the spread in spectroscopic results is much larger than the uncertainty in the dynamical mass.

In order to make progress with testing the MRR, the following issues will need to be addressed. Firstly, the causes of uncertainty in parameters derived from hydrogen line fitting will need to be identified and reduced. This includes the spread in results from different observations of the same target, which will most likely require improved spectra and refinements to the methods of fitting them. It also includes a more wide-ranging investigation into possible systematic offsets, especially for high mass white dwarfs and those above 50,000 K. Secondly, it will be necessary to extend the comparison of mass estimates obtained from different methods to include many more systems. This will show if the potential discrepancy noted for Sirius B is an isolated case, or a symptom of an underlying problem with spectroscopic mass determinations.

Chapter 3

Testing the mass-radius relation using the gravitational redshift method

3.1 Overview

In the previous chapter I tested the MRR using the spectroscopic method which can be applied relatively easily to many white dwarfs. Although it can be widely used, the accuracy of the spectroscopic method is limited by its dependence on model atmospheres which require many assumptions and complex input physics. In contrast, the gravitational redshift method is in principle much simpler as it relies only on measuring the wavelength of a line and comparing this to the rest wavelength.

The gravitational redshift method can potentially provide very precise tests of the MRR and it can also be used as a benchmark to check the results from the spectroscopic method. In this chapter I use the gravitational redshift method to test the mass-radius relationship. The data used consists of H-α line spectra of four white dwarfs, Sirius B, 14 Aur Cb, HD2133 B and HR1358 B, which cover most of the white dwarf mass range. I will also assess the effects of systematics and the level of accuracy that can currently be achieved with this method. Finally, the results will be compared to those from the spectroscopic method.

3.2 Introduction

Very few WDs have had a reliable and accurate mass measurement made using the gravitational redshift method even after nearly 100 years of effort. The history of gravitational redshift measurements of Sirius B illustrates some of the difficulties encountered.

The first attempt to measure the redshift of a white dwarf (Sirius B) was made by Adams (1925) who obtained a gravitational redshift velocity of 23 km s^{-1}. This measurement matched the theoretical prediction by Arthur Eddington of 28.5 km s^{-1} (Holberg, 2010) and was considered a successful result for the 3rd test of general relativity. It was only many decades later that it was realised how much the scattered light from the much brighter companion Sirius A had contaminated the spectrum, causing the measured redshift to be 4 times smaller than modern predictions ($\sim$ 80 km s^{-1}).

Greenstein et al. (1971) found a much larger redshift velocity of 89 $\pm$ 16 km s^{-1} in agreement with the corrected theoretical prediction of 80 km s^{-1} albeit with an error range of 16 km s^{-1} due to the difficulties of measuring the line cores on photometric plates with the methods available at the time.

The problems of scattered light from Sirius A can best be avoided by using space-based observations. An optical spectrum of Sirius B taken in space with CCD detectors was first obtained by HST in 2004 (Cycle 12 , PI Barstow), and resulted in a redshift with a greatly improved accuracy of 80.42 $\pm$ 4.83 km s^{-1} (Barstow et al., 2005). This redshift, when combined with the measured radius of 0.008 $R_{\odot}$ led to a mass of 1.02 $\pm$ 0.02 $M_{\odot}$ which is in agreement with the astrometric mass and the theoretical mass-radius relation (MRR) for a C/O core WD at 25,000 K. However, the spectroscopic mass (0.841 + 0.080/0.026 $M_{\odot}$) was significantly lower than the mass obtained from the gravitational redshift. The spectroscopic mass was also in disagreement with the mass determined from the binary orbit 1.053 $\pm$ 0.028 $M_{\odot}$ (Gatewood & Gatewood, 1978) which has recently been confirmed by Bond et al. (2017). This difference in the Barstow et al. (2005) results could only be partially resolved by taking the slightly higher radius (8.33 $R_{\odot}$) obtained from the flux from the G750 grating. This brought the spectroscopic mass into agreement with the MRR, but gave an increased gravitational mass of 1.050 $\pm$ 0.063 $M_{\odot}$ which was only marginally consistent with the theoretical mass-radius relation.

The dynamical method of determining the mass from a binary orbit is expected to be the most reliable because it is based on well understood laws of mechanics and is not dependent on complex models. The fact that the 3 methods do not agree when applied to Sirius B shows that much work still needs to be done to fully understand and improve the spectroscopic and gravitational redshift methods.

This problem is not just limited to Sirius B. Various studies (e.g. Falcon et al. 2012, Halenka et al. 2015) have noted that the gravitational redshift method gives systematically higher mass measurements than the astromentric or spectroscopic method. One possible cause of the overestimated mass is that part of of the observed shift is due to another process, such as the pressure (Stark) shift (section 1.4), but has been erroneously attributed to the gravitational redshift.

In this study, the line used to measure the gravitational redshift is the H-α line which has been shown to be the least affected by the pressure shift (Halenka et al., 2015). The pressure shift for H-α is predicted to be in the order of $\sim$2 km s^{-1} which is small compared to the $\sim$80 km s^{-1} gravitational redshift expected for Sirius B. However, the precision required to differentiate between the mass-radius relation for a thin or thick H-layer in the 1 $M_{\odot}$ range is only a few km s^{-1} so this effect may be important.

This study seeks to build on the results obtained in Barstow et al. (2005) for Sirius B and expand the analysis to include white dwarfs covering a wide mass range. These white dwarfs are all in Sirius-Like Systems. The bright main sequence companions currently prevent the WD from being resolved from the ground. These systems were suspected of having hidden white dwarf components because they exhibit much brighter UV emission than normal main sequence stars. They were resolved with HST (Barstow et al., 2001), revealing the positions of the white dwarfs. This enabled a follow-up program (12606, PI Barstow) to obtain spectra which will be used in this analysis.

3.3 Data

The data consists of G750M spectra covering a wavelength range of 5450-10140 Å which includes the H-α line at 6564 Å . For Sirius B there are 4 spectra taken with the 'wide' 52 x 2 arcsecond slit and another 4 with the 'narrow' 52 x 0.05 slit. The main reason for using the narrow slit is to exclude any stray light from Sirius A. The telescope was oriented so that the slit would be perpendicular to a line joining Sirius A and B, and so avoid capturing Sirius A in the slit.

The full list of exposures is given in Table 3.1 and examples of the spectra are shown in Fig. 3.1 to 3.4. The left section of the spectrum is the Balmer lines up to β taken with the G430L grating. This was used to obtain the radius in Chapter 2, which will be used here when calculating the mass. The right hand section shows

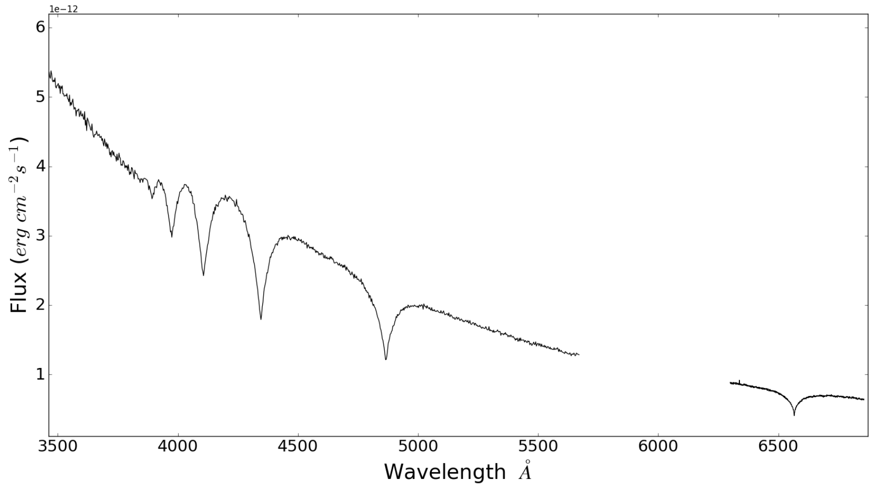

Figure 3.1: Sirius B HST spectrum. (2013)

the H-α line from the G750M grating which is used in this chapter to measure the gravitational redshift. The other lines are not reliable for measuring the shift as they have lower wavelength resolution and are more strongly affected by the pressure shift (See section 1.4).

3.4 Method

3.4.1 Overview

The basic premise of this method is to measure the wavelength of the H-α line and compare it to a rest wavelength to calculate how much it has been shifted. This wavelength shift can be converted to a velocity using the Doppler shift equation 3.1.

$$\frac{\Delta\lambda}{\lambda} = \frac{v_{gr}}{c} \tag{3.1}$$

The measured gravitational redshift is therefore referred to as a velocity (v_{gr}) in km s^{-1}.

From the measured gravitational redshift, the mass of the white dwarf is calculated using equation 3.2 where mass (M) and radius (R) are both in solar units.

$$v_{gr} = 0.636\frac{M}{R} \tag{3.2}$$

Table 3.1: HST spectra taken in 2012/13 as part of program 12606 in cycle 19 (PI Barstow).

Grating	λ Range (Å)	Resolution (Å)	Slit (arc sec)	File ID	Exposure Time (s)
Sirius B					
G430L	2900-5700	5.5	52x2	obt801010	3.5
	-	-	-	obt801020	3.5
	-	-	-	obt801030	3.5
	-	-	-	obt801040	3.5
G750M	5450-10140	1.11	52x2	obt801050	30.0
	-	-	-	obt801060	30.0
	-	-	-	obt801070	30.0
	-	-	-	obt801080	30.0
G750M	5450-10140	1.11	52x0.05	obt801090	100.0
	-	-	-	obt8010a0	100.0
	-	-	-	obt8010b0	100.0
	-	-	-	obt8010c0	100.0
HD2133 B					
G430L	2900-5700	5.5	52x0.2	obt802010	110
	-	-	52x0.2	obt802020	110
G750M	5450-10140	1.11	52x0.2	obt802030	963
	-	-	52x0.2	obt802040	963
14 Aur Cb					
G430L	2900-5700	5.5	52x0.5	obt804050	40
	-	-	52x0.5	obt804060	40
G750M	5450-10140	1.11	52x0.5	obt804030	200
	-	-	52x0.5	obt804040	200
G750M	5450-10140	1.11	52x0.05	obt804010	390
	-	-	52x0.05	obt804020	390
HR1358 B					
G430L	2900-5700	5.5	52x0.2	obt808050	40
	-	-	52x0.2	obt808060	40
G750M	5450-10140	1.11	52x0.2	obt808030	200
	-	-	52x0.2	obt808040	200
G750M	5450-10140	1.11	52x0.05	obt808010	437
	-	-	52x0.05	obt808020	437

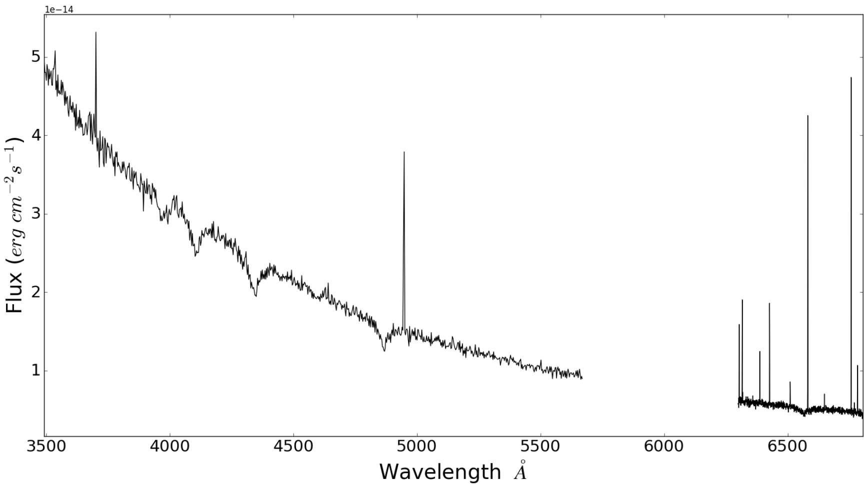

Figure 3.2: 14 Aur Cb HST spectrum. (2013)

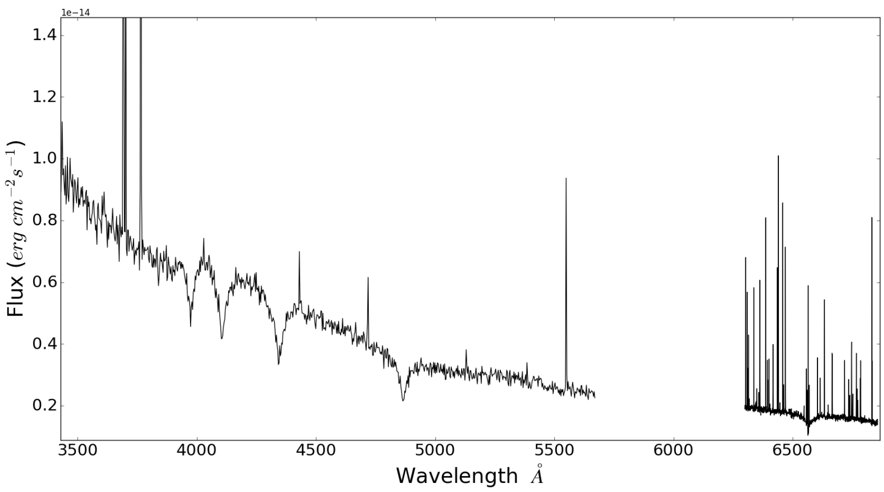

Figure 3.3: HD2133 B HST spectrum. (2013)

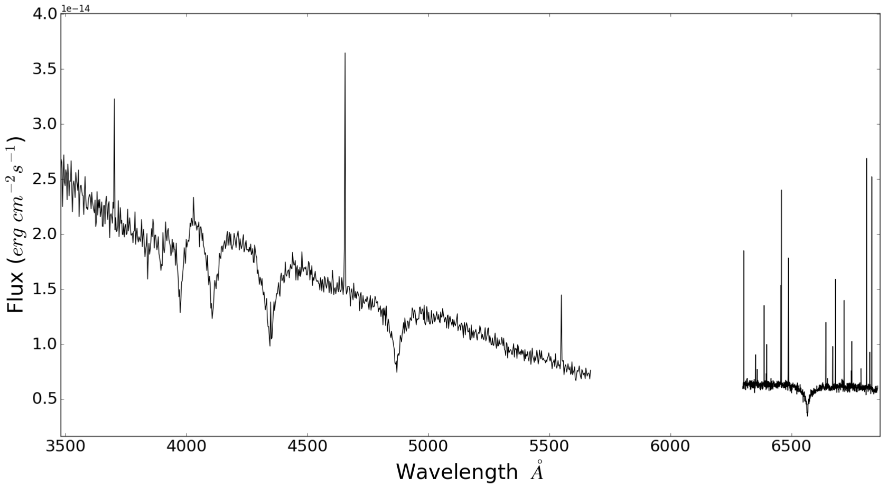

Figure 3.4: HR1358 B HST spectrum. (2013)

3.4.2 Fitting procedure

The H-α line in spectra of WDs is broadened due to the high pressure of the atmosphere in the region where the line is formed. The lack of a sharply-defined line position requires that the wavelength of the line centre be measured by fitting a model. The wavelength range included in the fitting can be narrow to include only the core of the line, or it can be wide to include more of the wings. In the past, lower resolution spectra were used which made it necessary to include the line wings as the core was not resolved. Lab tests on high density plasma (Falcon et al. 2015, Halenka et al. 2015) have shown that the wings can be slightly asymmetrical due to Stark effects which could systematically increase the measured shift of the spectrum leading to an overestimate of the gravitational redshift.

Following the procedure adopted by Barstow et al. (2005), the fitting is repeated for each H-α line four times including a different amount of the wings each time. This is done by selecting four wavelength ranges with a width of 8 to 176 Å centred on the apparent core of the line by visual inspection. This method makes it possible to assess the consistency of the fitting and to detect any shifts which might be introduced by including more of the wings.

Fig. 3.5 shows an example of fitting the H-α line for Sirius B. The analysis of the STIS spectra involves fitting models to the spectra using the standard χ^2 minimisation process in XSPEC. The models used are the same as in Chapter 2 generated using TLUSTY and SYSNSPEC (Hubeny & Lanz, 2017). These models are similar to the ones used in the Barstow et al. (2005) analysis of Sirius B except for using the updated broadening tables of Tremblay & Bergeron (2009) with additional updates from Tremblay 2015 (private communication). When fitting, the $T_{\rm eff}$ and log g parameters were kept frozen at the values found from the G430L fitting for each target. This leaves only the z parameter free to vary, which provides a measure of the wavelength shift of the spectrum.

It can be seen in Fig. 3.5 and 3.6 that several of the spectra are affected by cosmic ray hits. Panel A of Fig. 3.6 shows the original spectrum with noise between 6555 to 6560 Å. Regions of the spectrum affected in this way were removed prior to fitting as shown in Fig. 3.6 panel B to make it possible to achieve a reasonable fit to the remaining data. The effect of removing sections of the spectrum is that the resulting fit is less certain and the results must be treated with caution. In subsequent analysis steps both spectra obt804020 and obt802030 were identified as giving highly uncertain wavelength measurements.

3.4.3 Corrections to the measured velocity

The observed wavelength shift of the lines in the white dwarf spectrum is the sum of the gravitational redshift and the Doppler shift caused by the relative radial motion of the stars with respect to the observer. This and other causes of additional line shift must be removed to reveal the true magnitude of the gravitational shift.

Rest wavelength air to vacuum correction

The z parameter from fitting the model to the data in XSPEC is the shift relative to the rest wavelength as defined by the TLUSTY model grid. The corresponding shift in the wavelength can be calculated using equation3.3.

z is the redshift factor as defined by the shift in the measured wavelength. It must be clearly distinguished from the *gravitational* redshift which is calculated only after corrections have been applied for the relative motions between source and observer.

$$z = \frac{\Delta\lambda}{\lambda} = \frac{v_{obs}}{c} \tag{3.3}$$

Here, v_{obs} is the velocity measured from the shift in the H-α wavelength before any corrections are applied, so it is not attributed solely to gravitational redshift.

From equation 3.3, z can be converted back into a wavelength if the model 'rest' wavelength is known. The rest wavelength of H-α in air is 6562.795 Å according

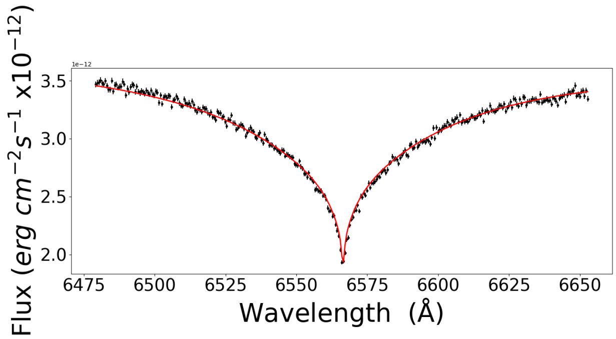

(a) Sirius B, wide slit

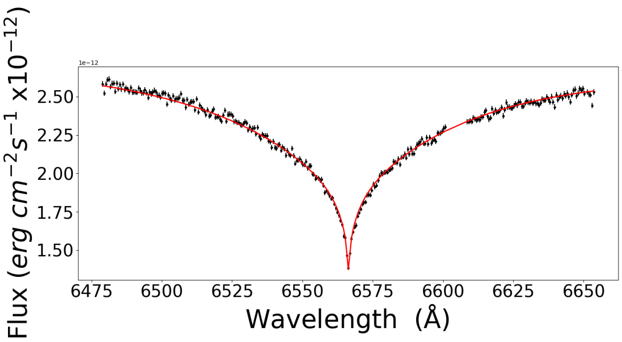

(b) Sirius B, narrow slit

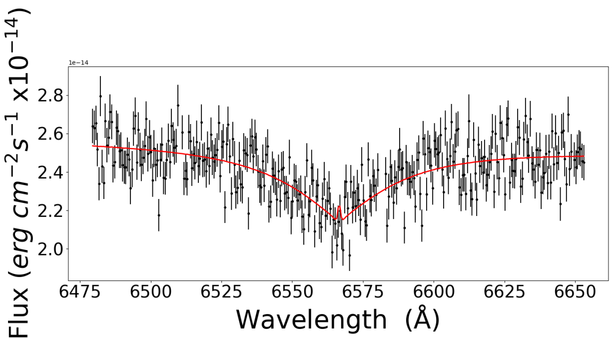

(c) 14 Aur Cb, wide slit

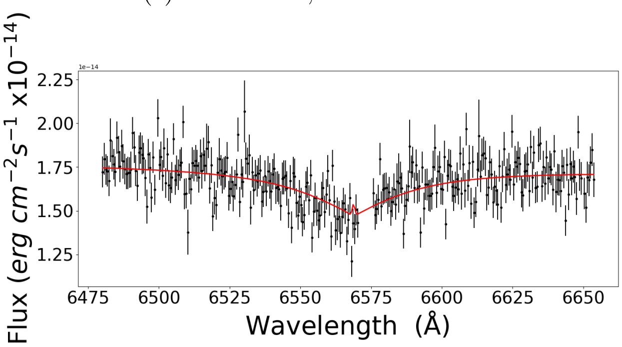

(d) 14 Aur Cb, narrow slit

Figure 3.5: Examples of XSPEC fitting of the H-α line for Sirius B and 14 Aur Cb. The best fit model is the solid red line.

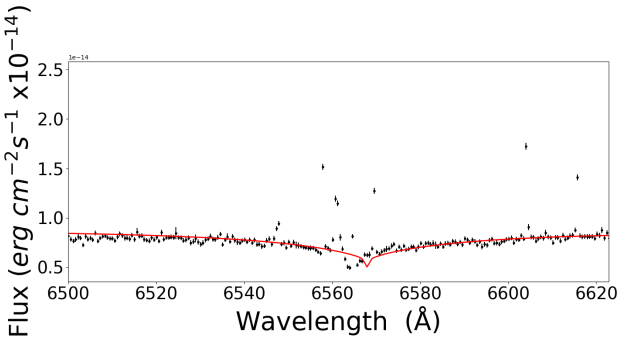

(a) HD 2133 B, obt802030, with spike included

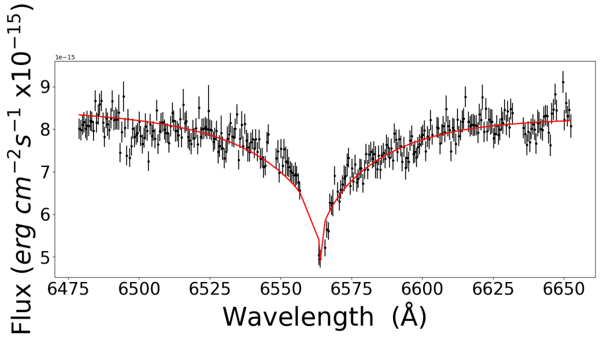

(b) HD 2133 B, obt802030, spike removed between 6550-6560 Å .

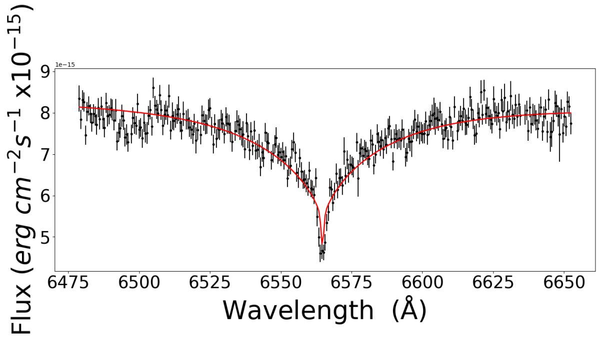

(c) HD 2133 B, obt802040

Figure 3.6: The effect of the obt802030 spectrum at 6560 Å is shown in the top panel. The middle panel shows the same spectrum after the affected wavelength region was excluded. The bottom panel is the obt802040 spectrum for HD 2133 B which is not affected by any problems.

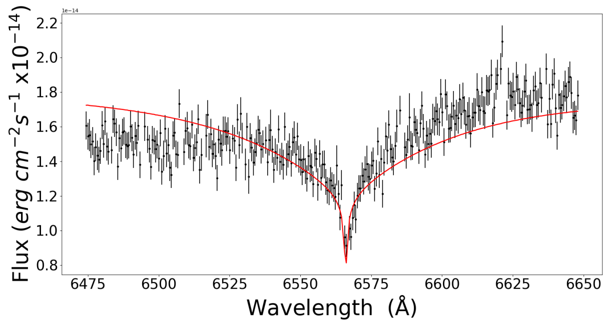

(a) HR 1358 B, obt808010, narrow slit

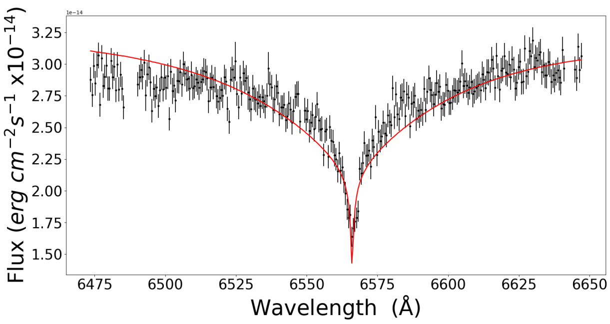

(b) HR 1358 B, obt808030, wide slit

Figure 3.7: Fitting of the HR 1358 B spectra. The wide slit spectra (lower panel) have a much deeper H-α line and the fitting results are more reliable compared to the narrow slit spectra.

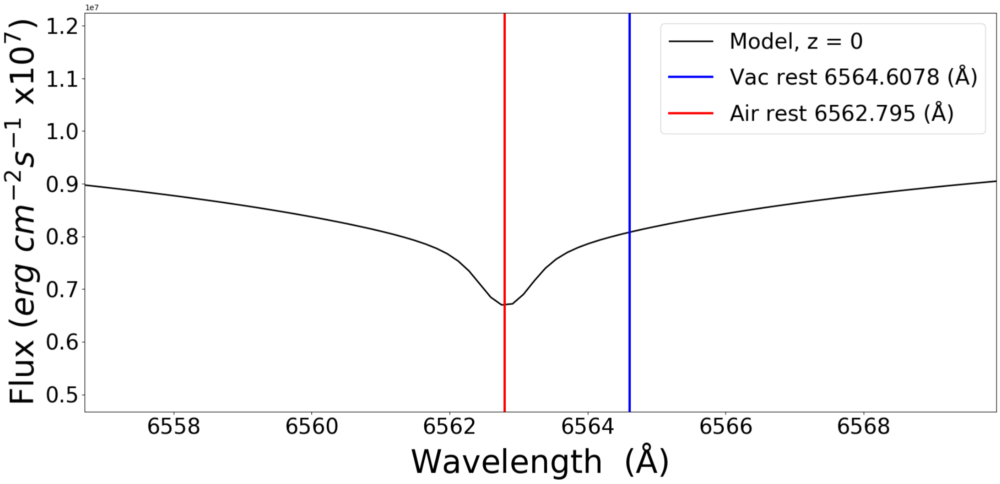

Figure 3.8: Model with z shift parameter set to zero to show the rest wavelength of H-α according to the model. It corresponds to the air rest 6562.795 Å (red line). The longer vacuum rest wavelength is 6564.6078 Å(blue line).

to the NIST ADS database (Kramida et al., 2018). Fig. 3.8 shows that this matches the H-α wavelength of the model when no shift is applied.

Barstow et al. (2005) pointed out that *HST* spectra are measured in a vacuum. The rest wavelength of H-α is slightly longer in a vacuum. 6564.6078 Å(vac). Measuring the shift in the H-α line relative to the air rest wavelength makes the shift appear larger than it really is and adds 82.8 km s^{-1} in terms of velocity. This was corrected for after the z shift had been converted to a velocity by subtracting away the velocity equivalent to the difference in rest wavelength between air and vacuum.

HST orbital motion correction

A barycentric correction is applied to adjust the spectra to the wavelength as it would appear if observed at the centre of the solar system to remove the effect of the orbital velocity of the Earth. This correction is applied as part of the pipeline processing automatically.

A further correction is required for the orbital motion of *HST* around the Earth. The correction for *HST* orbital motion is different for each spectrum depending on which point in the orbit the exposure was taken. Fig. 3.11 to 3.14 show the *HST* velocity relative to the target for each exposure. This correction can alter the final velocity by up to $\pm$ 7.5 km s^{-1}. The most relevant data-points for this analysis are the red triangles which mark the narrow (52x0.05) slit observations and the green stars for the wider slits. Values are listed in Table 3.3 (column 3). These velocities were calculated using a PYTHON script provided by STScI helpdesk which reads the time and spacecraft orientation from the spectral file and calculates the appropriate source-*HST* velocity. The corresponding shift in the wavelength was calculated using equation (3.1) and a correction applied directly to the spectral files before model fitting.

Radial velocity of the binary and the white dwarf

The shift in wavelength due to the gravity of the star is exactly equivalent to what would be observed if the star were moving away from the observer causing a Doppler shift. For this reason, the gravitational redshift is often given as a value in km/s^{-1} although it is not due to any movement of the source.

In order to deconvolve the redshift and space velocity from the observed velocity, it is necessary to have an independent measurement of the white dwarfs space motion. One method is to take a large sample of white dwarfs and take the average velocity of the sample. The assumption is that the velocities are random and will cancel out when the average is taken (Falcon et al., 2010). Any remaining velocity is therefore attributed to the gravitational redshift which is always a positive velocity. The drawback of this method is that it only gives the average redshift for the entire sample rather than for individual stars.

Measurements of the gravitational redshift effect can only be carried out for an individual WD if it is in a binary system. Repeated radial velocity measurements of the MS star show that it ocillates around a velocity which is the constant velocity of the binary centre of mass with respect to the observer (γ velocity).

Fig.3.9 shows radial velocity measurements of Sirius A which have been extrapolated to the date of the 2013 observations in Fig.3.15. The offset in the point where the velocity curves intersect is indicated by the vertical line at -7.69 km s^{-1} which is the constant velocity of the binary.

In addition to this, the orbital motion of the white dwarf itself creates an additional velocity component which varies with time (K). The final velocity of the white dwarf is the sum of the γ and K velocities.

$$\gamma_{\mathrm{WD}} = \gamma_{\mathrm{binary}} + K_{\mathrm{WD}} \tag{3.4}$$

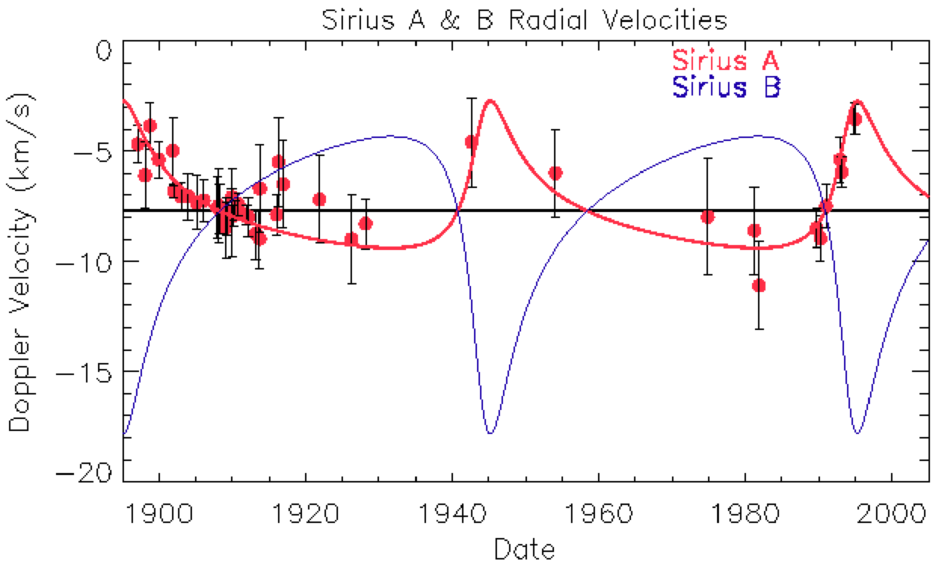

Figure 3.9: Radial velocity measurements of Sirius A. Figure provided by Jay Holberg.

The gravitational red-shift of the MS star

When measuring the RV of the main sequence star, it is also necessary to take into account the fact that it too has a gravitational red-shift which affects the RV measurement. The gravitational red-shift of the main sequence star is estimated from its mass and radius based on its observed spectral type.

$$v_{gr,MS} = 0.636 \frac{M_{MS}}{R_{MS}} \tag{3.5}$$

This correction is applied to the value of the white dwarf space velocity to correct for the redshift of the main sequence star. γ_{WD} must then be subtracted from v_{obs} to leave v_{gr}.

$$\gamma_{WD} = \gamma_{binary} + K_{WD} + v_{gr,MS} \tag{3.6}$$

Correction for instrumental slit position

When using the long slit in the STIS instrument, the target is dithered along the slit so that each spectrum is recorded by a different section of the CCD to minimise the impact of hot pixels. The slits are not perfectly aligned with the axis of the CCD but have a small offset angle (See table 11.2 , STIS Instrument handbook, Cycle 25). For the 52″ slit used here, the offset from the spacecraft orientation vector (U) is 45.35° which means the slit has an offset of 0.35° with respect to the dispersion axis of the CCD (See Fig. 4.3). The dithering of the target along the slit causes a slight change in the zero point of the spectrum which results in a shift of the measured wavelength of the spectral features.

The size of this slit offset is calculated as follows. The offset of the target along the slit (in arcsec) is given by the POSTARG2 key word in the FITS file header e.g. 0.609 for the obt801070 spectrum. For the G750M spectra with the 52x 0.05 slit the pixel scale is 0.05 arcsec/pix. So an offset along the slit of 0.609 arcsec is 0.609/0.05 = 12.19 pixels. This translates in to a shift along the dispersion direction of $12.19 \times 0.35 \times \frac{\pi}{180} = 0.075$ pixel In the dispersion direction, each pixel corresponds 0.56 Åso this slit offset results in a wavelength offset of $0.56 \times 0.075 = 0.042$ Å.

Table 3.3 shows the correction due to the slit position for each individual spectrum in terms of velocity. Across the 4 G750M spectra, the slit offset causes a variation in the measured velocity of up to ± 1.9 $\mathrm{km\,s^{-1}}$

3.4.4 Applying corrections to the measured velocity

The corrections described above are subtracted from the observed velocity according to formula (3.7) where v_{obs} is the velocity as it measured from the shift in the spectrum and v_{gr} is the velocity attributed only to the gravitational redshift. s is the offset caused by the slit tilt, γ is the radial velocity of the binary centre of mass and HST_{orbit} is the orbital velocity of the telescope.

$$v_{gr} = v_{obs} - \gamma - K_{\rm WD} - v_{gr,\rm MS} - s - HST_{orbit} \tag{3.7}$$

Calculating mass from V_{gr}

Once all the extra causes of wavelength shift have been corrected for, the final velocity is attributed to the gravitational redshift and is a direct consequence of the mass of the white dwarf. The velocity is then combined with the radius measured in chapter 2 to calculate the mass using equation 3.2 which correlates mass, radius and gravitational redshift.

3.5 Results

3.5.1 Check for spectral purity

The spectra were checked for contamination from the MS companion stars by inspecting the 2-D spectral images as shown in Fig.3.10. The plot on the right of each 2-D image is a vertical slice taken through the 2-D image which shows the flux on the y axis against the pixel number in the spatial direction (i.e. y axis from the 2-D plot). The slices show a sharp peak corresponding to the white dwarf spectrum and a very low flux level everywhere else. There is no evidence of scattered light affecting the spectra except for HR1358 B. After applying the same background subtraction as was used for the G430 spectra in chapter 2 it was found that this had no measurable effect on the wavelength of the line. Only the overall flux level was reduced.

3.5.2 Correction for radial velocity of the white dwarf

The Doppler shift affecting the spectrum due to the radial velocity of the binary and the white dwarf orbital velocity were calculated using the available information from observations of the main sequence star.

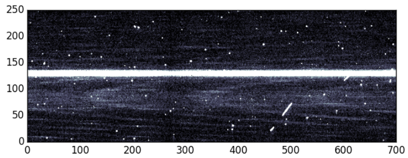

(a) Sirius B, narrow slit 52 x 0.05 slit.

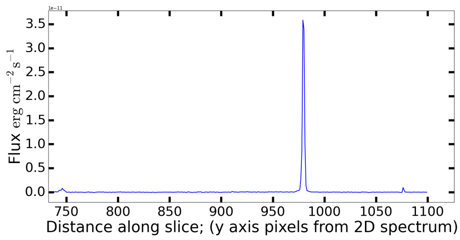

(b) Sirius B, narrow 52 x 0.05 slit vertical slice.

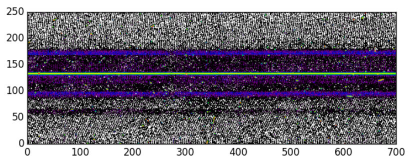

(c) 14 Aur Cb, wide slit 2D spectrum.

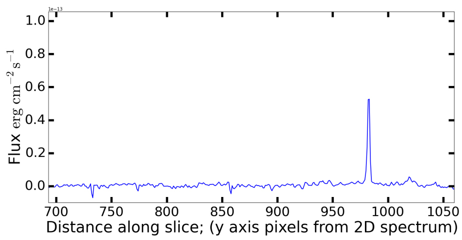

(d) 14 Aur Cb, wide slit spectrum vertical slice.

Figure 3.10: Examples of the 2-D spectra of Sirius B and 14 Aur Cb showing the bright line for the WD spectrum. The images are histogram equalised to show up any background clearly. Faint lines either side of the main spectrum are the signal from the diffraction spikes of the main sequence star. The right hand panels show the flux for a 1 pixel wide vertical slice through the 2-D spectrum.

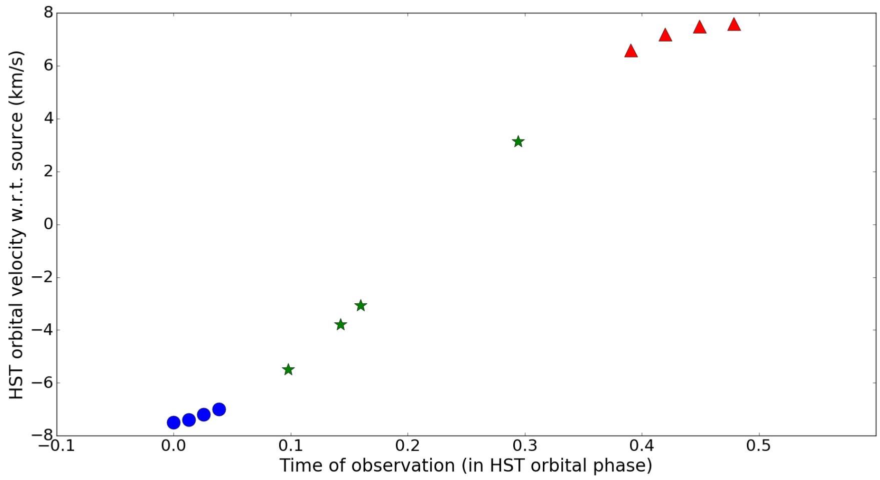

Figure 3.11: Sirius B: HST orbital velocity during each exposure. G430L 52x2 (Blue circles), G750M 52x2 (Green stars), G750M 52x0.05 (Red triangles)

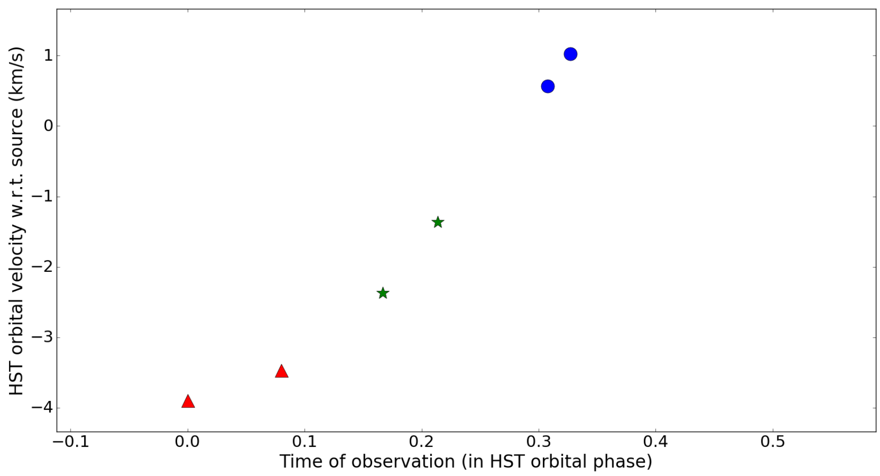

Figure 3.12: 14 Aur Cb: HST orbital velocity during each exposure. G430L 52x0.5 (Blue circles), G750M 52x0.5 (Green stars), G750M 52x0.05 (Red triangles)

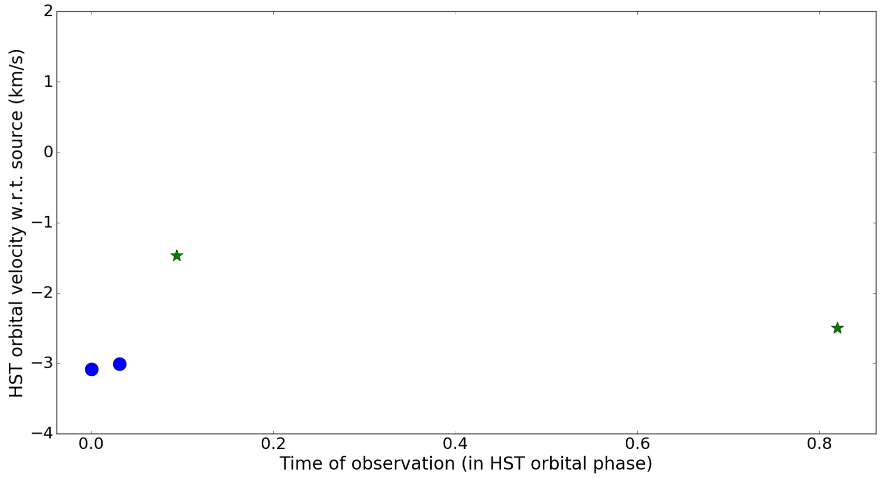

Figure 3.13: HD2133 B: HST orbital velocity during each exposure. G430L 52x0.2 (Blue circles), G750M 52x.02 (Green stars)

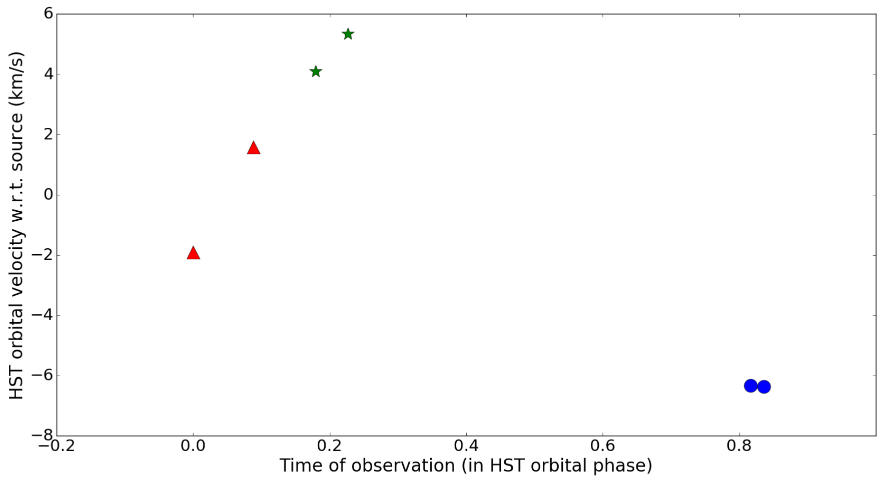

Figure 3.14: HR1358 B: HST orbital velocity during each exposure. G430L 52x0.2 (Blue circles), G750M 52x0.2 (Green stars), G750M 52x0.05 (Red triangles)

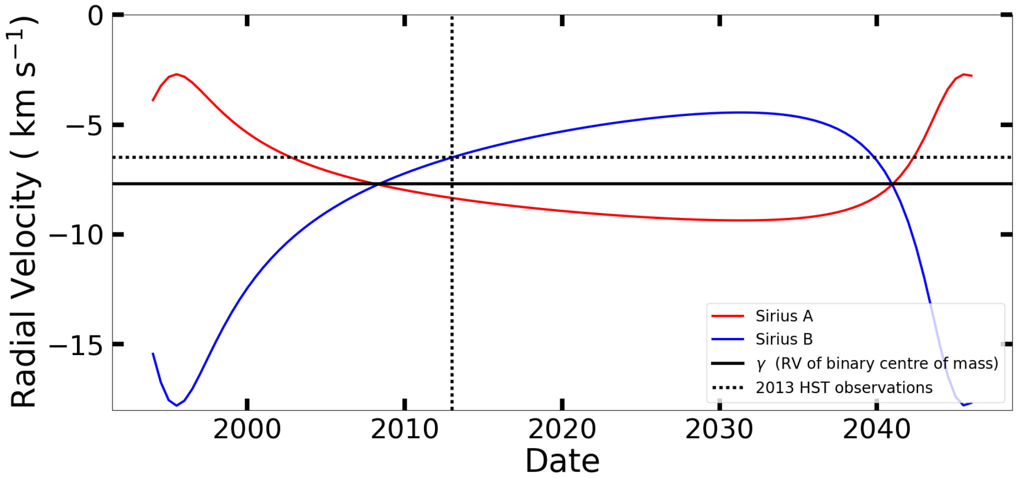

Figure 3.15: Velocity of Sirius A and B at the time of the 2013 observations. The curves are plotted from the tabulated values in appendix (A). The dashed line marks the velocity of Sirius B at the time of the observations.

RV and orbital velocity of Sirius B

The net velocity of Sirius B is taken from Fig. 3.15. This figure uses the tabulated velocities of Sirius A and B listed in appendix (A) based on a model fit to the Sirius A RV measurements and the orbit model of Bond et al. (2017). From this model the velocities are extrapolated into the future to give the velocity at the time of the *HST* observations. The γ velocity of the binary is -7.69 km s^{-1} but the orbital velocity of Sirius B is +1.25 km s^{-1} so this reduces the net velocity. At the time of these observations (26/01/2013) the net velocity of Sirius B is therefore -6.497 km s^{-1} as marked by the dashed line in Fig. 3.15.

Sirius A is large and close enough to have had its angular diameter measured directly by interferometry at 5.936 $\pm$0.016 mas (Kervella et al., 2003). At the distance of 2.36 pc this gives a radius of R = 1.711 $\pm$ 0.013 R$_\odot$. From equation 3.5, using a dynamical mass of 2.042 $\pm$ 0.01 M$_\odot$ Bond et al. (2017), this gives a gravitational redshift of 0.759 km s^{-1} for Sirius A. This produces an additional redshift velocity which must be subtracted.

RV and orbital velocity for 14 Aur Cb, HD2133 B and HR1358 B

The radial velocity for each of the targets was taken from the literature references listed in Table 3.3 which are available on the Simbad database. For HD 2133 the RV listed in Simbad is 45 $\pm$ 2.5 km s^{-1} which gave a final mass measurement inconsistent with the MRR. A new RV measurement for this star is available in the RAVE DR5 database (Kunder et al., 2017) and is much smaller at -1.95 ± 1.56 km s^{-1}. This is the value adopted for this analysis.

The multiple radial velocity measurements needed to acertain the orbital velocity of the MS star and WD are not available for 14 Aur Cb, HD 2133 and HR 1358 B because these systems have very long (100 year plus) orbital periods and have only recently been resolved using *HST*. The magnitude of the white dwarf orbital velocity can be estimated using the apparent semi-major axis and the orbital period. However, since the direction of motion of the white dwarf is not known, this can only be used to estimate the uncertainty in the gravitational redshift velocity rather than apply a correction as was done for Sirius B. The estimated orbital velocities for each white dwarf are listed in Table 3.2. These values are based on the semi-major axis and period of the binary orbit given in Holberg et al. (2013). With limited observations, it is only possible to measure the apparent angular separation a_p listed in column 3. This can be converted in to an estimate of the true semi-major axis a based on the conversion factor $a = 1.11a_p$. The conversion factor is taken from monte carlo simulations which compute the probability distribution of orbital eccentricities and orientations (Dupuy & Liu, 2011). If the orbit is assumed to be circular then the speed of the white dwarf is constant and is given by equation 3.8. This is an upper estimate of the speed with respect to the observer because an orbit with zero inclination (i.e. viewed face on) would have no radial velocity component.

$$v = \frac{2\pi a}{P} \tag{3.8}$$

We do not know which point in the orbit the white dwarf is at, so the velocity could be positive or negative. The estimated speed listed in Table 3.2 column 5 can only be used as a measure of the uncertainty in the v_{gr} value rather than applying it as a correction as was done for Sirius B. The estimated orbital speed is incorporated into the error on the measured velocity by adding it to the uncertainty in the radial velocity. The long orbital periods of these three systems result in low orbital speeds which cause only a moderate uncertainty in the mass measurements.

3.5.3 Results of XSPEC fitting

Examples of the XSPEC fitting for each target are shown in Fig. 3.5 to 3.7. The results of fitting the H-α line in each spectrum are listed in Table 3.4. The values for each spectrum are the average of the four fits for different wavelength ranges. Listed z values have been corrected by subtracting 0.0002762 to account for the

Table 3.2: Estimated white dwarf orbital speed based on the assumption of a circular orbit with the period and semi-major axis taken from Holberg et al. (2013).

Target	Period (Yrs)	a_p (au)	a (au)	v_{orbital} (km s^{-1})
14 Aur Cb	2432.7	207.7	230.5	2.8
HD2133 B	665.03	82.2	91.3	4.09
HR 1358 B	274.53	60.5	67.2	7.3

difference between the air and vacuum rest wavelength. The velocity equivalent to the measured redshift is calculated using equation 3.3 and listed in column 5 (v_{obs}). As mentioned, the correction for the velocity of *HST* were applied to the spectra before fitting. Corrections for the velocity of the white dwarf are applied to (v_{obs}) according to equation 3.7 which leaves only the velocity attributed to the gravitational redshift (v_{gr}, column 6)

Table 3.3: Correction factors calculated for each spectrum.

Obs ID	Net radial velocity (km s^{-1})	HST Orbital velocity (km s^{-1})	slit angle offset (km s^{-1})
Sirius B	-	-	
Wide slit (52 x 2)			
obt801050	-7.256[a]	-5.467	-1.9
obt801060	"	-3.804	-0.6
obt801070	"	-3.068	0.6
obt801080	"	3.146	1.9
Narrow slit (52 x 0.05)			
obt801090	-7.256	6.64	-1.71
obt8010a0	"	7.198	-0.57
obt8010b0	"	7.504	0.57
obt8010c0	"	7.550	1.71
	Radial velocity of binary (km s^{-1})		
14 Aur Cb			
Wide slit (52 x 0.5)			
obt804030	-8.4 ± 0.5[b]	-2.4	-0.63
obt804040	"	-1.4	0.63
Narrow slit (52 x 0.05)			
obt804010	"	-3.9	-0.63
obt804020	"	-3.5	0.63
HD2133 B			
Narrow slit (52 x 0.2)			
obt802030	45 ± 2.5[c]	-1.5	-0.63
obt802040	"	-2.5	0.63
HR1358 B			
Wide slit (52 x 0.2)			
obt808030	39.2 ± 0.3[d]	4.1	-0.63
obt808040	"	5.3	0.63
Narrow slit (52 x 0.05)			
obt808010	"	-1.9	-0.63
obt808020	"	1.6	0.63

[a]Includes γ, K_{WD} and MS_{Vgr}
[b](Gontcharov, 2006)
[c](Kunder et al., 2017)
[d](Pourbaix et al., 2004)

Table 3.4: Measured z, velocity and mass for Sirius B 2013 data.

Obs ID	z	Wavelength (Å)	$\Delta\lambda$ (Å)	v_{obs} (km s^{-1})	v_{gr} (km s^{-1})	Mass ($M_\odot$)
Sirius B	-		-			
Wide slit (52 x 2)						
obt801050	2.8199e-04	6566.46	1.851 ± 0.033	84.54	93.70	1.183 ± 0.011
obt801060	2.9723e-04	6566.56	1.951 ± 0.060	89.11	96.96	1.224 ± 0.016
obt801070	2.9235e-04	6566.53	1.919 ± 0.027	87.65	94.30	1.191 ± 0.010
obt801080	2.9340e-04	6566.53	1.925 ± 0.023	87.96	93.31	1.178 ± 0.009
Average						1.194 ± 0.049
Narrow slit (52 x 0.05)						
obt801090	2.6279e-04	6566.33	1.725 ± 0.041	78.78	87.75	1.108 ± 0.012
obt8010a0	2.8720e-04	6566.49	1.885 ± 0.045	86.10	93.93	1.186 ± 0.013
obt8010b0	2.8168e-04	6566.46	1.849 ± 0.019	84.45	91.13	1.151 ± 0.009
obt8010c0	2.8472e-04	6566.48	1.869 ± 0.025	85.36	90.90	1.148 ± 0.009
Average						1.148 ± 0.080

Table 3.5: Measured z, velocity and mass for 14 Aur Cb, HD2133 B and HR1358 B, 2013 data.

Target	Obs ID	z	Wavelength (Å)	$\Delta\lambda$ (Å)	v_{obs} (km s^{-1})	v_{gr} (km s^{-1})	Mass ($M_\odot$)
14 Aur Cb	Wide slit (52 x 0.5)						
	obt804030	7.1083e-05	6565.07	0.467 $\pm$ 0.117	21.31	30.34	0.642 $\pm$ 0.055
	obt804040	4.3508e-05	6564.89	0.286 $\pm$ 0.165	13.04	20.81	0.440 $\pm$ 0.071
	Narrow slit (52 x 0.05)						
	obt804010	1.0622e-04	6565.30	0.697 $\pm$ 0.113	31.84	40.87	0.864 $\pm$ 0.055
	obt804020	-7.4005e-06	6564.56	-0.049 $\pm$ 0.303	-2.22	5.55	0.117 $\pm$ 0.122
	Average						0.516 $\pm$ 0.747
HD 2133 B	Narrow slit (52 x 0.2)						
	obt802030	-6.3486e-05	6564.19	-0.417 $\pm$ 0.445	-19.03	-16.45	-0.362 $\pm$ 0.188
	obt802040	3.5261e-05	6564.84	0.231 $\pm$ 0.028	10.57	11.89	0.261 $\pm$ 0.052
	Average						-0.050 $\pm$ -0.441
HR 1358 B	Wide slit (52 x 0.2)						
	obt808030	2.3326e-04	6566.14	1.531 $\pm$ 0.114	69.93	31.36	0.609 $\pm$ 0.073
	obt808040	2.2294e-04	6566.07	1.463 $\pm$ 0.058	66.84	27.01	0.524 $\pm$ 0.063
	Narrow slit (52 x 0.05)						
	obt808010	2.3471e-04	6566.15	1.540 $\pm$ 1.360	70.36	31.79	0.617 $\pm$ 0.492
	obt808020	2.0649e-04	6565.96	1.355 $\pm$ 1.623	61.90	22.07	0.429 $\pm$ 0.585
	Average						0.545 $\pm$ 0.189

3.5.4 Reliability of fitting results

For 14 Aur Cb, HD2133 and HR1358 there is a problem with the spectra giving inconsistent results as can be seen in Table. 3.5. This is partly due to lines being much shallower and the data noisier than the Sirius B lines. When the lines are shallow, the data do not constrain the z parameter well as the model could be shifted horizontally without much change in the reduced χ^2.

Reduced χ^2 contour plots

The degree to which the z parameter is well constrained is illustrated in Fig. 3.17 to 3.21 which were produced by shifting the model through a pre-defined range of z values in steps of 1×10^{-7} and recording the reduced χ^2 for each.

As an aid to providing an objective comparison between spectra, the reduced χ^2 vs z plots show a region marked in black where the reduced χ^2 is within 1 per cent of the minimum value. Once the reduced χ^2 value is more than 1% above the minimum it is plotted in grey. It is then possible to compare how well the z value is constrained by measuring the z range covered by the 1% region. A 1% change in reduced χ^2 was chosen because most spectra were found to produce a reduced χ^2 plot which increased by 1% within a realistic range of z values. Table 3.6 gives the minimum χ^2 value for each spectrum and the corresponding z value. Column 5 gives the z range over which χ^2 is within 1% of the minimum.

Sirius B has a well defined minimum χ^2 with the 1% region covering a range of only 0.25×10^{-4} to 0.87×10^{-4} in z before increasing rapidly. For the other targets, χ^2 only changes by 1 per cent over a range of $1 - 2 \times 10^{-4}$ in z as indicated by the solid black region of the contour in Fig. 3.17 to 3.21. 14 Aur Cb is particularly poorly constrained, ranging up to 4.8×10^{-4} in z. An additional problem is that some of the fits have several local minima where the fitting can get stuck, giving a misleading result. It was found in Fig. 3.16 that when the mass values were calculated by combining z measurements from all spectra for a target, there was very large uncertainty in the data points due to the spread from individual spectra. The mass values calculated in this way place very little constraint on the MRR.

3.5.5 Method to systematically identify unreliable results

Improved results can be obtained by using a systematic method to assess the reliability of each measurement and reject those which can be considered unreliable. The method developed involves a two-step process.

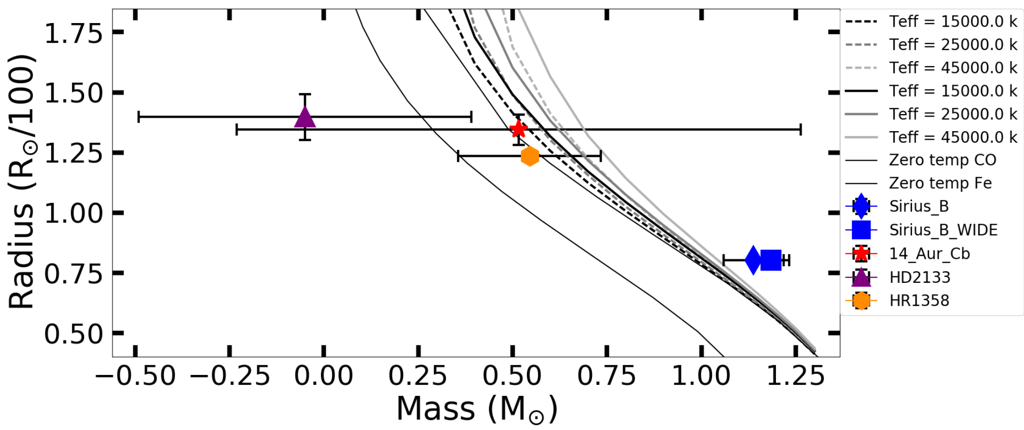

Figure 3.16: MRR plotted with the mass calculated from the gravitational redshift measurements.

Step 1: Identify appropriate z value to start fit

The reduced χ^2 plots and Table 3.6 described above are used to identify the correct z range to start the fitting process so that the fitting is confined to a reasonable range of z and avoid getting stuck in a local minimum. The selection of the starting z value was based mainly on finding the global minimum in the contour plot which works well when the data is good and the contour plot has an obvious minimum with the reduced χ^2 value increasing rapidly for z values either side of the minimum. For some spectra, reduced χ^2 is relatively flat over a large range of z. There are also cases where there are two minima. In these cases, the starting z value was selected based on the starting point selected for other spectra of the same target as long as the starting point was still within the 1 per cent reduced χ^2 range for the spectrum in question.

Step 2: Identify reliable results

The fitting is repeated for each of the four wavelength ranges 8, 64, 120 and 176 Å . The next step is to look at the results from all spectra from a single target to identify outliers and calculate a best estimate of the correct z value.

The method adopted for finding robust z measurements from the full set of spectra is as follows. The full set of results for each target is plotted as in Fig. 3.22 to 3.26 which show the z parameter on the x axis and the best fit z value from each spectrum and pixel range stacked up in the y direction. There are four pixel ranges so each individual spectrum results in four horizontal lines. An initial calculation of the average z is done with all results. A sigma clipping algorithm is then used to identify and exclude any data points which differ from the average by more than 3σ. The sigma clipping works by calculating how many sigma each measurement is away from the average and deleting measurements which are above a set sigma value. The average is then recalculated and the procedure repeated with a smaller σ. This is iterated with reducing σ limits of 3, 2.5, 2 and 1.5 σ until a final average z value is reached. The limit of 1.5 σ was used because many of the measurements have large uncertainty and none were removed if the sigma threshold was too large. Any data points which were discarded are plotted as faded out markers. The horizontal line indicates the final average z value with the standard error in the average indicated by the dashed lines.

3.5.6 Details of fitting results for each target

Sirius B For the narrow slit spectra, the reduced χ^2 contour in Fig. 3.17 increases relatively rapidly either side of the minimum z value. z can only vary by $\sim 0.4\times10^{-4}$ before the χ^2 increases by more than 1 per cent. This is indicated in the plot by the black line which changes to grey when the χ^2 value is more than 1 per cent above the minimum. The best fit z value is the same across the four spectra as shown by the overlapping 1 per cent χ^2 regions. The horizontal lines are close together showing that the best fit using the 176 Å range is similar to the average of the fit when using the three narrower ranges. None of the plots show a second minimum which could be an alternative fit.

For the wide slit spectral results in Fig. 3.18, the top two panels (050 and 060) give results almost identical to the narrow slit spectra. The lower two panels (070, 080) are consistent with a best fit z value at 5.7×10^{-4} but have a much shallower χ^2 contour showing that the z value is not al well constrained. The 070 spectrum has a particularly poorly defined best fit z value. This is reflected in Fig. 3.23 which shows that when more restricted wavelength ranges are used, the fitting becomes inconsistent with the values found for the other 3 spectra. The results from 070 were not included in the calculation of the final z value for this reason.

14 Aur Cb The χ^2 contours for 14 Aur Cb do not clearly identify a specific z value as the best fit. However, all apart from the second (020) spectrum indicate that it is in the range 3 - 4 $\times10^{-4}$. The full set of results shown in Fig. 3.24 shows that each individual measurement has a large uncertainty spanning up to 2×10^{-4}. The two wide slit spectra (purple and green) have the smallest uncertainty and are always consistent with a z value of 3.4×10^{-4}. The two narrow slit spectra (gold, red) have greater error ranges and fall either side of the average, but they are all consistent with the average within the measurement errors.

HD 2133 B There are only two G750M spectra for HD 2133 B and in Fig. 3.20 it can be seen that the z values they give are incompatible. The spectrum in Fig. 3.6 (Top panel) reveals that the 030 spectrum is affected by a spike in the noise right in the middle of the H-α line. Calculations showed that the mass derived from the z value from the obt802030 spectrum is unrealistically low. Given the clear evidence for an anomaly with this spectrum, it was decided to exclude this spectrum from the final z measurement for HD 2133 B.

HR 1358 B The wide slit spectra in Fig. 3.21 lower two panels clearly place z at 5×10^{-4}. The steep rise in χ^2 either side of this value show that the fit is robust. The narrow slit spectra on the other hand (upper panels) give a lower z value around 3.8×10^{-4}, albeit with the χ^2 still within 1 per cent of the minimum up as far as $z = 5 \times 10^{-4}$. The average from the four wavelength ranges fitted does in fact fall closer to 5×10^{-4}, which is indicative that the unusually low z values were only valid when large portions of the wings were included in the fit. Fig. 3.26 confirms this assessment, with both of the narrow slit spectra giving widely scattered results for the four fitting ranges (gold and red markers). The wide slit spectra give consistent results centred around the final z value of 5×10^{-4} (purple and green markers).

Table 3.6: Minimum χ^2 values and corresponding z value for each of the H-α spectra fitted to measure the redshift z. Column 5 is the range in z where the χ^2 value is within 1 per cent of the minimum and indicates how well the z values in column 4 are constrained.

Spectrum	Minimum χ^2	Degrees of freedom	z at min χ^2 ($\times 10^{-4}$)	z range within 1 % of of min χ^2 ($\times 10^{-4}$)
Sirius B				
obt801050	616.6	312	5.598	0.25
obt801060	576.4	314	5.762	0.258
obt801070	623.5	314	5.697	0.265
obt801080	823.2	314	5.726	0.323
obt801090	4899.9	310	5.435	0.625
obt8010a0	1661.2	311	5.703	0.384
obt8010b0	5517.8	311	5.693	0.869
obt8010c0	2682.6	311	5.657	0.428
14 Aur Cb B				
obt804010	389.2	300	4.166	4.826
obt804020	329.2	301	5.38	2 minima
obt804030	486.6	300	5.858	4.504
obt804040	307.4	292	3.284	1.839
HD 2133 B				
obt802030	421.5	281	2.08	1.38
obt802040	418.0	302	3.09	0.913
HR 1358 B				
obt808010	960.6	297	3.825	2.003
obt808020	700.6	294	3.665	2.06
obt808030	622.5	298	5.015	0.986
obt808040	686.7	293	4.817	1.192

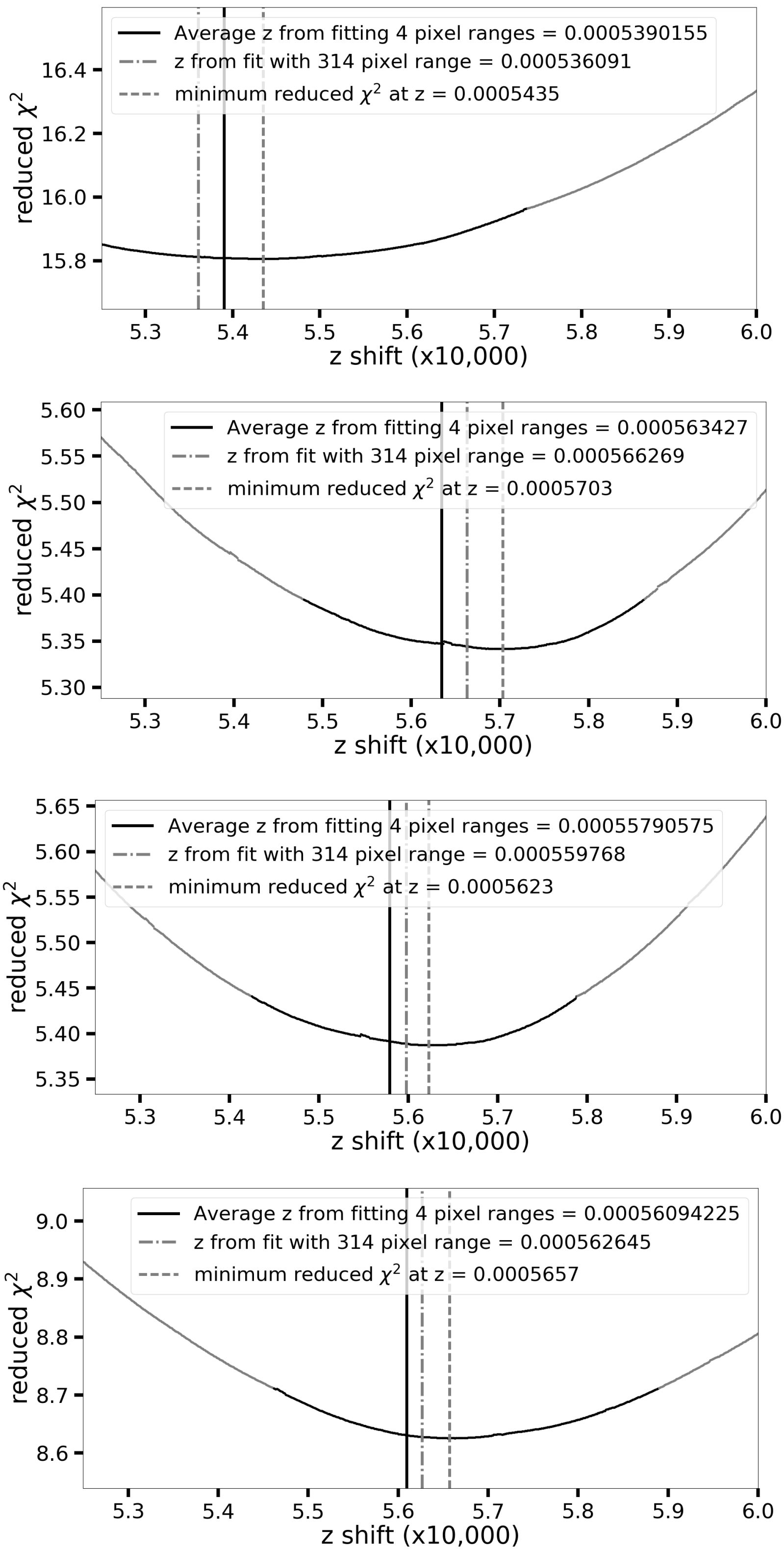

Figure 3.17: Sirius B, Narrow slit. Reduced χ^2 as a function of z. From top to bottom, obt801090, ...0a0, 0b0 and 0c0.

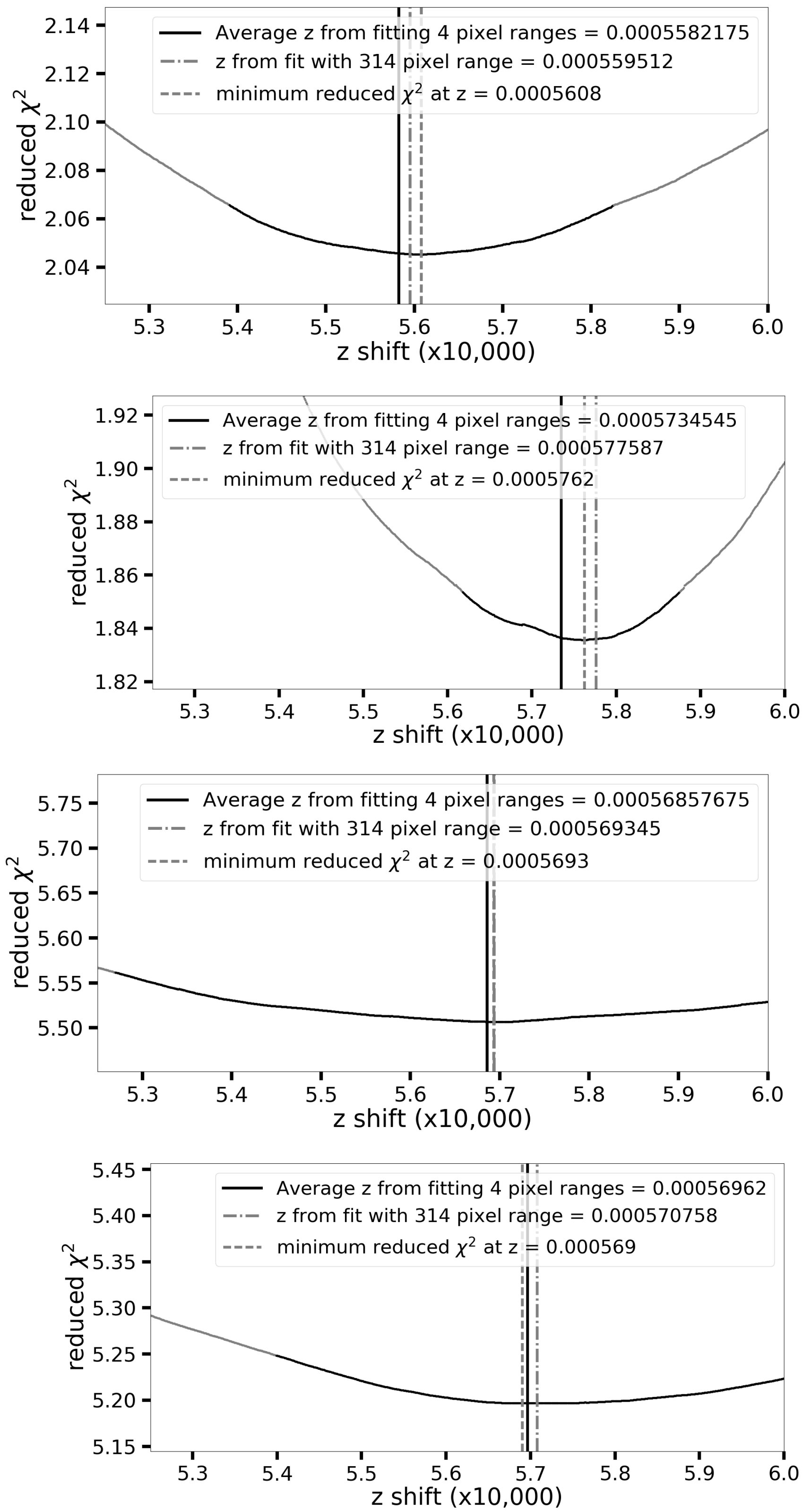

Figure 3.18: Sirius B wide slit (52x2). Reduced χ^2 as a function of z. From top to bottom obt801050, 060,070 and 080.

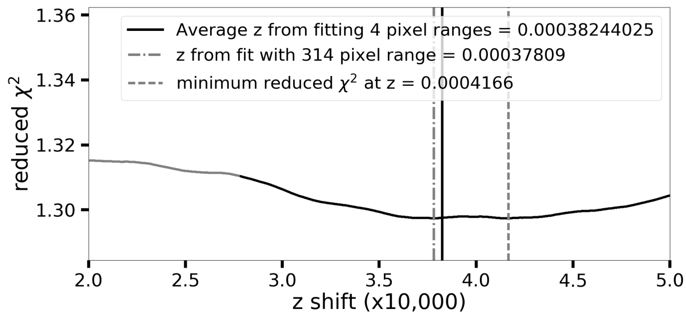

(a) 14 Aur Cb, 010

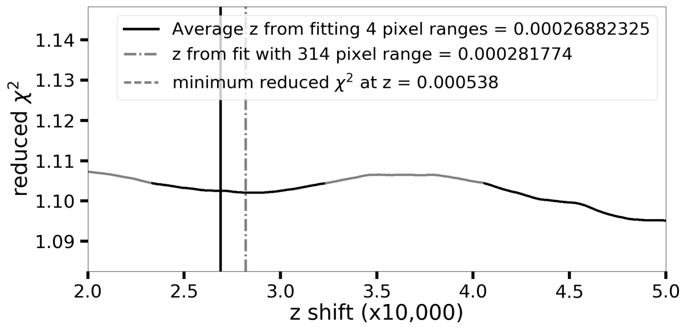

(b) 14 Aur Cb, 020

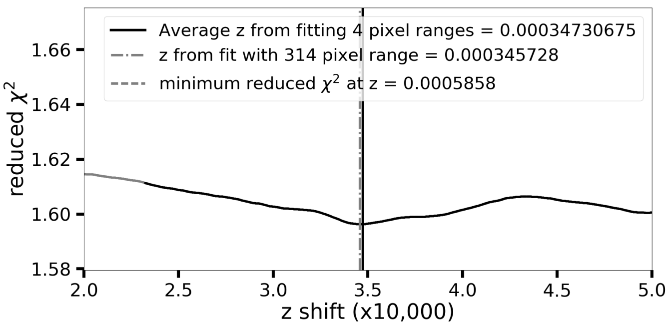

(c) 14 Aur Cb, 030

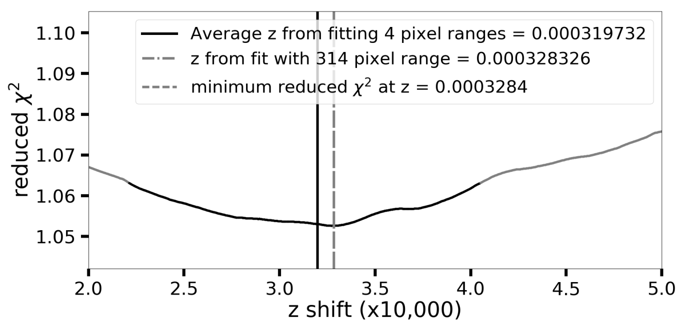

(d) 14 Aur Cb , 040

Figure 3.19: Reduced χ^2 as a function of z.

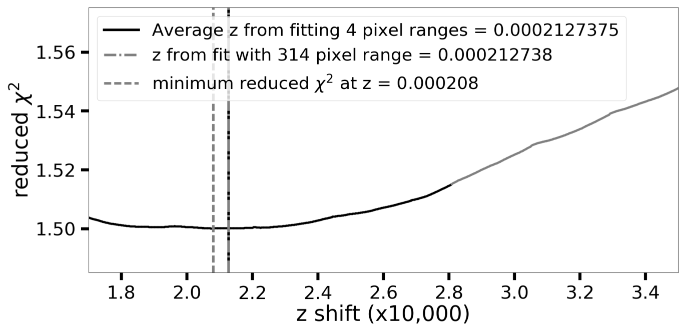

(a) HD2133, 030

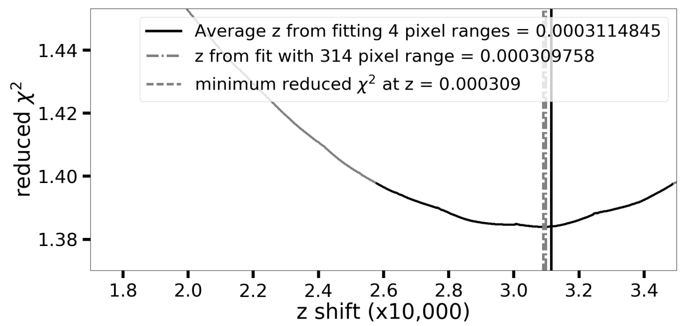

(b) HD2133, 040

Figure 3.20: Reduced χ^2 as a function of z.

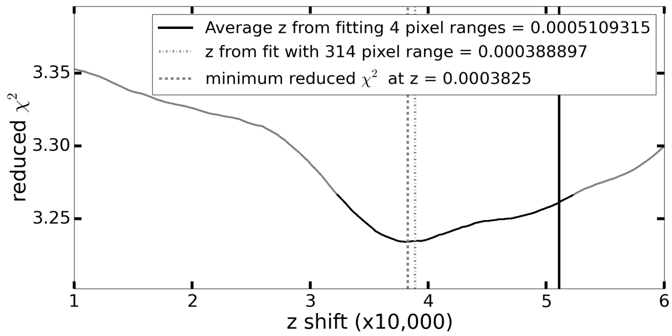

(a) HR1358 B, narrow slit,obt808010

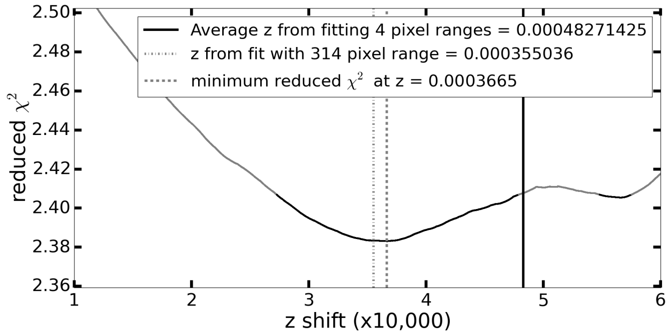

(b) HR1358 B, narrow slit, obt808020

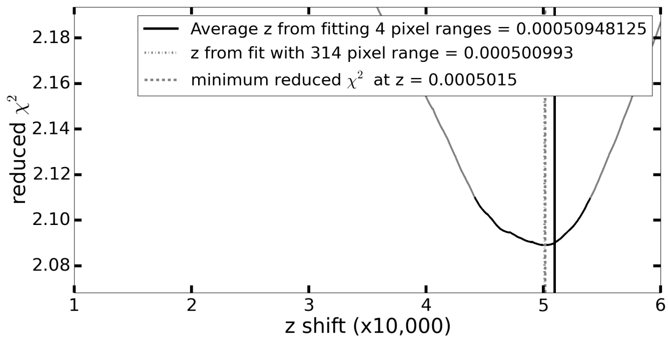

(c) HR1358 B, wide slit, obt808030

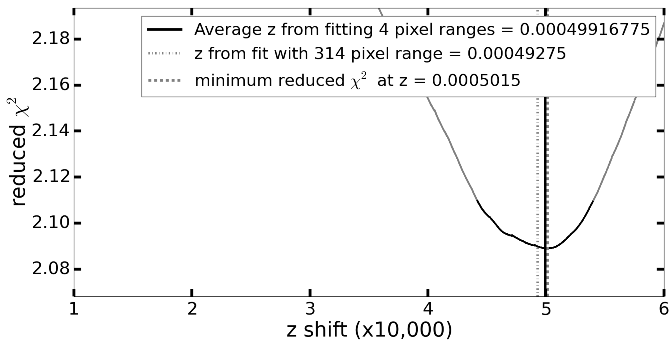

(d) HR1358 B , wide slit, obt808040

Figure 3.21: Reduced χ^2 as a function of z.

Table 3.7: Final results for wavelength measurements and calculated mass using the gravitational redshift. Measured z using sigma clipping method described in section 3.5.5.

Target	z	Wavelength (Å)	$\Delta\lambda$ (Å)	v_{obs} (km s^{-1})	v_{gr} (km s^{-1})	Mass ($M_\odot$)
Sirius B Narrow slit	2.7830e-04 ± 1.2753e-06	6566.435	1.827	83.43	90.69	1.145 ± 0.008
Sirius B Wide slit	2.8902e-04 ± 7.2781e-07	6566.505	1.897	86.65	93.90	1.186 ± 0.008
14 Aur Cb	5.3352e-05 ± 1.1232e-05	6564.958	0.350	15.99	24.39	0.516 ± 0.041
HD 2133 B	3.3159e-05 ± 7.7921e-07	6564.825	0.218	9.94	11.89	0.261 ± 0.051
HR 1358 B	2.2631e-04 ± 3.2825e-06	6566.093	1.486	67.85	28.65	0.556 ± 0.060

Result

The final z value for each white dwarf is listed in Table 3.7 based on taking the average of the z measurements from all spectra for each target and rejecting any measurements which do not agree within 1.5 σ using the iterative method described above. After corrections for the radial velocity of the binary are applied, the final mass values are plotted in Fig. 3.31.

3.6 Discussion

3.6.1 Comparison of results obtained from the two z methods

The theoretical MRR with the full set of gravitational redshift results is plotted in Fig. 3.16 using all the spectra and in Fig.3.31 using the selective process described above. They show that when the mass is calculated from each spectrum individually there is a large scatter in results and the data is not consistent with the MRR. In contrast, when the process of selecting reliable z values is applied, the results follow the expected trend.

3.6.2 Comparison with spectroscopic results and the MRR

The results obtained with the gravitational redshift can be compared to those derived from the Lyman/Balmer line fitting in the previous chapter. These comparisons are plotted for each star individually in Fig. 3.27 to 3.30.

Sirius B

The gravitational redshift mass for Sirius B is inconsistent with the MRR, as well as the dynamical and spectroscopic mass which are plotted as green and red diamonds respectively in Fig. 3.27. There is also a smaller but still significant difference between the mass using the narrow and wide slits (blue diamond and purple square). This difference between the narrow and wide slit results indicates that there is a systematic instrumental effect which is causing the discrepancy between this result and the other methods. The consistency between the results for each of the four spectra taken through each slit is very good as shown in Fig. 3.22 and Fig. 3.23. It should be noted that the scale on the x axis is very small compared to the same plots for other targets.

The errorbars on the Sirius B data points are only just visible in the figure which is an indication of the small spread in results obtained from the 4 individual spectra. From the significant difference between the wide and narrow slit results, it

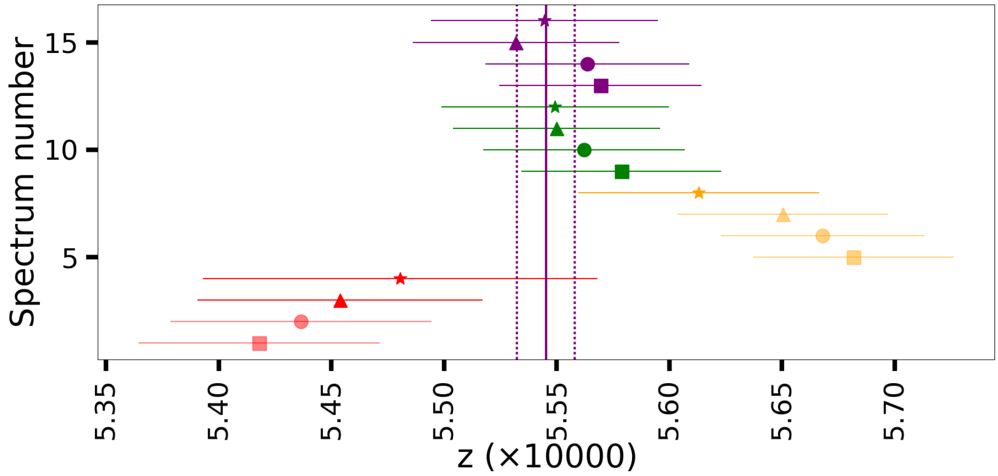

Figure 3.22: Sirius B, narrow 52 x 0.05 slit: z shift measured from four wavelength ranges (8 (star), 64 (triangle), 120 (circle), 176 (square) Å) for all four spectra taken with the narrow 52 x 0.05 slit. Colours indicate the spectra used. obt801090,...0a0, 0b0 and 0c0 are red, gold, green and purple respectively. Faded markers are outliers and are not included in the calculation of the average z value indicated by the vertical purple line.

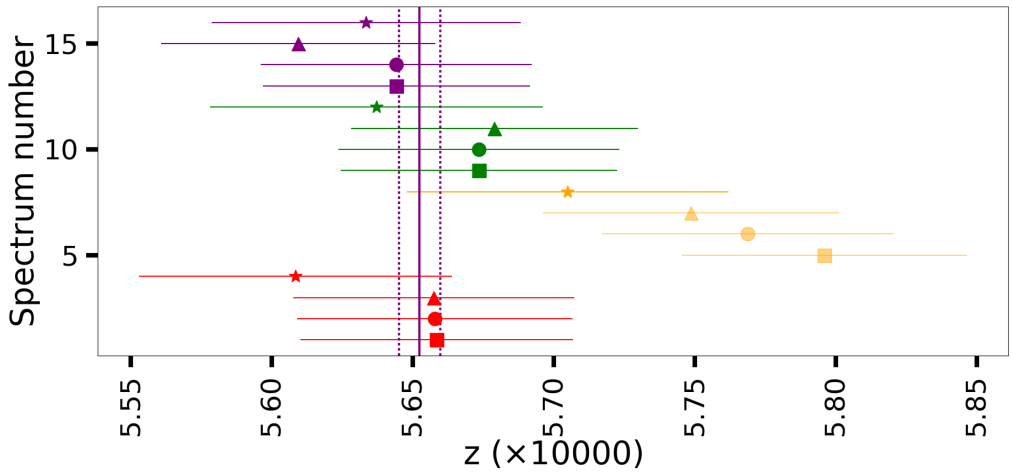

Figure 3.23: Sirius B, wide 52 x 2 slit: Same as previous figure but using the wide slit spectra.

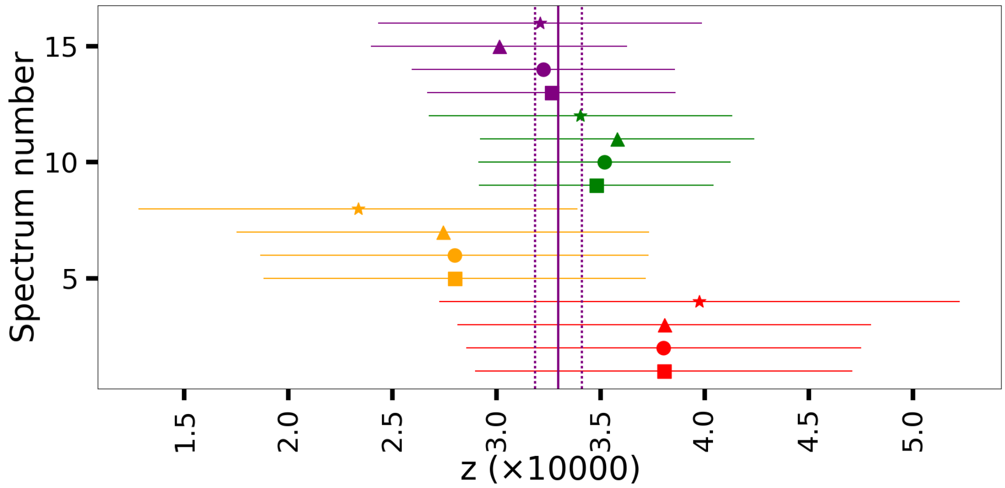

Figure 3.24: 14 Aur Cb: Same as Fig.3.22. The wide 52 x 0.5 slit spectra are obt804030, ...040 (green, purple). Narrow slit 52 x 0.05 spectra are obt804010, ...020 (red, gold).

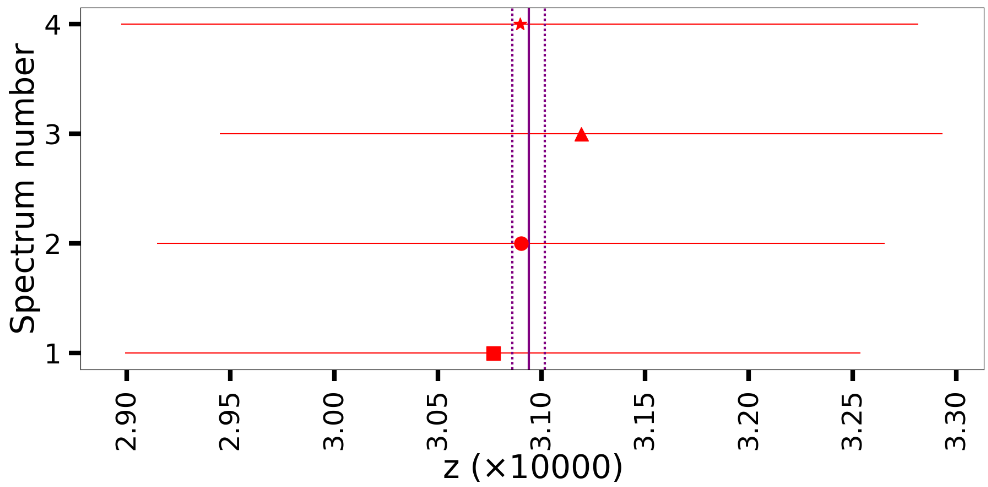

Figure 3.25: HD2133 B: Only the obt802040 spectrum was used as the 030 spectrum was shown to give an unrealistic (negative) mass.

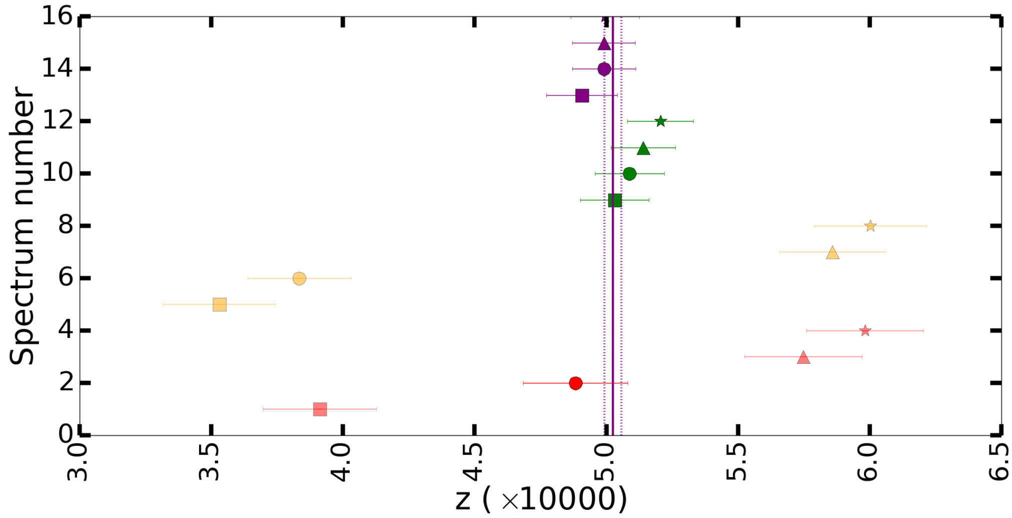

Figure 3.26: HR1358 B: The wide slit spectra (purple and green) give consistent results. The narrow slit spectra (gold and red) show a large variation depending on the range of the wings included in the fit. These are unreliable and excluded from the final z measurement.

must be concluded that there are systematic effects which have not been corrected for. The disagreement with the MRR, as well as gravitational mass being ~ 15 per cent larger than the dynamical mass, is further evidence that there measurements are subject to an unknown systematic offset, probably of instrumental origin. Despite this discrepancy, the precision achieved is very good, with an uncertainty of only 0.008 $M_{\odot}$. This makes it likely that this method of studying the MRR can provide a very useful test, with precision sufficient to distinguish between H-layer thickness and temperature even in this high mass range. However, this will require further work to identify and correct the systematic offset.

14 Aur Cb

In Fig.3.28 the gravitational redshift mass is below the MRR for the temperature of 45,824 K. It is consistent with the spectroscopic mass from *HST* within 1σ. The larger error on the spectroscopic mass makes it formally consistent with the thin H-layer model at the correct temperature, in agreement with the *FUSE* result. It is possible that the lower gravitational mass is due to an underestimate of the effect of the WD orbital velocity. The result may also be subject to an instrumental offset similar to that affecting Sirius B.

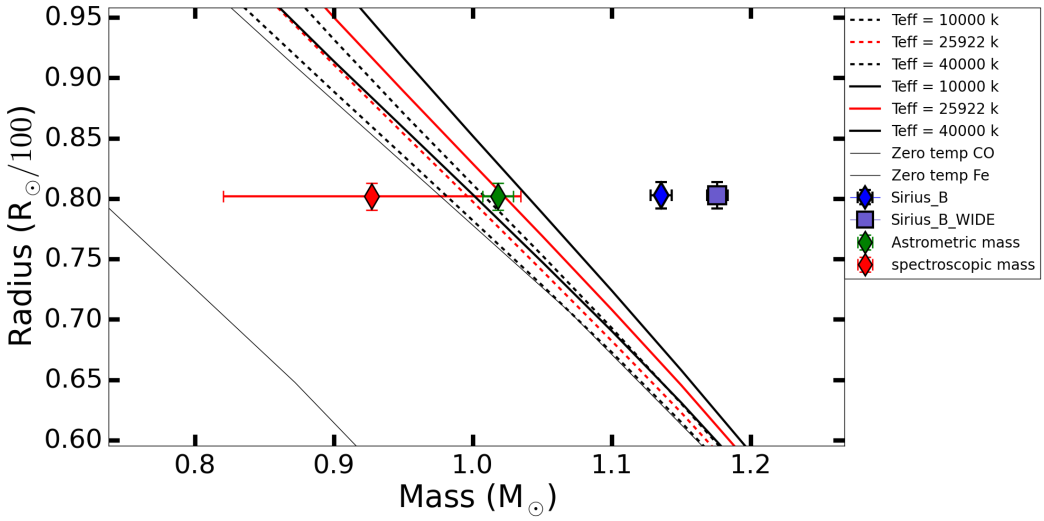

Figure 3.27: Sirius B mass from the gravitational redshift compared to the spectroscopic and dynamical mass.

HD 2133 B

The gravitational redshift mass is within 1σ of both the far-UV and optical spectroscopic mass which is added evidence that these mass measurements are correct rather than a random error. Fig. 3.29 confirms that all three mass measurements for this star are below the C/O core MRR and are in fact consistent with a zero temperature Fe core model. A similar group of white dwarfs consistent with or below the Fe core MRR was noted by Bédard et al. (2017). The convergence of all three mass measurements for HD 2133 B strongly suggests that this white dwarf is peculiar in some way and is a member of this unexplained population of white dwarfs.

HR 1358 B

The gravitational mass is exactly on the line for a MRR of 20,790 K with a thin H-layer. As shown by the dashed red line in Fig. 3.30. The spectroscopic mass is inconsistent with this result, possibly due to problems with the scattered light affecting these spectra. However, both measurements are consistent with the MRR.

3.7 Conclusion

The gravitational redshift method has provided high precision mass measurements for four white dwarfs. The results for three of the stars are in agreement with

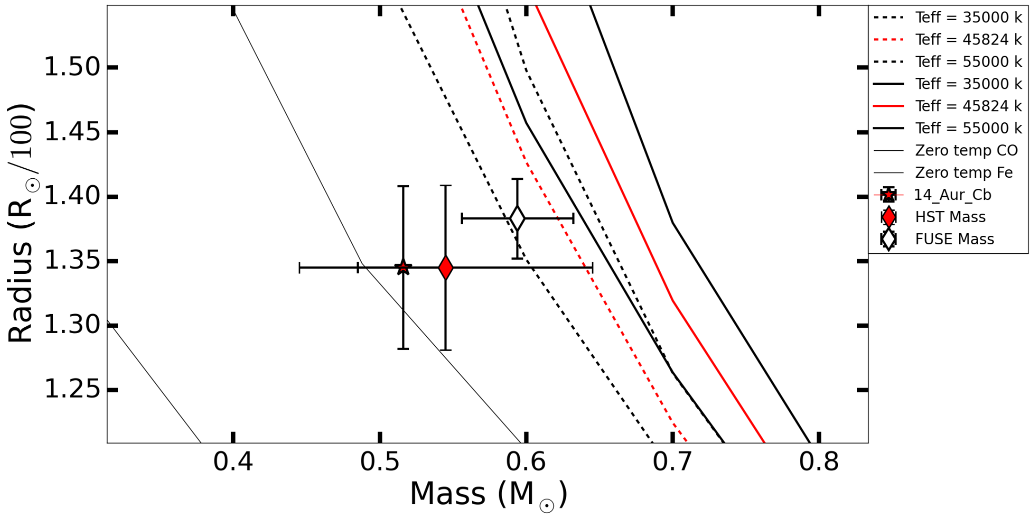

Figure 3.28: 14 Aur Cb mass from the gravitational redshift compared to the spectroscopic mass

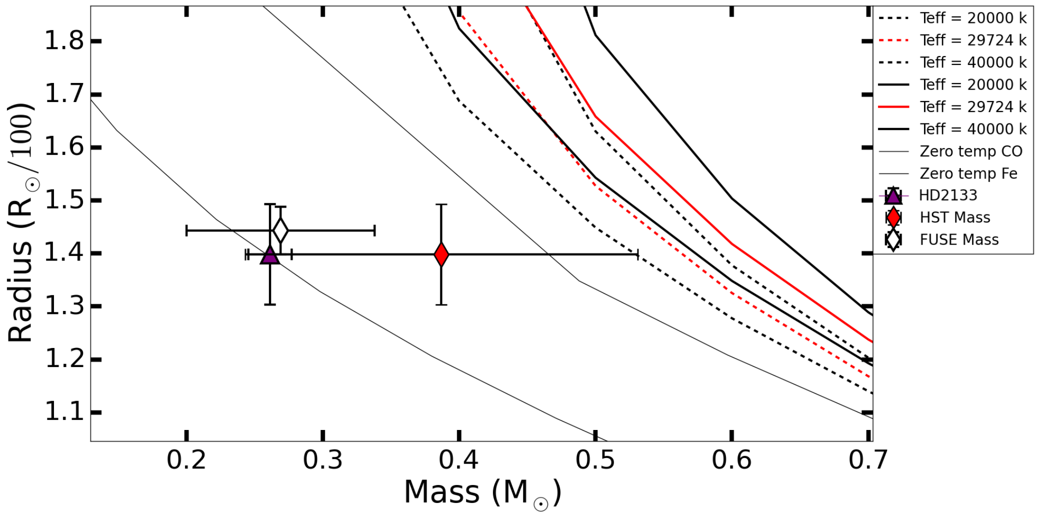

Figure 3.29: HD 2133 B mass from the gravitational redshift compared to the spectroscopic mass

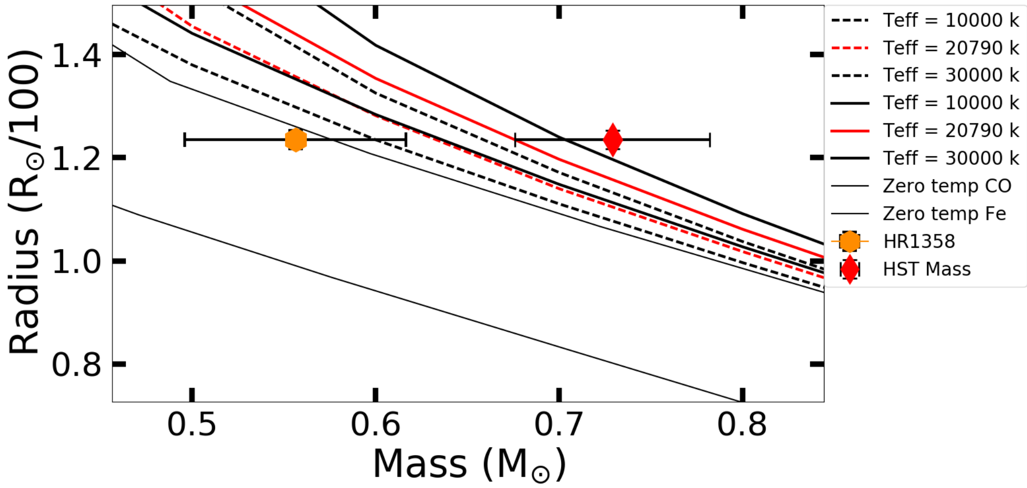

Figure 3.30: HR 1358 B mass from the gravitational redshift compared to the spectroscopic mass

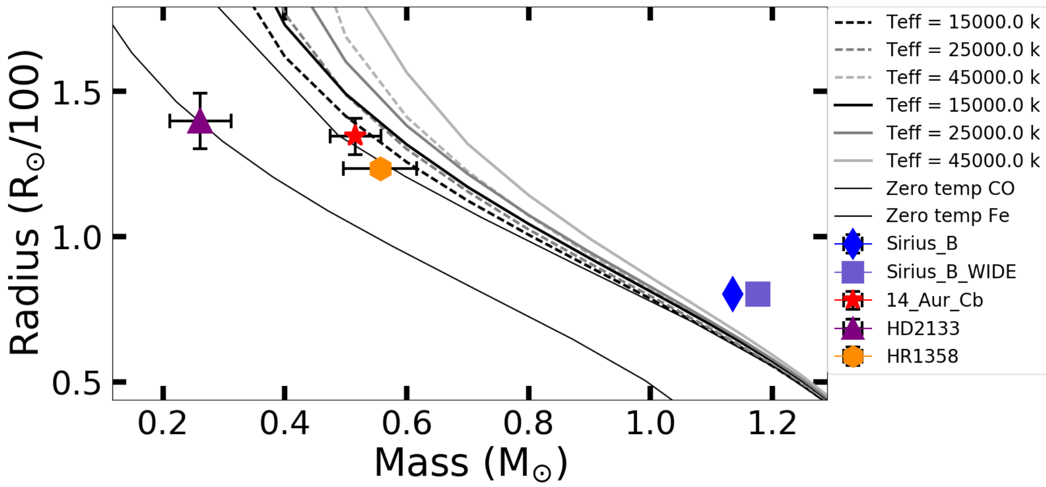

Figure 3.31: The mass-radius relation measured using the gravitational redshift. Sirius B, 14 Aur Cb, HD2133 B and HR1358 B

the C/O core MRR models of Fontaine, Brassard & Bergeron (2001). This result supports the validity of the MRR. The result from Sirius B, though not consistent within 1σ clearly follows the expected trend of the MRR. The ~ 0.1 $M_{\odot}$ offset is likely to be the results of an instrumental effect, as shown by the difference between the wide and narrow slit measurements.

The remaining white dwarf, HD 2133 is only consistent with a Fe zero-temperature model. The low mass of ~ 0.3 $M_{\odot}$ found for HD 2133 is consistent within 1σ with the spectroscopic mass for this star which makes it more likely that this measurement is correct rather than a random error. If this is the case, then the low mass of HD 2133 below 0.5 $M_{\odot}$ indicates that this white dwarf is not the product of single star evolution and may have interacted with its companion in a way which has altered its structure compared to a normal white dwarf.

When compared to the spectroscopic results in chapter 2, all targets are consistent within 2σ of both the far-UV and optical mass. Sirius B is the notable exception, with the gravitational redshift and spectroscopic mass approximately 0.1 $M_{\odot}$ above and below the dynamical mass.

The overall conclusion for the gravitational redshift method is that it can provide higher precision than the spectroscopic method, but it requires careful analysis to reduce the uncertainty introduced by less reliable measurements. The results support the MRR, but there is a potential systematic offset which needs to be investigated before drawing conclusions.

Chapter 4

A differential measurement of the gravitational redshift of Sirius B using *HST*

> *"Therefore the clock goes slowly when it is placed in the neighbourhood of ponderable masses. It follows from this that the spectral lines in the light coming to us from the surfaces of big stars should appear shifted towards the red end of the spectrum."*
>
> \- Albert Einstein, *1916*

4.1 Overview

The previous chapters have shown that there is a serious discrepancy between the mass obtained from the spectroscopic and gravitational redshift method for Sirius B. The gravitational mass is also significantly higher than the dynamical mass (Bond et al., 2017). As one of the few white dwarfs that constrains the high mass end of the mass-radius relation, it is important to investigate the cause of this discrepancy. Sirius B is also a rare example where all 3 methods of mass determination can be applied and the results compared. In this chapter I present analysis of *HST* observations which were carried out with the aim of making an accurate gravitational redshift measurement of Sirius B and uncovering the cause of the discrepancy in the gravitational redshift method.

4.2 Introduction

The difference between the 3 mass estimates of Sirius B was first noted in Barstow et al. (2005) using data taken in 2004 (GO program 12606, PI Barstow). The 2005 analysis was based on a single spectrum. The results of chapter 3 showed that, for the spectroscopic method, the derived mass from 4 spectra had a scatter of 0.1 $M_\odot$. If the gravitational redshift method has a similar degree of scatter, this could explain the apparent discrepancy. However, the results of analysis of multiple spectra taken in 2013 (discussed in chapter 3) have confirmed that the mass estimate given by the two methods are significantly different and can not be explained as simply an underestimate of the uncertainties involved.

In the previous analysis, I considered all the possible systematic errors such as the orbital velocity of the *HST* and the corrections due to the rest wavelength being measured in a vacuum versus on Earth. It is possible that unknown instrumental or systematic effects are responsible for the mass discrepancy. Such effects could not be detected in the previous analysis because the reference rest wavelength is taken from lab based measurements. What is required is a point of reference taken with the same instrument at the same time which can be used to uncover any problems with the calibration or analysis method.

The aim of this investigation is to resolve this discrepancy by using the traditional method of measuring the gravitational redshift of the white dwarf relative to the luminous primary, in this case Sirius A. In this way, the same instrument is used to provide both the reference wavelength and the white dwarf spectrum which cancels out any instrumental wavelength shift. The observations were planned so as to measure the wavelengths of the H-α lines in both Sirius B and A using the same STIS G750M grating during the same visit. This removes many of the systematic uncertainties affecting previous observations, although some effects, such as the changing orbital velocity of *HST* relative to the target, still have to be taken into account.

This investigation will provide a high precision test of the mass-radius relation at the high mass end where very few white dwarfs are suitable for study. Also, by comparing the results to those from other methods it will provide a test of the analysis method and help to uncover any unknown systematics. This will either allow us to confirm the validity of this fundamental method and the mass-radius relationship, or it may uncover a gap in our theoretical understanding which needs to be addressed.

Table 4.1: Spectra of Sirius A and B taken with *HST* on 12/01/2018. Program 15237, (PI Joyce, Barstow)

Obs ID	CCD position (Centre or E1)	Exp time (s)	Time of exposure (GMT)
Sirius B			
ODL601010	E1	100	03:32:40
ODL601020	E1	100	03:36:14
Sirius A			
ODL601030	E1	0.2	03:39:59
ODL601040	E1	0.2	03:41:29
ODL601050	Centre	0.9	03:53:36
ODL601060	Centre	0.9	03:56:17
Sirius B			
ODL601070	Centre	75	04:01:35
ODL601080	E1	75	04:04:16

4.3 Data and observing strategy

The data for this study was obtained as part of GO program 15237, (PI Joyce, Barstow) in cycle 25 at the start of 2018. The data consist of 4 exposures each for Sirius A and B. All spectra were taken with the G750M grating which covers the wavelength range 6295 - 6867 Å and captures the broadened wings of the WD H-α line centred at $\sim$ 6564 Å. This set up has a resolution of 0.56 Å/ pixel. This resolution is lower than the approximately 0.26 Å which is the size of the discrepancy from the 2013 observations. However, by fitting a model to the broadened line, cross correlation improves the accuracy of the wavelength measurement by a factor of 10 (Barstow et al., 2005).

Exposure times were calculated to give a S/N > 100 for Sirius B. For Sirius A, the target is bright enough to saturate within 0.1 s. This is shorter than the minimum exposure time of 0.3 s which is limited by the shutter speed. Previous observations (Bohlin, 2014) have shown that the spectrum can be recovered even though it is saturated.

One of the major challenges with this observation is the close proximity of Sirius A which has the potential to contaminate the spectrum of Sirius B. To avoid this problem, the narrow 52x0.05 arcsecond slit was used which excludes light from any nearby sources. Also, the orientation of the spacecraft was selected so that the long slit would be perpendicular to the line joining Sirius A and B. This ensures that the slit does not go across both stars and also places Sirius B in between the diffraction spikes caused by the mirror support structure. It was known that the

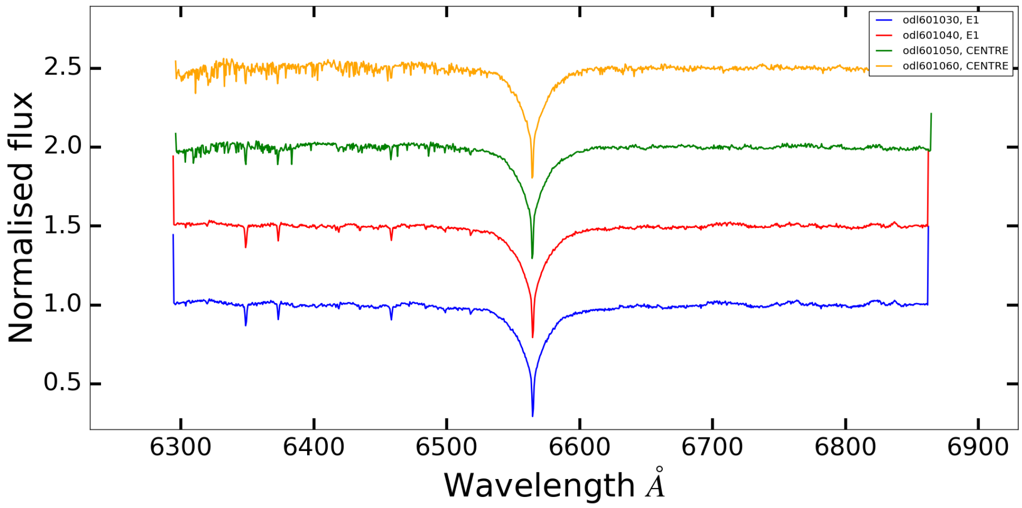

Figure 4.1: Sirius A H-α line. The 4 spectra have been normalised to remove the continuum and are offset by 0.5 in flux for clarity.

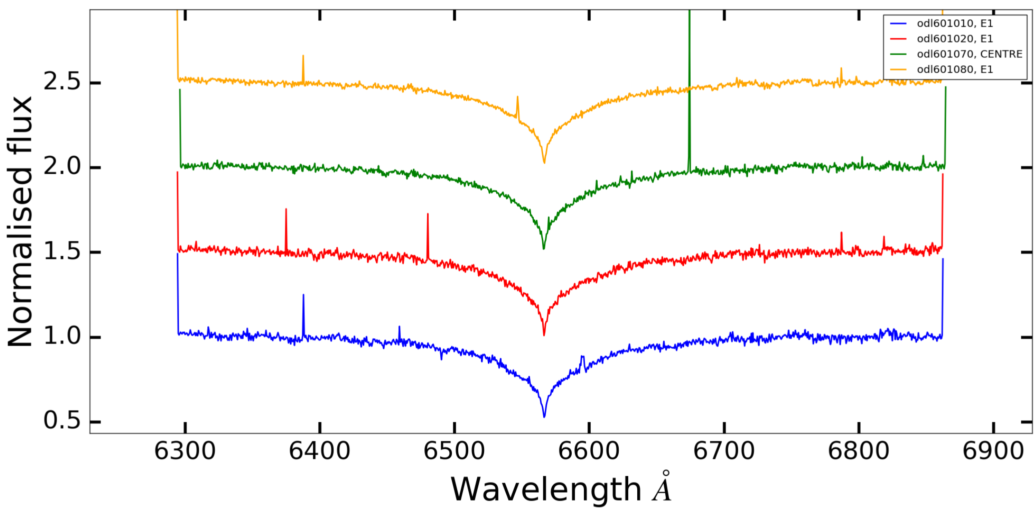

Figure 4.2: Sirius B H-α line. The 4 spectra have been normalised to remove the continuum and are offset by 0.5 in flux for clarity.

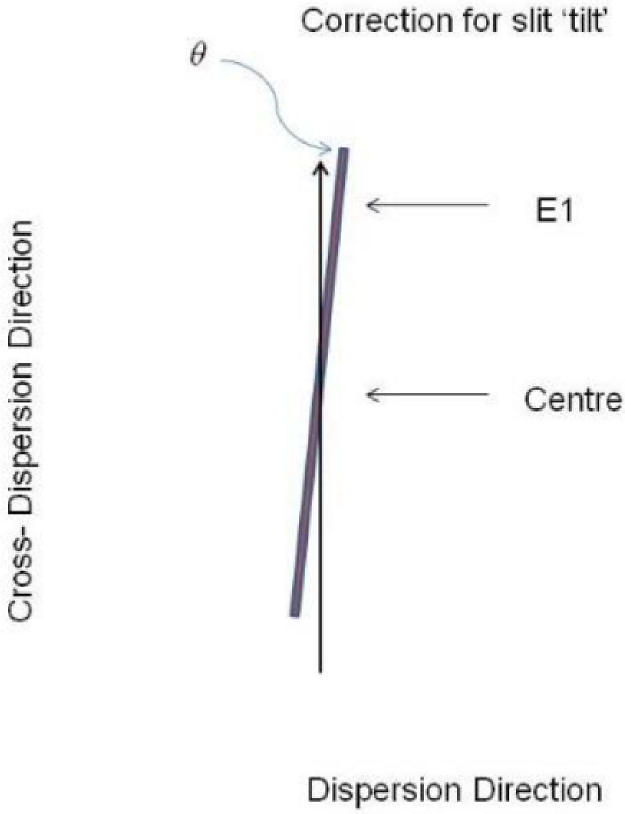

Figure 4.3: The angle of the 52x0.05" slit causes a slight offset along the dispersion (wavelength) direction when the target is at the E1 position compared to the centre position.

selected roll angle would be appropriate for avoiding the diffraction spikes of Sirius A affecting the Sirius B spectrum because a similar roll angle had been used for the 2013 observations successfully.

The position of the target along the slit changes due to the use of both the standard position, with the spectrum at the centre of the CCD (row 512), and the pseudo E1 aperture position which places the spectrum closer to the top of the CCD (row 898).

The reason for the use of the E1 position is that it places the spectrum closer to the readout node at the edge of the CCD and minimises loss of signal due to charge transfer inefficiency when the chip is read out (Friedman, 2005). The increasing charge transfer losses as the chip suffers from radiation damage mean that the E1 pseudo aperture is now the preferred position for Sirius B.

The Sirius A spectrum was likely to be highly saturated. For such a saturated spectrum, it is recommended to use the original (centre) position (Friedman, 2005). It was decided to take some exposures of each target at both slit positions (E1 and centre) so that any effects due to charge transfer inefficiency losses and saturation could be compared since it was not known how these might affect the absolute wavelength of the spectrum.

The sequence of exposures is listed in Table 4.1. When using the narrow ($52''$x0.05) slit, normal procedure is to perform a peak-up to precisely centre the target in the slit. This was done for Sirius B at the start of the observing run. The telescope was then moved to point at Sirius A. However, Sirius A is too bright to perform a peak up without changing the slit and filter settings. The distance moved between targets is only 11 arc seconds and the precision of the telescope pointing for such a small angle manoeuvre [1] is $''.0045$ It was therefore decided to forgo the peak up procedure so as to take an exposure of Sirius A without any intervening change to the slit or filter. The first sequence of spectra (odl601010 to odl601040) are therefore identical in terms of instrument set up and almost co-incident in time.

The second set of Sirius A exposures (odl601050 / 060) was taken after a peak-up to ensure the target was correctly aligned in the slit and placed at the centre position on the CCD. The following Sirius B exposure (odl601070) was also taken at the centre position for direct comparison with the preceding Sirius A spectrum (odl601060). Finally there is one more spectrum of Sirius B taken back at the E1 position. This can be compared to the two Sirius B exposures taken at the start of the orbit to check for any shift in the H-α line over the course of the observing run due to instrumental changes or possibly thermal effects such as heating and cooling of the optical bench.

The four spectra for each target are plotted in Fig. 4.1 and 4.2. The spectra have been normalised to remove the slope of the continuum and are offset by increments of 0.5 on the y axis for clarity. All spectra are free of cosmic ray hits and show no signs of any peculiarities which might affect the wavelength measurements.

4.4 Analysis

Check for contamination

The spectra of Sirius B were checked for any signs of contamination by light from Sirius A. In Fig. (4.4) are examples of the 2D images from which the Sirius B spectra are extracted. It shows no signs of scattered light from Sirius A except for

[1] A 3 arcsecond manoeuvre has an error of 0.003 arcsecond according to the STIS Instrument Handbook, Section 8.2.3

the faint spectra either side of the bright Sirius B spectrum due to the diffraction spikes crossing the slit. Panel (b) and (d) show a vertical slice through the 2-D image showing the spike in the flux at the position of the Sirius B spectrum. This shows that the spectrum is unaffected by scattered light and the faint spectrum from the diffraction spike has no impact on the main spectrum. Fig. (4.4) also illustrates the difference in position between spectra taken with the E1 (a) and centre (c) setting.

Correction for *HST* orbital motion

The correction for *HST* orbital motion was calculated and applied in the same way as described in section 3.4.3. The orbital velocity at the time of each exposure is plotted in Fig. 4.5 and values are listed in Table 4.2 (column 2). The corresponding shift in the wavelength was calculated using equation (4.1) which converts the *HST* velocity to a corresponding shift between points A and B on the detector. The correction is applied directly to the spectral files before model fitting.

Measuring the wavelength of H-α

The wavelength of the observed H-α line in the Sirius A and B spectra was measured by fitting a Lorentzian model to the core of the line. A python script utilizing the 'lmfit' library (Newville et al., 2014) was used to perform the fitting. The 'lmfit' fitting function uses the least-squares method of Levenberg-Marquardt (Press et al., 1986). This approach differs from the method used in the previous chapter because it does not rely on fitting with TLUSTY models which have an inbuilt rest wavelength for H-α and only provide the shift relative to this standard of rest. Here, the fitting makes no assumption about the rest wavelength and is simply a measure of the wavelength at the centre of the line.

For Sirius A the Lorentzian model is a good fit to the core but is not as good for fitting the core and wings simultaneously as can be seen from the models (red lines) in Fig. (4.6 panel b). The problem is minimal for the narrowest fitting range which only includes the core, but gets progressively worse as the fitting range is increased. The measured wavelength for the four fitting ranges were checked to see if there was any significant difference caused by the poor fit to the wings (see Fig. 4.8) which would affect the wider fitting ranges but not the narrow range fits. There was no significant change in the measured wavelength greater than 0.02 Å for all four fitting ranges. Also, for Sirius B the fitting was repeated with XSPEC models which are a better fit to the shape of the H-α line and there was no significant difference between the XSPEC fits and the Lorentzian fits.

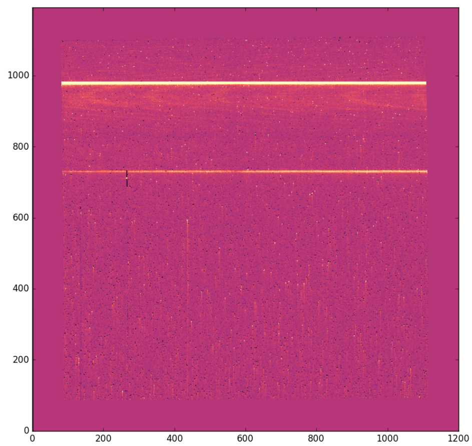

(a) Sirius B, E1 position

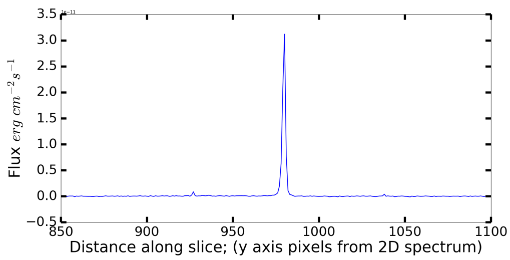

(b) Sirius B, E1 position vertical slice

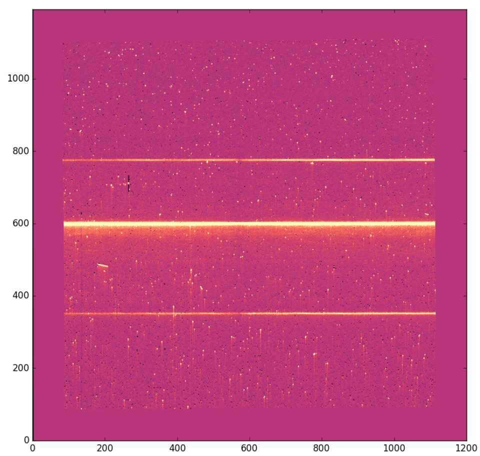

(c) Sirius B, Centre position

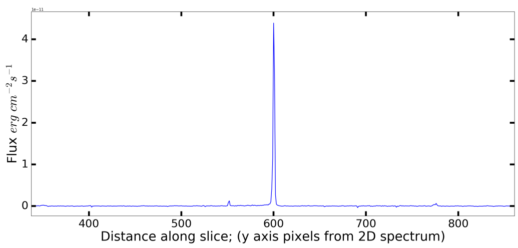

(d) Sirius B, Centre position vertical slice

Figure 4.4: Examples of the 2-D spectra of Sirius B showing the position of the spectrum on the CCD at the E1 position (a) and the centre position (c). The images are histogram equalised to show up any background clearly. Faint lines either side of the main spectrum are the signal from the diffraction spikes of Sirius A. The right hand panels show the flux for a 1 pixel wide vertical slice through the 2-D spectrum.

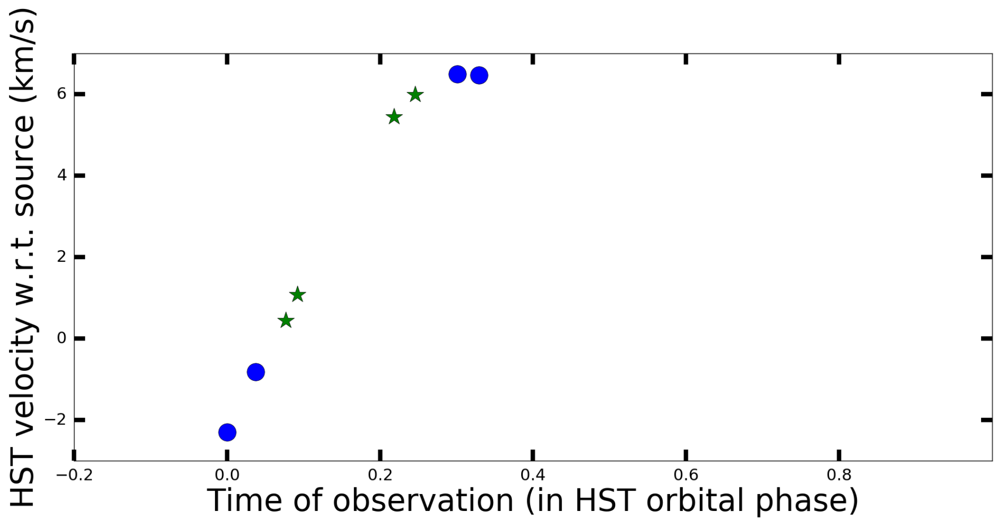

Figure 4.5: Orbital velocity of the *HST* relative to the target during each of the exposures. Symbols indicate the target : Sirius B (circles), Sirius A (stars)

Fig. 4.1 and 4.2 show that the H-α line of Sirius B is broader than Sirius A and covers a range of $\sim$ 300 Å. To accurately measure the wavelength of the line centre, the fitting for each line was repeated 4 times with a slightly increased wavelength range each time. The ranges used are 7,11,15 and 19 Å. These were chosen so as to focus on the sharply defined line core and avoid including too much of the wings which may be affected by the Stark pressure shift and asymmetry. Tests of lab based plasma have shown that the Stark shift in the H-α line increases with increasing distance from the line core (Halenka et al., 2015). For the wavelength ranges we have chosen (7-19 Å), the effect of the Stark shift is below 1 km s^{-1} (See Fig. 1.8 of the introduction chapter).

Possible evidence of Stark(pressure) shift

The fitting results were checked for any evidence of the pressure (Stark) shift which might show up as a slight increase in the measured wavelength as the fitting region is expanded to include more of the wings. The wavelength measured using each of the four ranges (7, 11, 15, 19 Å) is plotted in Figure. 4.8 where each line corresponds to one spectrum. The Sirius B measurements are marked with crosses and Sirius A measurements are circles. The measured wavelengths on the y axis are displayed as the wavelength minus the wavelength measured from the first fitting range. This puts all the measurements on the same scale and makes it easier to see how the wavelength measurement varies as the fitting region is increased (towards the right

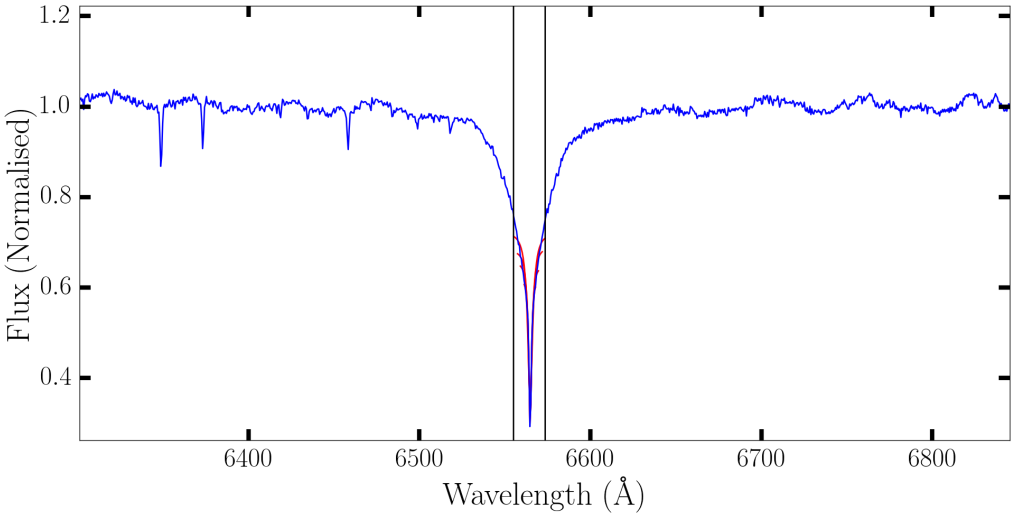

(a) Sirius A, showing the full H-α line with the core of the line used for fitting indicated by the two horizontal lines.

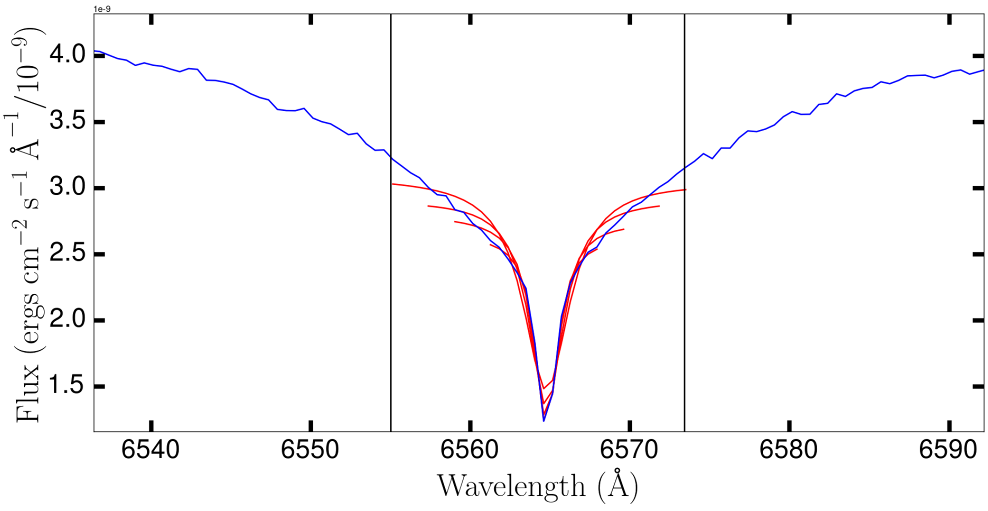

(b) Sirius A, zoom in on the central region of the figure above to show the detail of the fitting using the four wavelength ranges.

Figure 4.6: Example of fitting the Sirius A H-α line showing the extent of the wings (Top panel) and the wavelength ranges used to fit the line core (Bottom panel).

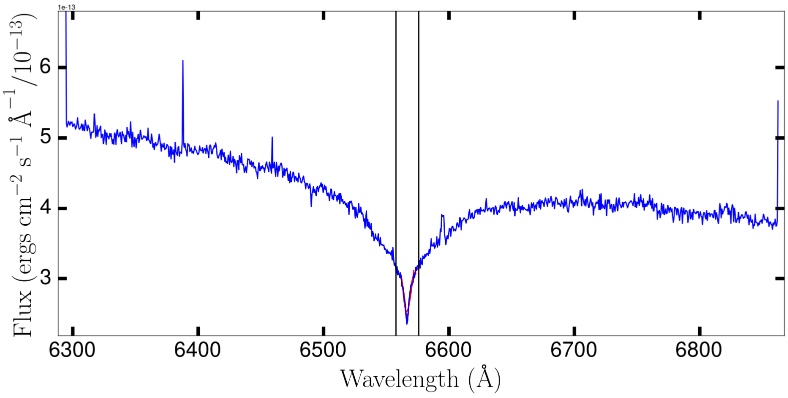

(a) Sirius B, full H-α line showing the broad wings and the sharp core region (horizontal lines) used to measure the wavelength of the line.

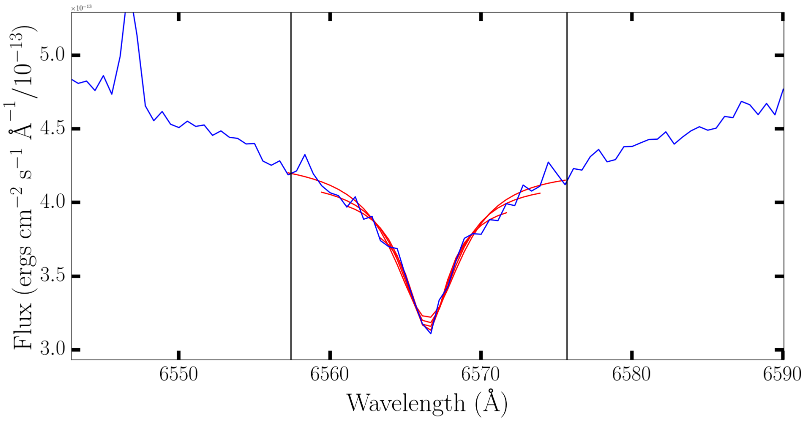

(b) Sirius B, zoom in on the core of the line showing the best fit model for each of the four wavelength ranges (red lines).

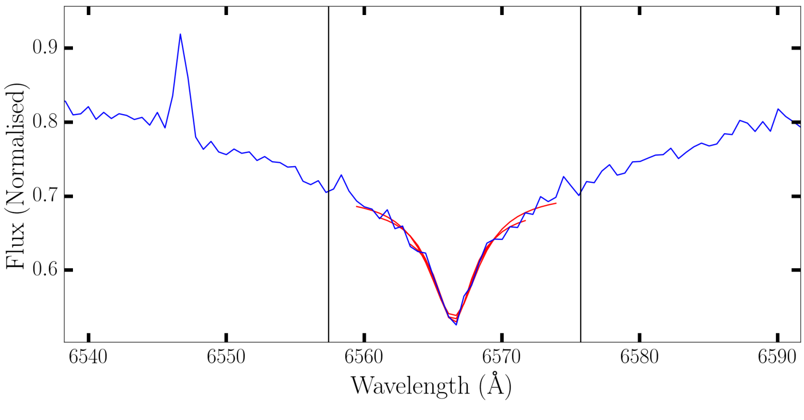

(c) Sirius B, normalised.

Figure 4.7: Example of fitting the Sirius B H-α line to measure the wavelength. **Top panel:** The full wavelength range and the extent of the broad wings. **Middle panel:** A zoom in to show detail of the fitting using the four wavelength ranges which only include the core of the line. **Bottom panel:** Same as the middle but the spectrum has been normalised to remove the slope of the continuum.

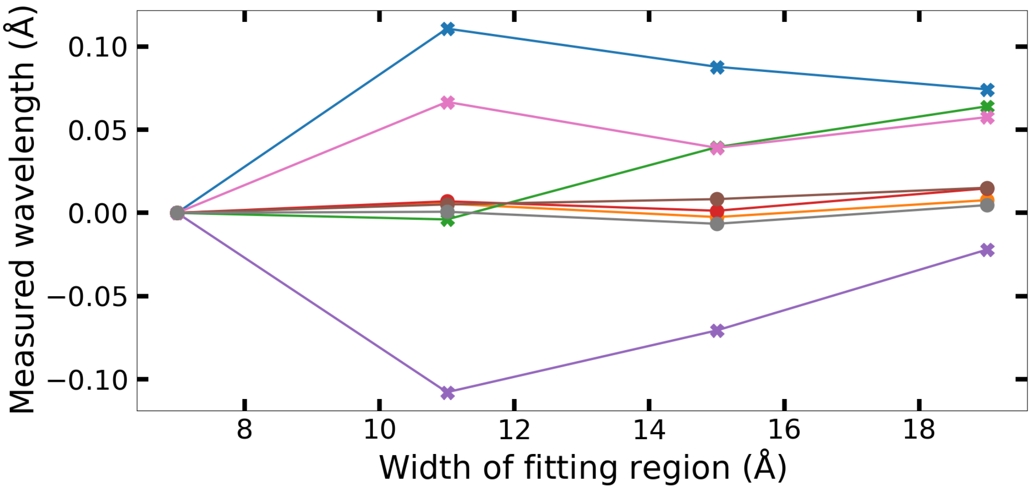

Figure 4.8: Figure showing the variation in measured wavelength of the H-α line when the fitting region is increased from 7 to 19 Å. Each line is a separate spectrum and markers indicate the target, Sirius A (circles) and Sirius B (crosses).

on the x axis).

It is notable that the 4 lines for the Sirius A spectra are tightly grouped and almost level, indicating very little variation as the fitting region is expanded. This would be expected since the lower atmospheric pressure in Sirius A would not produce a detectable pressure shift.

In contrast, the Sirius B measurements all show an increase in measured wavelength as the fitting range expands. All three of the spectra from the E1 position have a measurement from the widest fitting range which is ~ 0.06 Å larger than that from the narrow fitting range. The results from the spectrum at the 'centre' position (purple line) also appear to have increasing wavelength but the measurement for the narrowest range does not match the pattern. Overall there is some evidence for a systematic increase in measured wavelength as more of the wings are included which is the effect that would be expected from the pressure shift. The magnitude of the increase is approximately 0.06 Å. This is equivalent to $\sim$2.7 km s^{-1} which is larger than the effect observed in laboratory plasma $\sim$1 km s^{-1} at similar pressure (Halenka et al., 2015).

Calculation of the velocity

The observed velocity is calculated from the difference in the measured wavelengths between Sirius A and Sirius B. Fig. 4.9 shows the measured wavelength of each H-α line in the order in which they were observed. The markers are blue for Sirius

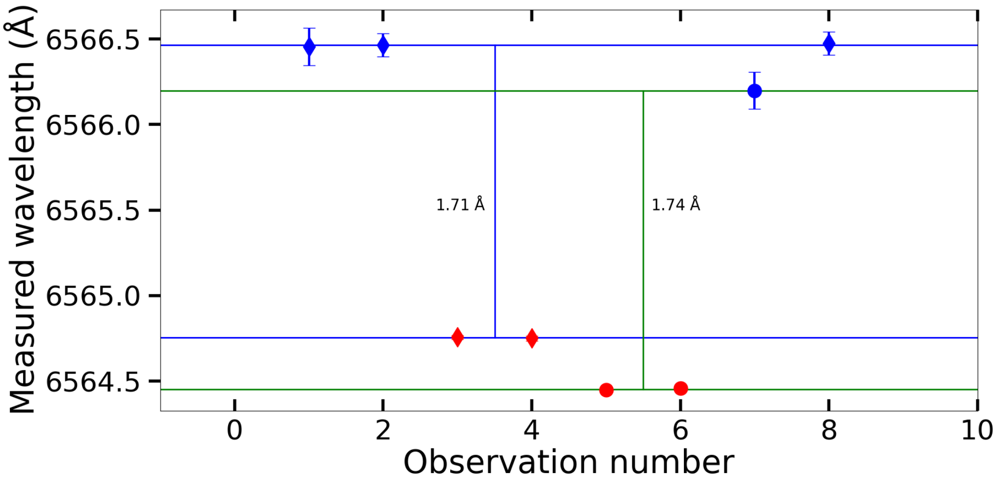

Figure 4.9: Measured wavelength for each spectrum in the order in which they were observed along the x axis. Colours indicate the target. Sirius A(red) and Sirius B(blue). Shapes indicate the aperture used, E1 position (diamonds) and 'centre' (circles). Horizontal lines show the average wavelength and vertical lines indicate the difference in average wavelength between A and B.

B and red for Sirius A. This clearly highlights the difference caused by using the E1 position (diamonds) compared to the centre position (circles). The horizontal lines indicate the average wavelength measured for the E1 spectra (blue) and centre spectra (green). The wavelengths from all individual spectra are consistent with the average when sorted by target and CCD position. The wavelength difference between A and B is calculated using the average wavelengths. E1 and centre data were calculated separately. The horizontal lines show that the difference in wavelength between A and B is 1.71 Å for E1 and 1.74 Å for centre. The wavelength difference is converted into a velocity using equation (4.1).

$$v_{obs} = \frac{\lambda_B - \lambda_A}{\lambda_A} \times c \tag{4.1}$$

Correction for velocity of Sirius A and B

Fig. 4.10 shows the radial velocities for Sirius A and B taken from the values in appendix (A)[2] which are based on the astrometrically determined orbit (Bond et al., 2017). The γ velocity of the binary centre of mass is -7.687 km s^{-1} marked by the solid black line. At the time of the 2018 observations, the velocity relative to the observer was -5.596 km s^{-1} for Sirius B and -8.794 km s^{-1} for Sirius A. These

[2]Kindly provided by Jay Holberg

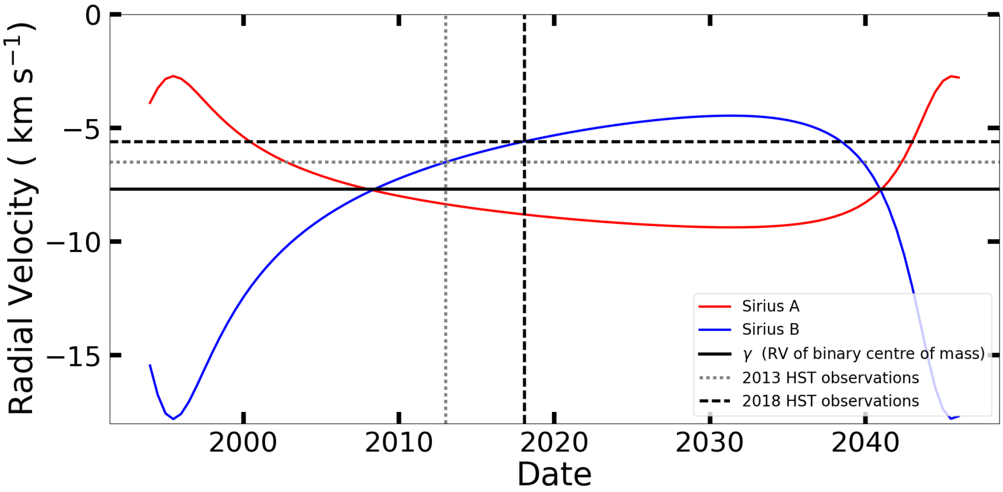

Figure 4.10: Velocity of Sirius A and B at the time of the 2018 observations. The red curve (Sirius A) and blue curve (Sirius B) show the velocity of each star relative to the observer. The faint dotted line indicates the velocity of Sirius B for the 2013 observations. The dashed line shows the Sirius B velocity during the 2018 observations. The solid horizontal line is the velocity of the binary centre of mass (γ).

values include the γ velocity.

The γ velocity affects both stars equally so it does not affect the relative wavelength shift. The only velocity that needs to be considered is the difference due to the orbital motion of the 2 stars (K_{diff} velocity). The difference in velocity between A and B is $-8.794-(-5.596) = -3.198$km s^{-1} i.e., a net differential velocity towards the observer. This has the effect of reducing the observed wavelength shift (a blue shift). The velocity of 3.198 km s^{-1} must be added back on to the observed velocity.

In addition to this, there is a small correction for the gravitational red-shift of Sirius A which was calculated in section 3.5.2 as $V_{MS,gr} = 0.759$ km s^{-1}. This produces an additional red-shift velocity which must be subtracted. The final velocity is calculated using equation (4.2).

$$v_{gr} = v_{obs} + K_{diff} - V_{MS,gr} \tag{4.2}$$

Table 4.2: List of correction factors calculated for Sirius A and B.

Obs ID	HST Orbital velocity (km s^{-1})	slit angle offset (km s^{-1})
Sirius A		
odl601030	0.4368	0.0
odl601040	1.076	0.0
odl601050	5.441	-0.634
odl601060	5.985	0.634
Sirius B		
odl601010	-2.299	-0.63
odl601020	-0.816	0.63
odl601070	6.497	0.0
odl601080	6.468	0.0

Slit angle correction

The 52″x0.05 slit is not exactly perpendicular to the dispersion direction of the CCD. It is at an angle of 0.35° to the perpendicular[3]. The position of the spectrum on the CCD therefore shifts slightly in the dispersion direction depending on the position of the target in the slit as shown in Fig. 4.3 [4]. This is important because the target is dithered along the slit between exposures so as to minimise potential problems with hot pixels. The position along the slit is recorded in the file header as POSTARG2 and can be used to calculate the shift in the wavelength. For the dithering pattern specified for these observations, only spectra 1,2,5 and 6 were offset along the slit.

As an example, for spectrum odl601020 the offset along the slit was set to ± 0.203120 arcsec. With a plate scale of 0.05 arsec/pixel this is ± 4 pixels. The offset in the dispersion direction is then $4 \times 0.35 \times \frac{\pi}{180} = 0.0248$ (pixels). In the dispersion direction the scale is 0.56 Å per pixel, amounting to a wavelength offset of $0.56 \times 0.0248 = 0.0139$ Å or 0.63 km s^{-1}. Values for the offset due to dithering are listed in Table (4.2). The wavelength offsets due to dithering are not automatically corrected in the pipeline so I have added the correction to the velocity for each spectrum.

Mass calculations

Table 4.3 gives the difference in wavelength between the Sirius A and Sirius B as plotted in Fig. 4.9. There are separate rows for observations taken at the E1 position and the centre position. The v_{obs} column gives the velocity measured from

[3]STIS instrument handbook, table 11.2
[4]Figure (4.3) courtesy of Jay Holberg

the difference in wavelength between Sirius A and B before any correction for the motion of the source. The v_{gr} column is the velocity after the correction for relative velocity between A and B and the gravitational redshift of Sirius A. Having removed all additional sources of Doppler velocity, what remains is attributed entirely to the gravitational redshift effect. The final column is the mass calculated from v_{gr} and the radius using equation (4.3). In this equation v_{gr} is in km s^{-1} and M and R are in solar units. The radius of 0.803 ± 0.011 R$_{\odot}$/100 was measured from the flux in the G430 spectra as described in Chapter 3 and uses a parallax of 378.9 ± 1.4 miliarcseconds from Bond et al. (2017).

$$M = \frac{v_{gr} R}{0.636} \tag{4.3}$$

4.5 Results

The wavelength measured for the H-α line in each spectrum is listed in Table 4.3. From the average of the E1 spectra I find an observed wavelength of 6564.753 ± 0.002 Å for Sirius A and 6566.466 ± 0.006 Å for Sirius B. The difference between the measured wavelengths is 1.713 ± 0.006 Å which gives an observed velocity of 78.31 ± 0.28 km s^{-1}.

A correction of +2.44 km s^{-1} was applied to remove the effect of the velocity of the source and the gravitational redshift of Sirius A. The final velocity of 80.65 ± 0.77 km s^{-1} gives a mass of 1.017 ± 0.025 M$_{\odot}$ via equation (4.3). For the spectra taken at the centre of the CCD, the same process gives a slightly larger mass of 1.036 ± 0.025 M$_{\odot}$.

Table 4.3: Measured wavelength, velocity and mass. The average wavelength for each target is calculated from the individual spectra. The calculation of $\Delta\lambda$ and all subsequent quantities is then calculated from the difference in the average wavelength for Sirius B compared to Sirius A. These are listed in the row marked "differential".

obsID	wavelength (Å)	$\Delta\ \lambda$ (Å)	v_{obs} (km s^{-1})	v_{gr} (km s^{-1})	Mass ($M_\odot$)
E1					
Sirius A					
odl601030	6564.756 ± 0.010	-	-	-	-
odl601040	6564.750 ± 0.015	-	-	-	-
Average	6564.753 ± 0.002				
Sirius B					
odl601010	6566.456 ± 0.111	-	-	-	-
odl601020	6566.466 ± 0.068	-	-	-	-
odl601080	6566.476 ± 0.067	-	-	-	-
Average	6566.466 ± 0.006				
Differential		1.713 ± 0.006	78.21 ± 0.28	80.65 ± 0.77	1.017 ± 0.025
Centre					
Sirius A					
odl601050	6564.447 ± 0.015	-	-	-	-
odl601060	6564.459 ± 0.011	-	-	-	-
Average	6564.453 ± 0.004				
Sirius B					
odl601070	6566.199 ± 0.108	-	-	-	-
Differential		1.746 ± 0.004	79.73 ± 0.19	82.17 ± 0.74	1.036 ± 0.025

4.6 Comparison of fitting methods

The mass of Sirius B calculated via the gravitational redshift is very sensitive to the measured wavelengths of the H-α lines. I have carried out tests using 3 slightly different methods of measuring the wavelength to ensure that the results are robust and check for any bias introduced by the fitting method.

The first method is to fit Lorentzian profiles to the core of the line as previously described. This method was applied in exactly the same way to Sirius A and B to ensure consistent results. One possible source of bias is that the H-α line is affected by the slope of the continuum and is therefore not exactly symmetrical. To check if this has any significant effect on the wavelength, the spectra were all normalised to remove the slope of the continuum. The flattened spectra were then fitted in the exact same way as the non-normalised data and the measured wavelengths compared (see Table 4.5, Method 2).

The third method of fitting is the same as that applied to the 2013 data in chapter 3, which makes use of a white dwarf spectral model calculated for the $T_{\rm eff}$ and log g of Sirius B as found from spectroscopic fitting of the Balmer lines. This method differs from the previous two in that it uses a model specifically calculated to match the line broadening in a white dwarf atmosphere and is therefore able to simultaneously fit both the core and wings of the line more accurately than a Lorentzian model. When fitting with this model, broader wavelength regions are included so as to include more of the wings. The ranges are 7, 64, 120 and 176 Å . The disadvantage of this method is that it does not provide the wavelength of the line directly. The model includes a z parameter which measures the shift required to fit the data compared to the model standard of rest. It is also sensitive to the values chosen for the $T_{\rm eff}$ and log g parameters which are fixed at the values found from fitting the G430M data. It has already been shown that the mass calculated from the spectroscopic method is lower than expected which may mean that improvements to the models are required which could result in different best fitting $T_{\rm eff}$ and log g values.

To check how sensitive the fitting results are to the $T_{\rm eff}$ and log g values used, the fitting for spectrum ODL601010 was repeated with the values increased or decreased by 5% to see how much effect this had on the best fit z value. The results in Table. 4.4 show that the z value increases with decreasing log g or $T_{\rm eff}$. However, the variation in the z value is less than 0.8 $\times 10^{-4}$ which is equivalent to a Doppler velocity of < 1 km s^{-1}. This shows that variations in the measured velocity due to the selected $T_{\rm eff}$ and log g values used when fitting the H-α line are negligible

Table 4.4: Table showing the variation in z when either $T_{\rm eff}$ or log g are varied by ± 5 per cent. The "Range" row shows the maximum difference in z caused by varying the other parameters and the equivalent Doppler velocity is given in the final column.

±%	log g	$T_{\rm eff}$	z ($\times 10^{-4}$)	Equivalent velocity (km s^{-1})
	log g fixed			
+5%	8.596	27218	5.5743	
0%	"	25922	5.5769	
−5%	"	24626	5.5804	
Range	-	-	0.006	0.2
		$T_{\rm eff}$ fixed		
+5%	9.02	25922	5.5703	
0%	8.596	"	5.5769	
−5%	8.166	"	5.5924	
Range	-	-	0.022	0.7

compared to other sources of uncertainty.

Results The standard deviation of the wavelengths from the 3 methods for each spectrum is comparable to the uncertainty in the wavelength shift given in Table 4.3. The uncertainty in each measurement is calculated from the standard error in the average of the 4 wavelength ranges used for fitting. This test shows that there are no significant biases introduced by any of the fitting methods. Also, the average wavelength measured for the 3 E1 spectra is consistent across all 3 methods within the measurement uncertainties.

Table 4.5: Comparison of the wavelength measured for the Sirius B H-α line as measured using 3 different methods.

obsID	Method 1 With cont. (Å)	Method 2 Normalised (Å)	Method 3 XSPEC (Å)	Standard deviation (σ)
odl601010 (E1)	6566.46±0.1	6566.46±0.1	6566.46±0.03	0.0018
odl601020 (E1)	6566.47±0.07	6566.48±0.04	6566.43±0.04	0.0198
odl601080 (E1)	6566.48±0.07	6566.48±0.06	6566.49±0.08	0.0050
Average	6566.466	6566.474	6566.458	
odl601070 (Centre)	6566.20±0.1	6566.21±0.1	6566.21±0.04	0.0046

4.7 Discussion

4.7.1 Sirius B and the MRR

The mass derived from the gravitational redshift measurements can be compared to the theoretical MRR for white dwarfs. The MRR plotted in Fig. 4.11 is based on the evolutionary models of (Fontaine, Brassard & Bergeron, 2001) and includes models for temperatures from 20,000 K (red) to 50,000 K (purple) in steps of 10,000 K. Dashed and solid lines represent thin and thick H-layer respectively. The difference in radius due to temperature declines towards the high mass end so the models converge.

The mass resulting from the differential redshift measurement is in excellent agreement with the theoretical MRR. Fig. 4.11 shows that Sirius B lies directly on the predicted relation. This is clear evidence that white dwarfs follow the expected trend of decreasing radius with increasing mass.

A close-up of the Sirius B data point is shown in Fig. 4.12. Here, the red line indicates a MRR calculated specifically for the temperature of 25,922 K which was found to be the best fit $T_{\rm eff}$ from spectroscopic fitting of the G430 Balmer line spectra. The mass from the E1 (green diamond) and centre (red diamond) data are plotted separately. Both are consistent with the MRR for a 25,922 K C/O core white dwarf. The E1 result is considered to be more reliable because it is based on a larger number of spectra which showed greater consistency than the centre aperture results. For comparison, the dynamical mass from Bond et al. (2017) is also plotted (blue square). The data points for the E1 redshift and dynamical mass are directly on top of one another despite being obtained using completely different methods.

4.7.2 The difference between the E1 and Centre results

It is clear that there is a systematic offset in the wavelengths measured at the E1 position compared to the center position. The offset is 0.27 Å which would be a significant additional velocity of 12 km s^{-1} if the E1 H-α line were to be compared to a laboratory rest wavelength. Two possible causes of this offset were investigated. The first possibility is that it is due to the known issue of the slit angle which is not quite perpendicular to the dispersion direction. This offset to the zero wavelength would normally be around 1-2 km s^{-1} if the target is dithered a small distance along the slit. However, the E1 position places the target at the extreme end of the slit and would have a much larger effect. From the difference between the centre and E1 position, the distance is E1 - Centre = 898 - 512 = 386 pixels in cross-dispersion direction, which gives an offset of 1.19 Å or 54.3 km s^{-1}. According to the STIS

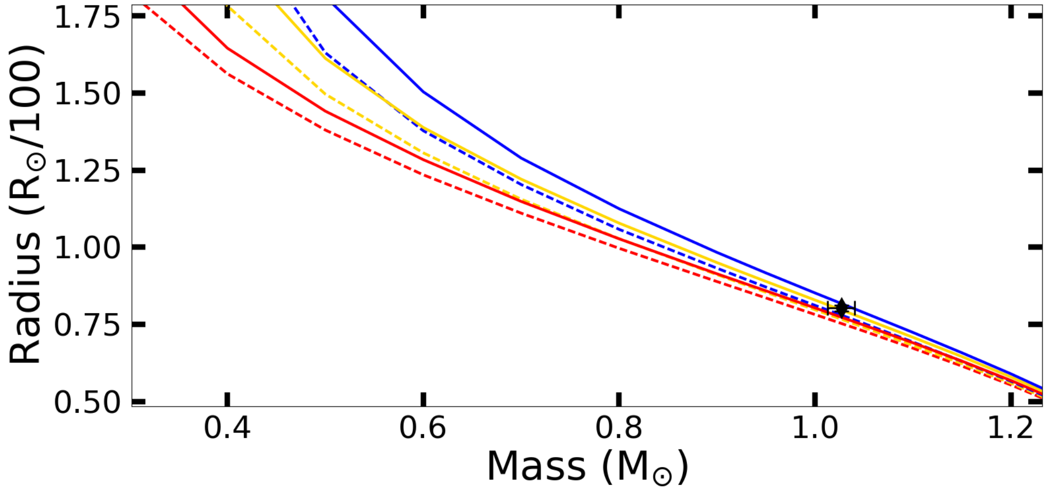

Figure 4.11: The position of Sirius B on the MRR as measured from the differential gravitational redshift. The theoretical mass-radius relations are from (Fontaine, Brassard & Bergeron, 2001) and are colour coded according to temperature from 10,000 K (red), 25,922 K (gold), 40,000 K (blue).

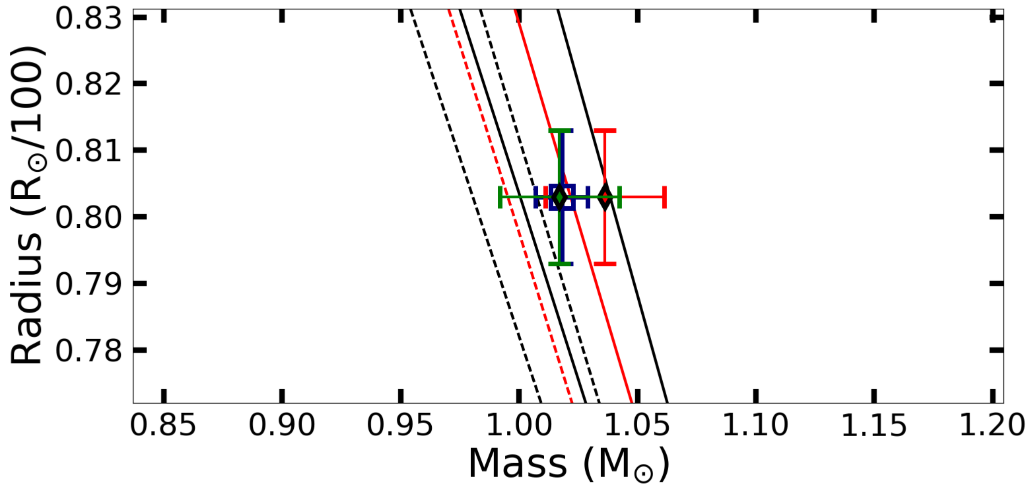

Figure 4.12: Mass measured from the gravitational red-shift at the E1 position (green diamond) compared to the mass from the dynamical method (dark blue square) (Bond et al., 2017). The red diamond is the gravitational red-shift mass from the 'centre' position. The solid and dashed lines are (Fontaine, Brassard & Bergeron, 2001) C/O core mass-radius relations for thick and thin H-layer respectively. The (red) MRR is for a temperature of 25,922 k which is the appropriate T_{eff} for Sirius B according to the spectroscopic fits to the G430 data (Chapter 3). Black lines either side are for 10,000 and 40,000 k.

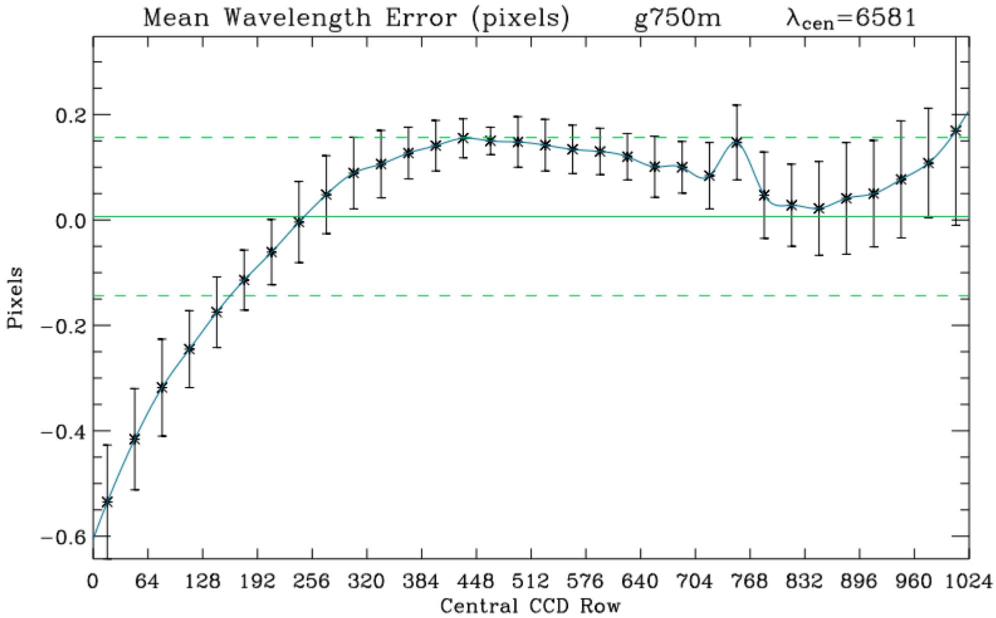

Figure 4.13: Comparison of the uncertainty in wavelength measurements at different positions on the CCD based on repeated tests using the lamp. Figure reproduced from STIS instrument science report Friedman (2005).

instrument handbook, the pipeline includes calibration for both the E1 and centre positions so this effect is automatically corrected for. It is also much larger than the offset found so this is unlikely to be the cause.

Another possibility is that the observed offset is a result of the uncertainty of the calibration at the E1 position which is known to be less accurate than the centre position. A study of the relative accuracy of the two positions was carried out by Friedman (2005)(STIS Instrument science report). The relevant figure for the G750M grating is reproduced below (4.13) and shows that at the centre (row 512) the uncertainty in the mean of the wavelength measurements is 0.05 pixels which at 0.56 Å per pixel is 0.028 Å. At the E1 position (row 896) the uncertainty increases to 0.2 pixels (0.112Å). So in terms of velocity the instrumental calibration uncertainty is 1.3 km s^{-1} and 5.1 km s^{-1} at the centre and E1 positions respectively. This could go some way to explaining the observed differences but is not enough to fully account for the offset of around 12 km s^{-1}.

4.7.3 Evidence of a systematic offset in measured wavelengths

From the results obtained with the differential analysis, it is now clear that the velocity measured with respect to the lab rest wavelength in the previous analysis is systematically too large. It is important to uncover the cause of the offset so that the gravitational redshift method can be applied to other white dwarfs where a convenient reference star may not be available.

The gravitational redshift of Sirius A is known to be less than 1 km s^{-1}. Therefore, taking the measured wavelength of Sirius A compared to the lab rest wavelength of H-α and correcting for the space motion of Sirius A should yield a zero velocity. Any residual velocity must be an instrumental effect assuming all corrections are applied correctly.

The lab rest wavelength used is 6562.795 Å which is the rest wavelength in air taken from the NIST Atomic Spectra Database. The velocities resulting from the difference between the Sirius A and rest wavelength are listed in Table (4.6, column 2). The corrections applied are +8.035 km s^{-1} for the velocity of Sirius A relative to the observer and -0.72 km s^{-1} for the gravitational redshift of Sirius A. The spectra had already been corrected for the *HST* orbital motion as described previously. The resulting velocities are listed in column 3.

The systematic offset in the E1 data could explain the discrepancy in the mass since an offset of 16 km s^{-1} is equivalent to an additional mass of 0.2 $M_\odot$ similar to the overestimate in the mass found from previous spectra. The 2013 observations used the E1 position so it is likely that they were affect by the same problem found in the new observations. If that is the case, then the systematic offset seems to be relatively stable and it may be possible to correct for it in future observations.

It can be seen that the Sirius B spectra are subject to an offset similar to the one affecting the Sirius A spectra. Fig. 4.14 shows that when the wavelength shift is calculated from the lab rest rather than using the Sirius A line as the reference wavelength, the Sirius B mass has a very similar overestimate to that seen in the 2013 data. The overestimate of $\sim$0.15$M_\odot$ is equivalent to $\sim$12 km s^{-1} which matches the offset seen in the Sirius A spectra (See Table 4.6) .

Stability of the instrument

The E1 data for Sirius B are consistent with the average throughout the whole observation showing that there was no scatter introduced due to thermal effects or changes to the instrument settings between the first and last exposure. The only

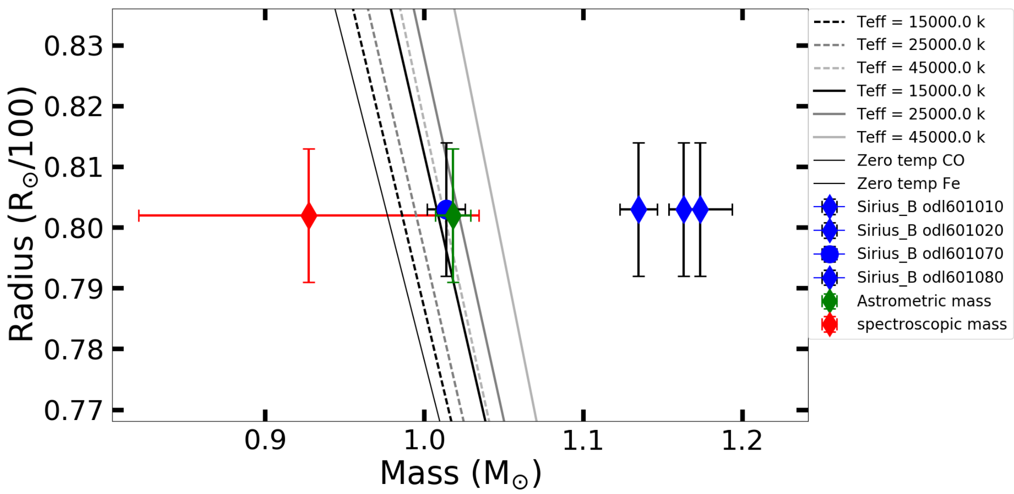

Figure 4.14: Sirius B mass when measured using the model ”lab” rest wavelength rather than the Sirius A H-α line as a reference. The three E1 spectra (blue diamonds) give a mass which is too large by the same amount as was found with the 2013 spectra. The spectrum from the centre position (blue circle) does not show an offset.

Table 4.6: The velocity (v_{obs}) of Sirius A calculated from the shift in its H-α line compared to the model rest wavelength. The final velocity is what remains after all known causes of wavelength shift have been removed, which should leave a final velocity of zero. This final column is therefore a measure of the systematic offset in the measurements.

obs ID	Wavelength (Å)	v_{obs} (km s^{-1})	Correction[a] (km s^{-1})	Final velocity (km s^{-1})
odl601030 (E1)	6564.76±0.01	6.8±0.5	9.55	16.3±0.9
odl601040 (E1)	6564.75±0.01	6.5±0.7	9.55	16.0±1.0
Average				16.2
odl601050 (Centre)	6564.45±0.02	-7.3±0.7	9.55	2.8±1.0
odl601060 (Centre)	6564.46±0.01	-6.8±0.5	9.55	2.1±0.9
Average				2.5

[a]For Sirius A binary and orbital velocity as well as gravitational redshift.

significant effect is the changing velocity due to the orbital motion of *HST*. This is predictable and easily corrected. However, it should be noted that this correction is not included automatically in the pipeline processing.

4.8 Conclusions

The mass of Sirius B as measured by the gravitaional redshift method is 1.017 ± 0.025 $M_\odot$. This matches the dynamical mass of Bond et al. (2017) almost exactly, leaving only the spectroscopic method as discrepant. The gravitational redshift mass is consistent with the MRR for a C/O core WD with thick envelope at the temperature of 25,922 K which matches the temperature derived spectroscopically from the G430M spectra.

This study has shown that the differential method of measuring the wavelength shift is a reliable and accurate method for determining the mass of white dwarfs. The offset between the wavelengths measured from spectra taken at the centre and E1 positions on the CCD, as well as the non-zero shift measurement for Sirius A after all corrections were applied confirms that it is a problem with the instrument which caused the offset in the mass measured in the previous chapter. Therefore, caution must be used when comparing measured wavelengths from *HST* to lab rest as there appears to be an unexplained offset in the *HST* spectra which is largest for the E1 position ($\sim$ 16 km s^{-1} or 0.35Å). This has been brought to the attention of the STScI instrument team who are planning to carry out further calibration tests in the near future.

Chapter 5

Summary and Conclusions

5.1 Summary

The main aims of this thesis have been firstly to test the white dwarf mass-radius relation using state of the art data. Secondly, to uncover the limitations of methods used to measure the mass and radius of a white dwarf and improve them where possible. To this end, I have focused on the spectroscopic and gravitational redshift methods. The dynamical method is already well understood and capable of producing the most accurate mass measurements, albeit for a limited number of white dwarfs.

In chapter 2 I applied the spectroscopic method of Lyman/Balmer line fitting to a sample of 11 white dwarfs combined with the best available (*Gaia* DR2) parallaxes. This study showed that the accuracy that can currently be achieved with this method is at a level where it can test the overall trends of the MRR. However, the uncertainty estimated from the spread in results from several spectra of the same target was found to be several times larger than the statistical uncertainty. Therefore, detailed tests of the effect of $T_{\rm eff}$ and H-layer are still beyond the precision of the data for most white dwarfs. The data support the validity of the MRR for the majority of the sample. The main conclusion for the spectroscopic method is that the parallax is no longer the main source of error, but the uncertainty in the spectroscopic parameters will need to be reduced if this method is to be used for further tests of the MRR.

In chapter 3 I have applied the gravitational redshift method to a sample of 4 stars and they again follow the general shape of the MRR. There were however notable discrepancies with two of the targets. Sirius B has a smaller radius than the lower mass stars as expected. However, the mass obtained from the gravitational redshift was significantly higher by ~ 0.15 $M_\odot$ when compared to the MRR and the dynamical mass. This was most likely due to an instrumental systematic effect but the cause could not be identified. HD 2133 B is a mystery as the redshift mass places it well below the C/O core MRR, consistent with a Fe core zero temperature model. This result was supported by the spectroscopic mass from both *FUSE* and *HST*, indicating that there really is something peculiar about this white dwarf rather than an error with the observations.

When comparing the methods, the scatter in results when several spectra of the same target are analysed is about the same. However, when the fitting of each H-α line is looked at in detail, it is possible to identify which results are reliable. Careful selection based on comparing each measurement against the results from the full data set can considerably reduce the error in the final result.

A number of specific issues affecting the usefulness of the gravitational redshift method have been identified. There can be a large variation in results from some spectra depending on the starting value used for the z parameter. The radial velocity of the binary and orbital velocity of the white dwarfs require independent measurements of the main sequence star and may not be available. Also, there is potentially a large instrumental offset in the case of *HST* observations as shown by the results for Sirius B.

Some progress towards solving these problems has been made with the methods developed in chapter 3. The process developed for systematically assessing each spectrum introduces more reliability when analysing a set of spectra for a target. For the radial velocity problem, a number of large surveys (e.g. RAVE, Gaia-ESO) are now providing the required measurements for thousands of stars which will prove very useful in future studies of SLSs. However, long term repeated observations will be needed to properly constrain the white dwarf orbital velocity in these systems.

The most troubling problem remaining is the unexplained offset in the mass for Sirius B. This has been dealt with in chapter 4 where the aim was to identify and resolve the cause of the Sirius B mass discrepancy.

The technique of using the H-α line of Sirius A as a reference wavelength proved successful and showed that the offset found in the previous chapter was an instrumental effect rather than a fundamental problem with the gravitational theory or method. Furthermore, this resulted in an independent mass measurement which is in agreement with both the dynamical mass and the MRR. The level of precision achieved constrains the high mass end of the MRR with a high degree of certainty. It also makes it possible to rule out the thin H-layer model for Sirius B and confirms the theoretical predictions, including finite temperature effects.

5.2 Conclusions

The main conclusions can be split in to two categories, those relating to the test of the MRR and others dealing with the methods used to make the measurements.

The overall conclusions from the observational tests of the MRR are that the majority of white dwarfs are consistent with the theory and there is no evidence of any serious deviation beyond the limits of the uncertainty in the data. The results with the highest precision are in agreement with the MRR and support the predictions of models which include finite temperature corrections. There is also some evidence that WDs can have a range of H-layer thickness.

The investigation of the spectroscopic and gravitational redshift techniques has shown that the spectroscopic method works well for most white dwarfs but can currently only provide mass measurements of limited precision. In general, the uncertainties in the log g parameter are too large to allow a definitive test of the details of the MRR, although the data are consistent with the overall trend of decreasing radius with increasing mass. The gravitational redshift results can achieve much better precision than the spectroscopic mass, but care must be taken to verify the reliability of each individual measurement from a set of spectra. As well as the apparently random errors, there is potentially a significant instrumental offset which has been shown to affect the Sirius B observations using *HST*. The most reliable way to apply the gravitational redshift method is to take reference spectra at the same time as the white dwarf is observed to enable identification and correction for instrumental issues. Observations of Sirius B carried out using this differential method are in agreement with the MRR and dynamical mass, proving that the gravitational redshift method is a valid and useful way of testing the MRR.

5.3 Future work

In the last few weeks before this thesis was finished, astronomy took a giant leap forward with the publication of *Gaia* DR2 on the 25th April 2018. The most immediate impact on this work was to reduce the uncertainty in the mass-radius measurements for thousands of white dwarfs. It will be possible to study much larger samples using the methods described in chapter 2, as there are many white dwarfs in the spectroscopic archives which were not included in DR1.

It will be important to carry out further studies on SLSs to make high precision mass measurements using the gravitational redshift and dynamical techniques. These will provide a vital test to verify and calibrate the results from the large spectroscopic samples which may well be subject to systematic errors which have still not been clearly identified or understood.

Nearly 90 years after it was first developed, observational proof of the white dwarf mass-radius relation still remains at the limit of our capabilities. Much work has gone in to shoring up the ”shaky underpinnings” of the observational MRR. In the next few years, the theory will face its most stringent tests yet, and no doubt stand battered but unbroken, as one of the pillars of astronomy.

Appendix A

Sirius binary orbital velocities and positions calculated from the model of Bond et al 2017

Date	Binary separation	Position angle	V_A	V_B
2003.00000	5.7194	123.2395	-6.564	-10.069
2003.50000	5.9511	119.7802	-6.711	-9.774
2004.00000	6.1841	116.5808	-6.848	-9.498
2004.50000	6.4172	113.6140	-6.976	-9.242
2005.00000	6.6495	110.8549	-7.096	-9.001
2005.50000	6.8800	108.2814	-7.209	-8.776
2006.00000	7.1080	105.8740	-7.314	-8.564
2006.50000	7.3328	103.6153	-7.414	-8.364
2007.00000	7.5538	101.4898	-7.508	-8.174
2007.50000	7.7707	99.4842	-7.598	-7.995
2008.00000	7.9829	97.5864	-7.682	-7.826
2008.50000	8.1902	95.7857	-7.763	-7.664
2009.00000	8.3922	94.0729	-7.840	-7.510
2009.50000	8.5887	92.4396	-7.913	-7.363
2010.00000	8.7795	90.8784	-7.983	-7.223
2010.50000	8.9643	89.3825	-8.049	-7.089
2011.00000	9.1431	87.9462	-8.113	-6.961
2011.50000	9.3156	86.5640	-8.175	-6.838
2012.00000	9.4817	85.2311	-8.234	-6.720
2012.50000	9.6412	83.9433	-8.290	-6.606
2013.00000	9.7942	82.6966	-8.345	-6.497
2013.50000	9.9404	81.4874	-8.397	-6.392
2014.00000	10.0799	80.3125	-8.448	-6.290
2014.50000	10.2124	79.1689	-8.497	-6.192
2015.00000	10.3378	78.0538	-8.544	-6.098
2015.50000	10.4563	76.9647	-8.589	-6.007
2016.00000	10.5675	75.8993	-8.633	-5.919
2016.50000	10.6715	74.8553	-8.675	-5.834
2017.00000	10.7681	73.8308	-8.716	-5.752
2017.50000	10.8574	72.8239	-8.756	-5.673
2018.00000	10.9391	71.8327	-8.794	-5.596
2018.50000	11.0133	70.8555	-8.831	-5.522
2019.00000	11.0798	69.8908	-8.867	-5.450
2019.50000	11.1386	68.9369	-8.901	-5.381
2020.00000	11.1895	67.9923	-8.935	-5.314
2020.50000	11.2325	67.0557	-8.967	-5.249
2021.00000	11.2675	66.1255	-8.998	-5.186
2021.50000	11.2943	65.2004	-9.028	-5.126
2022.00000	11.3129	64.2791	-9.057	-5.068
2022.50000	11.3231	63.3600	-9.085	-5.012
2023.00000	11.3248	62.4420	-9.112	-4.958
2023.50000	11.3179	61.5235	-9.137	-4.907
2024.00000	11.3022	60.6032	-9.162	-4.858

Date	Binary separation	Position angle	V_A	V_B
2024.50000	11.2776	59.6796	-9.185	-4.811
2025.00000	11.2440	58.7512	-9.208	-4.766
2025.50000	11.2012	57.8165	-9.229	-4.723
2026.00000	11.1490	56.8739	-9.249	-4.684
2026.50000	11.0873	55.9215	-9.267	-4.646
2027.00000	11.0158	54.9577	-9.285	-4.611
2027.50000	10.9343	53.9803	-9.301	-4.579
2028.00000	10.8427	52.9874	-9.315	-4.550
2028.50000	10.7407	51.9766	-9.328	-4.524
2029.00000	10.6280	50.9453	-9.339	-4.502
2029.50000	10.5045	49.8909	-9.349	-4.483
2030.00000	10.3697	48.8102	-9.356	-4.468
2030.50000	10.2235	47.6998	-9.362	-4.457
2031.00000	10.0655	46.5559	-9.365	-4.451
2031.50000	9.8954	45.3741	-9.365	-4.450
2032.00000	9.7128	44.1493	-9.363	-4.454
2032.50000	9.5174	42.8759	-9.358	-4.465
2033.00000	9.3088	41.5473	-9.349	-4.483
2033.50000	9.0865	40.1557	-9.336	-4.509
2034.00000	8.8502	38.6920	-9.318	-4.544
2034.50000	8.5993	37.1453	-9.295	-4.590
2035.00000	8.3335	35.5028	-9.267	-4.647
2035.50000	8.0522	33.7488	-9.231	-4.719
2036.00000	7.7550	31.8640	-9.187	-4.806
2036.50000	7.4416	29.8245	-9.134	-4.913
2037.00000	7.1114	27.6005	-9.070	-5.042
2037.50000	6.7643	25.1539	-8.992	-5.198
2038.00000	6.4001	22.4354	-8.898	-5.387
2038.50000	6.0191	19.3804	-8.784	-5.615
2039.00000	5.6220	15.9027	-8.647	-5.891
2039.50000	5.2104	11.8850	-8.479	-6.227
2040.00000	4.7869	7.1659	-8.275	-6.637
2040.50000	4.3564	1.5206	-8.025	-7.139
2041.00000	3.9273	354.6369	-7.717	-7.757
2041.50000	3.5131	346.0938	-7.337	-8.519
2042.00000	3.1356	335.3784	-6.870	-9.455
2042.50000	2.8267	322.0294	-6.302	-10.595
2043.00000	2.6252	306.0394	-5.628	-11.947
2043.50000	2.5615	288.3658	-4.868	-13.472
2044.00000	2.6335	270.7751	-4.085	-15.041
2044.50000	2.7998	254.7419	-3.393	-16.430
2045.00000	3.0025	240.7282	-2.914	-17.391
2045.50000	3.1963	228.4753	-2.714	-17.791
2046.00000	3.3604	217.5316	-2.771	-17.677

Bibliography

Adams, W. S. 1925, The Observatory, 48, 337

Arnaud, K. A. 1996, Astronomical Data Analysis Software and Systems V, 101, 17

Barstow, M. A., Barstow, J. K., Casewell, S. L., Holberg, J. B., & Hubeny, I. 2014, MNRAS, 440, 1607

Barstow, M. A., Bond, H. E., Burleigh, M. R., & Holberg, J. B. 2001, MNRAS, 322, 891

Barstow, M. A., Bond, H. E., Holberg, J. B., et al. 2005, MNRAS, 362, 1134

Barstow, M. A., Boyce, D. D., Welsh, B. Y., et al. 2010, ApJ, 723, 1762

Barstow, M. A, Casewell, S. L., Catalan, S., Copperwheat, C. et al 2014, *arXiv*, 1407.6163B

Barstow, M. A., Good, S. A., Burleigh, M., et al., 2003, *MNRAS*, 344, 562

Barstow, M.A., Good, S.A., Holberg, J.B., et al. 2002, *MNRAS*, 330, 425

Barstow, M. A., Joyce, S., Casewell, S. L., et al. 2017, 20th European White Dwarf Workshop, 509, 383

Barstow, M. A., & Werner, K. 2006, Ap&SS, 303, 3

Bédard, A., Bergeron, P., & Fontaine, G. 2017, ApJ, 848, 11

Bergeron, P., Saffer, R. A., & Liebert, J. 1992, *ApJ*, 394, 228

Bessel, F. W. 1844, MNRAS, 6, 136

Boehm-Vitense, E. 1993, AJ, 106, 1113

Bohlin, R. C. 2014, AJ, 147, 127

Bohlin, R. C., Colina, L., & Finley, D. S. 1995, AJ, 110, 1316

Bohlin, R. C., Gordon, K. D., & Tremblay, P.-E. 2014, PASP, 126, 711

Bond, H. E., Bergeron, P., & Bédard, A. 2017, ApJ, 848, 16

Bond, H. E., Gilliland, R. L., Schaefer, G. H., et al. 2015, ApJ, 813, 106

Bond, H. E., Schaefer, G. H., Gilliland, R. L., et al. 2017, ApJ, 840, 70

Bours, M. C. P., Marsh, T. R., Parsons, S. G., et al. 2016, MNRAS, 460, 3873

Burleigh, M. R., Barstow, M. A., & Fleming, T. A. 1997, MNRAS, 287, 381

Burleigh, M. R., Barstow, M. A., & Holberg, J. B. 1998, MNRAS, 300, 511

Chandrasekhar, S. 1931, MNRAS, 91, 456, "The Highly Collapsed Configurations of a Stellar Mass"

Chandrasekhar, S. 1931, ApJ, 74, 81 ,"The maximum mass of ideal white dwarfs"

Chayer, P., Fontaine, G., & Wesemael, F. 1995, ApJS, 99, 189

Dupuy, T. J., & Liu, M. C. 2011, ApJ, 733, 122

Einstein, A., 1916, "The foundation of the gerneral theory of relativity", Annalen der Physik 354, 769-822

Einstein, A., 1911, Annalen der Physik, 35, 898-908, English translation available at http://einsteinpapers.press.princeton.edu/vol3-trans/393, "On the influence of gravitation on the propagation of light".

Falcon, R. E., Bailey, J. E., Gomez, T. A., et al. 2017, 20th European White Dwarf Workshop, 509, 149

Falcon, R. E., Rochau, G. A., Bailey, J. E., et al. 2015, ApJ, 806, 214

Falcon, R. E., Winget, D. E., Montgomery, M. H., & Williams, K. A. 2012, ApJ, 757, 116

Falcon, R. E., Winget, D. E., Montgomery, M. H., & Williams, K. A. 2010, ApJ, 712, 585

Fontaine, G., Brassard, P., & Bergeron, P. 2001, *PASP*, 113, 409

Fontaine, G., & Wesemael, F. 1987, IAU Colloq. 95: Second Conference on Faint Blue Stars, 319

Fowler, R. H. 1926, MNRAS, 87, 114

Friedman, S.D. 2005, Instrument Science Report STIS 2005-03, "Wavelength Calibration Accuracy of the First-Order CCD Modes Using the E1 Aperture"

Gaia Collaboration, Prusti, T., de Bruijne, J. H. J., et al. 2016, A&A, 595, A1

Gaia Collaboration, Brown, A. G. A., Vallenari, A., et al. 2016, A&A, 595, A2

Gaia Collaboration, Brown, A. G. A., Vallenari, A., et al. 2018, arXiv:1804.09365

Gatewood, G. D., & Gatewood, C. V. 1978, ApJ, 225, 191

Gontcharov, G. A. 2006, Astronomy Letters, 32, 759

Grabowski, B., & Halenka, J. 1975, A&A, 45, 159

Grabowski, B., Halenka, J., & Madej, J. 1987, APJ, 313, 750

Green, J. C., Wilkinson, E., & Friedman, S. D. 1994, Proc. SPIE, 2283, 12

Greenstein, J. L., Oke, J. B., & Shipman, H. L. 1971, ApJ, 169, 563

Greenstein, J. L., & Trimble, V. L. 1967, ApJ, 149, 283

Halenka, J., Olchawa, W., Madej, J., & Grabowski, B. 2015, ApJ, 808, 131

Hamada, T., Salpeter, E. E. 1961, *ApJ*, 134, 683

Harrison, J. H. D., Bonsor, A., & Madhusudhan, N. 2018, MNRAS, 479, 3814

Holberg, J. B. 2010, Journal for the History of Astronomy, 41, 41

Holberg, J. B., Barstow, M. A., Bruhweiler, F. C., Cruise, A. M., & Penny, A. J. 1998, ApJ, 497, 935

Holberg, J. B., & Bergeron, P. 2006, AJ, 132, 1221

Holberg, J.B., Oswalt, T.D., & Barstow, M.A., 2012, *AJ*, 143, 68

Holberg, J. B., Oswalt, T. D., Sion, E. M., Barstow, M. A., & Burleigh, M. R. 2013, MNRAS, 435, 2077

Holberg, J. B., Oswalt, T. D., Sion, E. M., & McCook, G. P. 2016, MNRAS, 462, 2295

Holberg, J. B., Wesemael, F., Wegner, G., & Bruhweiler, F. C. 1985, ApJ, 293, 294

Hubeny, I., & Lanz, T. 1995, ApJ, 439, 875

Hubeny, I., & Lanz, T. 2017, arXiv:1706.01859

Hummer, D. G., & Mihalas, D. 1988, ApJ, 331, 794

Iben, I., Jr., & Tutukov, A. V. 1984, ApJSS, 54, 335

Jeffries, R. D., Burleigh, M. R., & Robb, R. M. 1996, A&A, 305, L45

Joyce, S. R. G., Barstow, M. A., Casewell, S. L., Holberg, J. B., & Bond, H. E. 2017, 20th European White Dwarf Workshop, 509, 389

Kalirai, J. S. 2013, MemSAI, 84, 58

Kawka, A., & Vennes, S. 2010, Binaries - Key to Comprehension of the Universe, 435, 189

Kervella, P., Thévenin, F., Morel, P., Bordé, P., & Di Folco, E. 2003, A& A, 408, 681

Koester, D., & Chanmugam, G. 1990, Reports on Progress in Physics, 53, 837

Koester, D., Schulz, H., & Weidemann, V. 1979, A&A, 76, 262

Koester, D., & Kepler, S. O. 2015, A& A, 583, A86

Kramida, A., Ralchenko, Yu., Reader, J. and NIST ASD Team (20l8). NIST Atomic Spectra Database (version 5.5.2), [Online]. Available: https://physics.nist.gov/asd [Wed Jan 24 2018]. National Institute of Standards and Technology, Gaithersburg, MD.

Kunder, A., Kordopatis, G., Steinmetz, M., et al. 2017, AJ, 153, 75

van Leeuwen, F., 2007, *A&A*, 474, 653

Lemke, M. 1997, A&A, 122, 285

Loyd, R. O. P., France, K., Youngblood, A., et al. 2016, ApJ, 824, 102

Madej, J., & Grabowski, B. 1990, A&A, 229, 467

Marsh, M. C., Barstow, M. A., Buckley, D. A., et al. 1997, MNRAS, 286, 369

Mason, B. D., Hartkopf, W. I., & Miles, K. N. 2017, AJ, 154, 200

Mestel, L. 1952, MNRAS, 112, 583

Milne, E. A. 1930, MNRAS, 91, 4

Moos, H. W., Cash, W. C., Cowie, L. L., et al. 2000, ApJ, 538, L1

Narayan, G., Axelrod, T., Holberg, J. B., et al. 2016, ApJ, 822, 67

Newville, M., Stensitzki, T., Allen, D. B., Ingargiola, A. 2014 , LM-FIT: Non-Linear Least-Square Minimization and Curve-Fitting for Python, https://doi.org/10.5281/zenodo.11813

Olchawa, W. 2002, Journal of Quantitative Spectroscopy & Radiative Transfer, 74, 417

Oswalt T.D. 2012, *JASS*, 29, 1750

Panei, J. A., Althaus, L. G., & Benvenuto, O. G. 2000, A& A, 353, 970

Parsons, S. G., Gänsicke, B. T., Marsh, T. R., et al. 2017, MNRAS, 470, 4473

Parsons, S. G., Marsh, T. R., Copperwheat, C. M., et al. 2010, MNRAS, 402, 2591

Perryman, M. A. C., Brown, A. G. A., Lebreton, Y., et al. 1998, AAP, 331, 81

Phillips, M. M. 1993, ApJ Letters, 413, L105

Pourbaix, D., Tokovinin, A. A., Batten, A. H., et al. 2004, A&A, 424, 727

Press, W. H., Flannery, B. P., & Teukolsky, S. A. 1986, Cambridge: University Press, 1986,

Preval, S. P., Barstow, M. A., Badnell, N. R., Holberg, J. B., & Hubeny, I. 2015, 19th European Workshop on White Dwarfs, 493, 15

Prialnik, D. 2009, An Introduction to the Theory of Stellar Structure and Evolution by Dina Prialnik. Cambridge University Press, 2009. ISBN: 9780521866040,

Provencal, J. L., Shipman, H. L., Høg, E., & Thejll, P. 1998, ApJ, 494, 759

Romero, A. D., Córsico, A. H., Althaus, L. G., et al. 2012, MNRAS, 420, 1462

Salpeter, E. E. 1955, ApJ, 121, 161

Schatzman, E. 1948, Nature, 161, 61

Schmidt, H. 1996, A&A, 311, 852

Shipman, H. L., Provencal, J. L., Høg, E., & Thejll, P. 1997, ApJ, 488, L43

Siess, L. 2007, A&A, 476, 893

Sion, E. M., Holberg, J. B., Oswalt, T. D., et al. 2014, AJ, 147, 129

Tremblay, P.-E., & Bergeron, P. 2008, ApJ, 672, 1144-1152

Tremblay, P.-E., & Bergeron, P. 2009, ApJ, 696, 1755

Tremblay, P.-E., Ludwig, H.-G., Steffen, M., & Freytag, B. 2013, A&A, 552, A13

Tremblay, P.-E., Gentile-Fusillo, N., Raddi, R., et al 2017, *MNRAS*, 465, 2849T

Trimble, V., & Greenstein, J. L. 1972, ApJ, 177, 441

Vauclair, G., Schmidt, H., Koester, D., & Allard, N. 1997, A&A, 325, 1055

Vauclair, G., Vauclair, S., & Greenstein, J. L. 1979, A&A, 80, 79

Vidal, C. R., Cooper, J., & Smith, E. W. 1970, JQSRT, 10, 1011

Weidemann, V. 2000, A& A, 363, 647

Whelan, J., & Iben, I., Jr. 1973, ApJ, 186, 1007

Wiese, W. L., & Kelleher, D. E. 1971, ApJ, 166, L59

Wilson, D. J., Gänsicke, B. T., Koester, D., et al. 2015, MNRAS, 451, 3237

Wood, M. A. 1995, White Dwarfs, Proceedings of the 9th European Workshop on White Dwarfs Held at Kiel, Germany (1994), 443, 41